Electronic self-organization in layered transition metal dichalcogenides

DISSERTATION

zur Erlangung des akademischen Grades
Doktor rerum naturalium
(Dr. rer. nat.)

vorgelegt

der Fakultät Mathematik und Naturwissenschaften
der Technischen Universität Dresden

von

Diplom Physiker Tobias Ritschel

geboren am 18.06.1985 in Ilmenau

Eingereicht am 13. Mai 2015
Verteidigt am 30. Oktober 2015

Gutachter:
Prof. Dr. Bernd Büchner (IFW Dresden und TU Dresden)
Prof. Dr. Kai Roßnagel (Universität Kiel)

Remarks

This thesis was typeset using the pdfTEX engine in combination with the macro package LATEX. Data plots were created with the matplotlib library for the Python programming language if not stated differently. For two-dimensional charts and drawings the Ti*k*Z package was employed. Three-dimensional visualizations were produced using the ray tracing program POV-Ray. If not stated differently, the data analysis and the postprocessing of results from numerical simulations was done within the Python programming language using the NumPy and SciPy libraries.

Kurzfassung

Das Zusammenspiel verschiedenster, auf elektronischer Selbstorganisation basierender Ordnungszustände und ihre Bedeutung für exotische elektronische Eigenschaften wie zum Beispiel Supraleitung stellt eine wesentliche Fragestellung der aktuellen Festkörperphysik dar. In der vorliegenden Arbeit wird eben dieses Zusammenspiel anhand des geschichteten Materials $1T$-TaS$_2$ sowohl experimentell als auch theoretisch detailliert untersucht.

Im ersten Teil der Arbeit wird zunächst die statische Ladungsdichtewelle in $1T$-TaS$_2$ als Funktion des Drucks und der Temperatur mit Hilfe von elastischer Röntgenbeugung untersucht. Dabei stellt sich heraus, dass die in diesem Material auftretende Supraleitung tatsächlich auf makroskopischer Ebene im Realraum mit einer inhomogenen Ladungsdichtewelle koexistiert. Diese Erkenntnis unterscheidet sich wesentlich von bisherigen Vorschlägen, die von einer Separation in supraleitende und isolierende Bereiche im Realraum ausgingen. Weiterhin verdeutlichen die Ergebnisse der Röntgenbeugungsexperimente die wichtige Rolle von Zwischenschichtkorrelationen für die Ladungsdichtewelle in $1T$-TaS$_2$.

Ausgehend von den mittels Röntgenbeugung gewonnenen detaillierten Informationen über die Ladungsdichtewellenstruktur, werden im zweiten Teil der Arbeit Modelle im Rahmen von Dichtefunktionaltheorie zur Beschreibung der elektronischen Struktur von $1T$-TaS$_2$ entwickelt. Im Unterschied zu den meisten bisherigen Studien beziehen diese Rechnungen den dreidimensionalen Charakter der Ladungsdichtewelle mit ein. Tatsächlich enthüllen diese Modellierungen der elektronischen Struktur komplexe Orbitaltexturen, welche mit der Ladungsdichtewelle verwoben sind und, abhängig von der Ausrichtung der Orbitale in benachbarten Lagen, dramatischen Einfluss auf die elektronische Struktur haben. Es wird weiterhin demonstriert, dass diese orbitalbezogenen Effekte das Schalten von technologisch relevanten Metall-Halbleiter Übergängen erlauben. Diese Ergebnisse sind daher besonders interessant für miniaturisierte ultra-schnelle Anwendungen in der Nanotechnologie. Außerdem gibt die Entdeckung von orbitalen Texturen Aufschluss bezüglich einiger ungeklärter Fragen, welche die elektronische Selbstorganisation in $1T$-TaS$_2$ betreffen: So kann die ultraschnelle Reaktion auf optische Lichtpulse, die starke Druckabhängigkeit der Ladungsdichtewelle sowie das Auftauchen einer bis dato nicht schlüssig geklärten kommensurablen Phase (bisher “Mott phase” genannt), welche in keiner anderen isostrukturellen Modifikation vorkommt, durch die Entdeckung von orbitalen Texturen besser als bisher erklärt werden.

Abstract

The interplay between different self-organized electronically ordered states and their relation to unconventional electronic properties like superconductivity constitutes one of the most exciting challenges of modern condensed matter physics. In the present thesis this issue is thoroughly investigated for the prototypical layered material $1T$-TaS_2 both experimentally and theoretically.

At first the static charge density wave order in $1T$-TaS_2 is investigated as a function of pressure and temperature by means of X-ray diffraction. These data indeed reveal that the superconductivity in this material coexists with an inhomogeneous charge density wave on a macroscopic scale in real space. This result is fundamentally different from a previously proposed separation of superconducting and insulating regions in real space. Furthermore, the X-ray diffraction data uncover the important role of interlayer correlations in $1T$-TaS_2.

Based on the detailed insights into the charge density wave structure obtained by the X-ray diffraction experiments, density functional theory models are deduced in order to describe the electronic structure of $1T$-TaS_2 in the second part of this thesis. As opposed to most previous studies, these calculations take the three-dimensional character of the charge density wave into account. Indeed the electronic structure calculations uncover complex orbital textures, which are interwoven with the charge density wave order and cause dramatic differences in the electronic structure depending on the alignment of the orbitals between neighboring layers. Furthermore, it is demonstrated that these orbital-mediated effects provide a route to drive semiconductor-to-metal transitions with technologically pertinent gaps and on ultrafast timescales. These results are particularly relevant for the ongoing development of novel, miniaturized and ultrafast devices based on layered transition metal dichalcogenides. The discovery of orbital textures also helps to explain a number of long-standing puzzles concerning the electronic self-organization in $1T$-TaS_2: the ultrafast response to optical excitations, the high sensitivity to pressure as well as a mysterious commensurate phase that is commonly thought to be a special phase a so-called “Mott phase” and that is not found in any other isostructural modification.

Contents

List of Figures

Publications

1. T. Ritschel, J. Trinckauf, K. Koepernik, B. Büchner, M. v. Zimmermann, H. Berger, Y. I. Joe, P. Abbamonte and J. Geck, "Orbital textures and charge density waves in transition metal dichalcogenides", Nature Physics **11**, 328–331 (2015).

2. P. Zhu, J. Cao, Y. Zhu, J. Geck, Y. Hidaka, S. Pjerov, T. Ritschel, H. Berger, Y. Shen, R. Tobey, J. P. Hill and X. J. Wang, "Dynamic separation of electron excitation and lattice heating during the photoinduced melting of the periodic lattice distortion in $2H$-TaSe$_2$", Applied Physics Letters **103**, 071914 (2013).

3. T. Ritschel, J. Trinckauf, G. Garbarino, M. Hanfland, M. v. Zimmermann, H. Berger, B. Büchner and J. Geck, "Pressure dependence of the charge density wave in $1T$-TaS$_2$ and its relation to superconductivity", Physical Review B **87**, 125135 (2013).

4. C. Cao, C. G. F. Blum, T. Ritschel, S. Rodan, L. Giebeler, D. Bombor, S. Wurmehl and W. Loser, "Peculiarities of anisotropic electrical resistivity in Lu$_2$PdSi$_3$ single crystals", CrystEngComm **15**, 9052–9056 (2013).

5. J. Trinckauf, T. Hänke, V. Zabolotnyy, T. Ritschel, M. O. Apostu, R. Suryanarayanan, A. Revcolevschi, K. Koepernik, T. K. Kim, M. v. Zimmermann, S. V. Borisenko, M. Knupfer, B. Büchner and J. Geck, "Electronic confinement and ordering instabilities in colossal magnetoresistive bilayer manganites", Physical Review Letters **108**, 016403 (2012).

1 Introduction

> The whole is more than the sum of its parts.
>
> *(Aristotle)*

When home computers started to spread out over the planet in the early 1980s a typical model weighed about two kilograms, was equipped with 64 kilobytes of random access memory and the central processing unit worked at a clock rate of about 1 megahertz. Nowadays, a standard smartphone weighs 150 grams, has 2 gigabytes or more of random access memory and features a multi-core processor with clock rates in the order of 2 gigahertz. The evolution from the C64 computer to modern smartphones is only one example of the tremendous technological progress that has been made during the last three decades. An indispensable ingredient for the advance of our technical capabilities is the everlasting improvement of our understanding of the physical and in particular electronic properties of complex materials, which constitutes a central objective of condensed matter research.

The condensed matter physicists, as opposed to their colleagues working in the field of high energy physics, are gifted with the fact that their research objects and the interactions between them are very well known: All surrounding matter is composed of electrons, protons and neutrons and their interaction on the relevant energy scales is dominated by electro-magnetism. However, the hitherto existing standard theories can only accurately describe rather simple systems like straightforward metals, band insulators or semiconductors. In these cases the interaction between the electrons average out which means that they can essentially be regarded as non-interacting. Nevertheless, the most intriguing cases are those where the interaction between the electrons does not effectively disappear but is rather strong. In this regime collective and self-organized phenomena can emerge: superconductivity, magnetism, colossal magnetoresistance and charge order – to name only a few. Undoubtedly, these fascinating properties involve a high potential for future applications.

The thorough examination of materials which fall into this class of correlated electron systems reveals that the corresponding electronic phase diagrams – an illustration of the different electronic states of a material as a function of external parameters like temperature and chemical doping and pressure – exhibit striking similarities. An often observed surprising feature, for instance, is that superconductivity – a state of matter where charge can move through a crystal without any resistance – exists in close proximity to what appears to be exactly the opposite: the static spatial ordering of charge. In addition, other complicated and not well understood phases with names like pseudogap phase or nematic phase frequently appear. A particularly famous example for such a behavior are the cuprate high-temperature superconductors. In these materials an antiferromagnetic Mott insulating ground state is suppressed with increasing hole-doping level and a superconducting phase emerges. Moreover, it is known that subtle structural changes can lead to a replacement of the superconducting phase with an inhomogeneous charge ordered phase – the so-called stripe phase [1, 2]. Only recently it was reported that also a charge density wave instability occurs in some cuprate superconductors and competes with superconductivity [3, 4]. The cuprate superconductors are only one example – similar issues are discussed for the newly discovered iron pnictide superconductors [5, 6], heavy fermion systems [7] and the dichalcogenides [8, 9]. Therefore, the relation between electronic order and superconductivity receives considerable attention. However, current solid state theory is not yet capable to capture the complexity of these materials from first principles. Consequently, experiments on well-defined model systems which share the same pathology are needed in order to identify crucial microscopic mechanisms and to develop effective models that describe the experimental phenomenology.

This is exactly the approach of this thesis which deals with the layered transition metal dichalcogenides as one such class of model systems. Like graphene or artificially created interfaces, these compounds belong to the family of low-dimensional electron systems – a property which gives rise to another wide variety of exciting quantum phenomena [10, 11]. Due to their layered structure these materials are rather easy to prepare in thin-film form which makes them appealing for nanotechnology applications [12–17]. An interesting representative of this material class is the compound $1T$-tantalum disulfide ($1T$-TaS_2) which recently attracted enormous attention because of its particularly complex electronic phase diagram featuring various charge density waves and pressure-induced superconductivity. In this compound, increasing pressure suppresses a well-ordered commensurate charge density wave in favor of superconductivity which resembles the characteristics found in cuprate superconductors as a function of hole doping. Moreover, in a certain pressure range the superconductivity coexists with an inhomogeneous textured charge density wave. These textured charge density waves constitute an interesting state of matter since they can be viewed as static defect lattices with astounding analogies to skyrmion lattices in magnetic systems [18]. Accordingly, $1T$-TaS_2 provides an excellent model system to study the relation between these complex ordering phenomena and superconductivity.

In this context, pressure serves as a well-defined parameter to tune the electronic structure without increasing the level of internal disorder as it is the case for chemical doping. So far the pressure-temperature electronic phase diagram of $1T$-TaS_2 has been studied in terms of electrical resistivity measurements which lack microscopic information about the charge density wave structure and the pressure-induced changes. However, such structural information are crucial in order to understand the interplay of superconductivity and charge density wave order in 1T-TaS$_2$. This lack of microscopic information will be addressed by means of X-ray diffraction as a function of temperature and pressure in chapter 4. It will be shown that the superconductivity indeed coexists with an inhomogeneous charge density wave on a macroscopic scale in real space. This result is fundamentally different from a previously proposed separation of superconducting and insulating regions in real space. Furthermore, the X-ray diffraction data uncover the important role of interlayer correlations and shed light on the role of ordered defects for the incommensurate charge density waves in 1T-TaS$_2$.

Another outstanding feature of 1T-TaS$_2$ concerns its commensurate charge density wave which is commonly associated with Mott-Hubbard-type electron correlations. Even though this mechanism for the stabilization of the commensurate charge density wave is widely accepted, important experimental facts – for instance the strong pressure dependence of this phase – remain to be understood. Also the influence of a partially disordered layer stacking which characterizes the commensurate charge density wave has not been explored so far. Exactly these questions will be addressed in chapter 5 by combining X-ray diffraction, angle-resolved photoemission spectroscopy and density functional theory model calculations. Indeed the electronic structure calculations uncover complex orbital textures, which are interwoven with the charge density wave order and cause dramatic differences in the electronic structure depending on the alignment of the orbitals between neighboring layers.

The present thesis is organized as follows: After introducing some theoretical aspects of charge density wave physics in chapter 2, the key characteristics of layered transition metal dichalcogenides and in particular 1T-TaS$_2$ are reviewed in chapter 3. Chapter 4 deals with the static charge density wave structure of 1T-TaS$_2$ as a function of pressure and temperature as revealed by state-of-the-art X-ray diffraction. More in detail, section 4.1 and 4.2 introduce the experimental method. In section 4.3 the coexistence of superconductivity and charge density wave order in 1T-TaS$_2$ is investigated. The different incommensurate charge density waves found experimentally at high pressure are discussed with respect to structural phase transitions of defect lattices in section 4.4. Numerical simulations are used to elucidate the charge density wave layer stacking in section 4.5. Chapter 5 is dedicated to the electronic structure of 1T-TaS$_2$ in the presence of charge density waves: Sections 5.1, 5.2 and 5.3 explain the theoretical and experimental approaches used to study the electronic structure. In section 5.4 the crucial role of the charge density wave layer stacking for the electronic structure of 1T-TaS$_2$ is studied. It will be shown that complex orbital textures which are intertwined with the charge density wave emerge. In section 5.5 the density functional theory results are discussed with respect to tight-binding approaches. A sophisticated density functional theory model for the commensurate charge density wave of $1T$-TaS_2 is presented in section 5.6 and a comparison to other related materials is drawn in section 5.7. Finally, a summary along with concluding remarks and an outlook are given in chapter 6.

2 Charge density waves in solids

A charge density wave (CDW) in a metal is a state where the (discrete) translational symmetry of the underlying crystal lattice is broken. The CDW ground state is characterized by a periodic spatial variation of the valence electron density with a period that is larger than the lattice parameters. Along with the variation of the valence electron density goes a modulation of the crystal lattice which is referred to as a periodic lattice modulation (PLM) [19].

In 1954 and 1955 charge density waves were first discussed by Fröhlich [20] and Peierls [21], but it took about 20 years until first experimental evidence for CDWs was found in organic materials such as TTF-TCNQ [22, 23]. With the discovery of CDW states in layered transition metal dichalcogenides (see chapter 3) shortly after, CDWs became a popular research topic [24]. The discovery of high-temperature superconductivity in cuprates in 1986 [25] shifted the mainstream research interest markedly towards cuprate superconductors and the charge density wave compounds somewhat fell into oblivion. However, recently the field of charge density waves regained enormous attention in particular due to the discovery of charge density wave order in some cuprate superconductors [3, 4, 6, 18, 26, 27].

The following chapter gives a brief introduction into some theoretical aspects of charge density waves. Deeper insights can be found, for instance, in the textbook of George Grüner [19] or in the review article of Kai Roßnagel [28].

2.1 Peierls instability

The key concepts of charge density waves can be well illustrated using a one-dimensional metallic chain (1D-metal) with a single s-electron per lattice site and a constant lattice parameter a as an example. Such a 1D-metal is illustrated in Fig. 2.1 (a). Due to the electron-phonon coupling such a system is susceptible towards a periodic lattice modulation u_n with a modulation wave vector $\mathbf{q}_m$ corresponding to twice the Fermi vector $\mathbf{k}_F$:

$$u_n = u^0 \cos(q_m \cdot x_n + \varphi), \tag{2.1}$$

where $x_n = na$ denotes the equilibrium positions of the undistorted lattice, u^0 is the amplitude of the periodic lattice modulation and φ is an arbitrary phase. Since this model is one-dimensional the bold vector notation can be dropped.

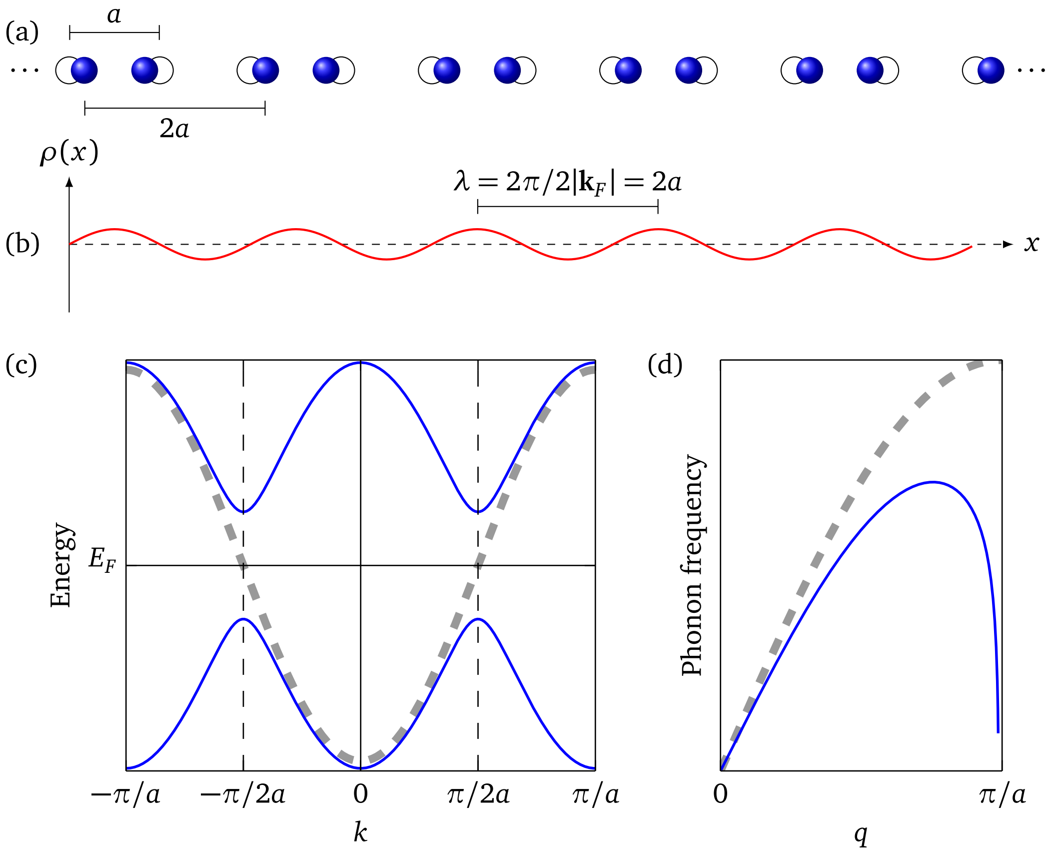

Figure 2.1: Illustration of the Peierls instability in a 1D-metal with a half-filled band. The periodic lattice modulation is schematically depicted in (a). The black open circles and the blue filled circles indicate the unreconstructed and modulated positions, respectively. The charge density wave is shown in (b). The electronic band structure of the metallic state (light gray dashed line) and in the CDW state (blue solid lines) are illustrated in (c). The renormalization of the phonon dispersion in shown in (d). Graphic in the style of reference 28.

The basic idea of the so-called Peierls instability is given by the following line of argument: The Fermi vector of the 1D-metal with a half-filled band is given by $k_F = \pi/2a$ and accordingly the Fermi surface comprises only two points: $\pm\pi/2a$, as illustrated in Fig. 2.1 (c). A periodic lattice modulation with $q_m = 2k_F = \pi/a$ leads to a doubling of the unit cell in real space which means that the lattice parameter of the modulated structure is $2a$ (cf. Fig. 2.1 (a)). As a consequence the new Brillouin zone boundaries are located at $\pm k_F = \pm\pi/2a$. Since the slope of the bands at the Brillouin zone boundary needs to be zero, gaps open at $\pm\pi/2a$, i. e. the Fermi surface points of the undistorted structure (cf. Fig. 2.1 (c)). Consequently, the energy of the occupied electron states is lowered while the energy of the empty states is raised which yields a net energy gain in the electronic system. In the simple Peierls picture it is argued that this electronic energy gain always overwhelms the elastic energy which is necessary to create the periodic lattice modulation and, accordingly, there will be a transition from the high-temperature metallic state to the insulating modulated ground state with a finite modulation amplitude u^0 at a certain critical temperature. This transition is referred to as the Peierls transition. The static modulation can be regarded as a frozen phonon mode with $q = 2k_F$, which means that the frequency of this mode becomes zero at the Peierls transition. The corresponding anomaly in the phonon dispersion is referred to as a Kohn anomaly and is depicted in Fig. 2.1 (d).

As illustrated in Fig. 2.1 (b) the periodic lattice modulation is accompanied by a modulation of the electron density ρ – the CDW:

$$\rho(x) = \rho_0(x)\left[1 + A\sin(q_m x + \varphi)\right], \tag{2.2}$$

where $\rho_0(x)$ denotes the electron density of the unreconstructed metallic state and A is the amplitude of the CDW. A CDW and a periodic lattice modulation always come together and, hence, the question what causes what is rather philosophical. The situation depicted in Fig. 2.1 applies for the case of a half filled band which means that the wavelength of the CDW λ is given by a rational multiple of the lattice constant a, yielding a so-called commensurate CDW. However, in the simplest approximation λ depends on the band filling which determines the Fermi vector k_F and, hence, can take any arbitrary value. When the ratio between λ and the lattice parameter a becomes irrational the CDW is called incommensurate.

2.2 The charge density wave ground state

We now turn the discussion towards a quantitative description of the CDW ground state. In the simplest form the coupled electron-phonon system can be described quantitatively by the so-called Fröhlich Hamiltonian:

$$H_F = \sum_{\mathbf{k}} \varepsilon_{\mathbf{k}} a^\dagger_{\mathbf{k}} a_{\mathbf{k}} + \sum_{\mathbf{q}} \hbar\omega_{\mathbf{q}} \left(b^\dagger_{\mathbf{q}} b_{\mathbf{q}} + \frac{1}{2} \right) + \sum_{\mathbf{k},\mathbf{q}} g_{\mathbf{q}} a^\dagger_{\mathbf{k}+\mathbf{q}} a_{\mathbf{k}} (b^\dagger_{-\mathbf{q}} + b_{\mathbf{q}}), \tag{2.3}$$

where $a^\dagger_{\mathbf{k}}$ ($b^\dagger_{\mathbf{k}}$) and $a_{\mathbf{k}}$ ($b_{\mathbf{k}}$) are electron (phonon) creation and annihilation operators, respectively[1]. The undistorted electron and phonon dispersions are described by $\varepsilon_{\mathbf{k}}$ and $\omega_{\mathbf{q}}$, respectively, and $g_{\mathbf{q}}$ stands for the ($\mathbf{q}$-dependent) electron-phonon coupling strength. Accordingly, the first two terms in Eq. 2.3 correspond to the non-interacting electron and phonon system and the third term describes the coupling between these two systems. Intuitively this coupling comprises processes where an electron is scattered from one state $|\mathbf{k}\rangle$ into another state $|\mathbf{k}+\mathbf{q}\rangle$ by absorbing (emitting) a phonon with momentum $\mathbf{q}$ ($-\mathbf{q}$).

---

[1] The spin degree of freedom is dropped in Eq. 2.3.

The Fröhlich Hamiltonian can be treated in a mean field type approximation (see for instance [19]) and it is possible to deduce a quantitative criterion for the stability of a CDW. Chan and Heine further extended the model by including Coulomb and exchange interaction and found the following necessary conditions for the formation of a CDW [29]:

$$\frac{4g_{\mathbf{q}}^2}{\hbar\omega_{\mathbf{q}}} - 2U_{\mathbf{q}} + V_{\mathbf{q}} \geq \frac{1}{\chi_0'(\mathbf{q})} \tag{2.4}$$

and

$$\frac{4g_{\mathbf{q}}^2}{\hbar\omega_{\mathbf{q}}} > 2U_{\mathbf{q}} > V_{\mathbf{q}} > 0, \tag{2.5}$$

where $V_{\mathbf{q}}$ and $U_{\mathbf{q}}$ denote the screened exchange interaction and the Coulomb interaction, respectively. $\chi_0'(\mathbf{q})$ is the real part of the static non-interacting electronic susceptibility $\chi_0(\mathbf{q})$. In linear response theory $\chi_0(\mathbf{q})$ describes the response of the charge density to a static external potential $\Phi(\mathbf{q})$:

$$\rho_{\text{ind}}(\mathbf{Q}) = \chi_0(\mathbf{q})\Phi(\mathbf{q}), \tag{2.6}$$

where ρ_{ind} denotes the Fourier transformed charge density induced by the external potential $\Phi(\mathbf{q})$. Eq. 2.4 confirms the intuition that a large electronic susceptibility as well as a strong electron-phonon coupling $g_{\mathbf{q}}$ favors the formation of a CDW. In the constant matrix approximation the real part $\chi_0'(\mathbf{q})$ and imaginary part $\chi_0''(\mathbf{q})$ of $\chi_0(\mathbf{q})$ are given by [30]:

$$\chi_0'(\mathbf{q}) = \sum_{\mathbf{k}} \frac{f(\varepsilon_{\mathbf{k}}) - f(\varepsilon_{\mathbf{k+q}})}{\varepsilon_{\mathbf{k}} - \varepsilon_{\mathbf{k+q}}} \tag{2.7}$$

and

$$\lim_{\omega\to 0} \chi_0''(\mathbf{q},\omega)/\omega = \sum_{\mathbf{k}} \delta(\varepsilon_{\mathbf{k}} - E_F)\delta(\varepsilon_{\mathbf{k+q}} - E_F), \tag{2.8}$$

where $f(\varepsilon)$ is the Fermi function and E_F refers to the Fermi energy. Eq. 2.7 is often referred to as the Lindhard response function and is depicted for the case of a homogeneous electron gas in one, two and three dimensions in Fig. 2.2 (a). In the 1D case $\chi_0'(q)$ displays a logarithmic divergence at $q = 2k_F$ and according to Eq. 2.4 this system is susceptible towards a distortion with $q = 2k_F$ given that $g_{\mathbf{q}=2k_F}$ is finite. This result is in line with the qualitative discussion in the previous section.

With respect to low-dimensional real materials – which are never really one-dimensional – it is often argued that Fermi surface nesting[2] leads to divergences or strong enhancements in the electronic susceptibility χ_0 and hence drives the formation of CDWs. It is true that the ima-

---

[2] Fermi surface nesting occurs when the Fermi surface contours can be translated by a certain vector (nesting vector) so that extended parts of these translated contours coincide with the original contours.

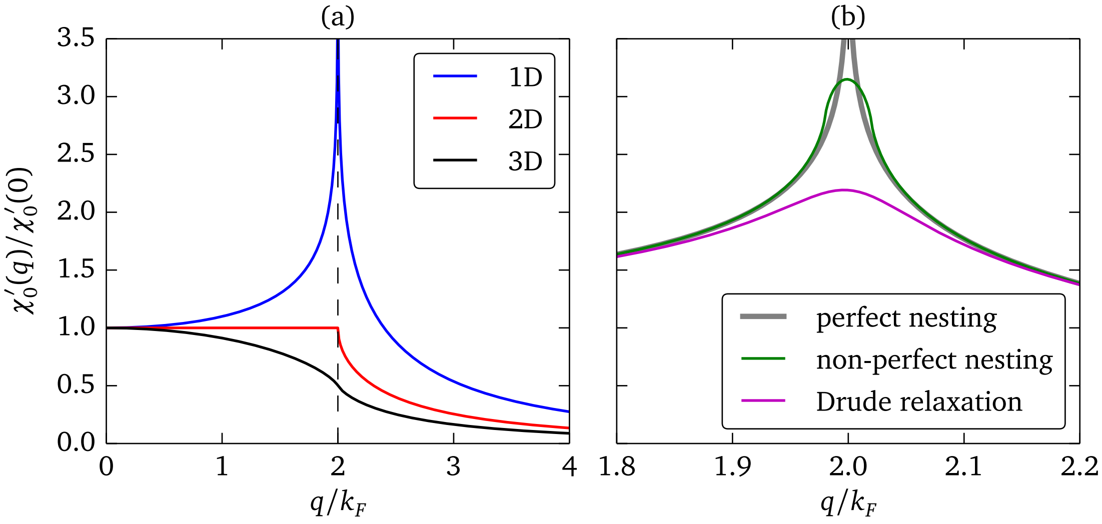

Figure 2.2: The real part of the static non-interacting electronic susceptibility χ'_0 of a homogeneous electron gas. (a): χ'_0 in one, two and three dimensions. In the 1D case χ'_0 exhibits a weak logarithmic divergence at $q = 2k_F$. This divergence vanishes in higher dimensions. (b) illustrates that the divergence in the 1D case is not robust against small deviations from "perfect nesting". The green line indicates the effect of a 2% deviation from perfect nesting. The magenta line depicts the impact of a small Drude relaxation. Figure is in the style of references 31 and 30.

ginary part of χ_0 as given in Eq. 2.8 constitutes a quantitative measure for the Fermi surface nesting, since Eq. 2.8 merely represents the autocorrelation of the Fermi surface. However, Johannes and Mazin [30] demonstrated that the divergence in the real part of the electronic susceptibility χ'_0 is not robust against small deviations from perfect nesting. As illustrated in Fig. 2.2 (b) even a slight deviation of 2% from perfect nesting, which means that the "nested" parts of the Fermi surface nest only within an accuracy of $\delta k/k_F = 0.02$ in reciprocal space, reduces the logarithmic divergence of a quasi one-dimensional system to merely an enhancement at $q = 2k_F$. A similar effect is also caused by a small finite Drude relaxation rate as shown in Fig. 2.2 (b) [30]. Since it is the real part of the susceptibility χ'_0 which gives rise to the CDW instability (cf. Eq. 2.7) the Fermi surface nesting alone certainly fails to predict CDW instabilities in real materials [30, 32]. Johannes and Mazin further pointed out that rather the **q**-dependent electron-phonon coupling $g_{\mathbf{q}}$ is crucial for the formation of charge density waves.

From Eq. 2.4 it is also clear that a strong Coulomb interaction hinders the formation of a CDW which is plausible since a CDW comes along with accumulations of charge that costs Coulomb energy.

However, once the charge density wave instability exists, the mean field solution of Eq. 2.3 shows that – within the CDW state – the phonon dispersion $\omega_{\mathbf{q}}$ becomes strongly renormalized as illustrated in Fig. 2.1 (d). The pronounced softening around $q_m = 2|\mathbf{k}_F| = \pi/a$ is commonly referred to as a Kohn-anomaly. The mean field CDW ground state is then given by a coherent superposition of electron-hole pairs and the single particle band structure develops a gap around the Fermi energy (see Fig. 2.1 (c)). How this modified band structure alters the experimentally accessible spectral function will be discussed in section 5.3.

It should be noted that the Peierls theory bears resemblance to the BCS-theory[3] of superconductivity [33]. For instance, the relation between the single particle gap Δ at $T = 0$ and the (mean field) transition temperature T^{MF} is, for both theories, given by:

$$2\Delta = 3.52 k_B T^{MF}, \tag{2.9}$$

with the Boltzmann constant k_B. This analogy is rooted in the fact that the physical mechanisms behind these phenomena are rather similar. In the case of CDWs the electron-phonon interaction leads to a pairing of electrons and holes. Similarly the electron-phonon interaction can also effectively cause the condensation of electrons into pairs – so-called Cooper pairs – in the BCS-theory. It is further interesting to mention that the electron-hole pairs which form in the CDW ground state have a total spin of $S = 0$. The pairing of electrons and holes with a total spin of $S = 1$ leads to so-called spin density waves which can be viewed as a periodic modulation of the spin density [31]. Which of the pairings (singlet superconductor, triplet superconductor, CDW or spin density wave) occurs depends – from a theoretical point of view – on microscopic details and is even for the most simple setups far from being solved [8, 34].

At this point it is worth noting that the Peierls model as introduced above is rather limited in the sense that it merely describes a single-band 1D-metal. In addition, it only applies for the weak coupling limit where the PLM amplitude is very small compared to the lattice parameter. Although this might be an admissible approximation for some (strongly 1D) simple systems, it is highly questionable how applicable the Peierls scenario is for more advanced multiband 2D (or even 3D) materials as for instance the transition metal dichalcogenides (see chapter 3).

Accordingly, it is clear that even though the Peierls mechanism represents the classical textbook approach to explain the CDW instability, the microscopic mechanism in many real materials remains widely elusive. In this context various other microscopic mechanisms for the formation of charge order are discussed in the literature as for instance the formation of local bound states leading to excitonic insulators [35] or electron localization due to electron-electron correlations in Mott-Hubbard insulators. However, the identification of the dominant mechanism in real complex materials is challenging since the experimental signatures like the excitation gap and the periodic lattice modulation[4] may be similar. Recently it has been proposed that time-resolved photoemission spectroscopy experiments may provide a route to disentangle

---

[3] BCS refers to the names of John Bardeen, Leon Cooper and Robert Schrieffer.

[4] Note that the Mott-Hubbard transition is commonly not accompanied by a periodic lattice modulation.

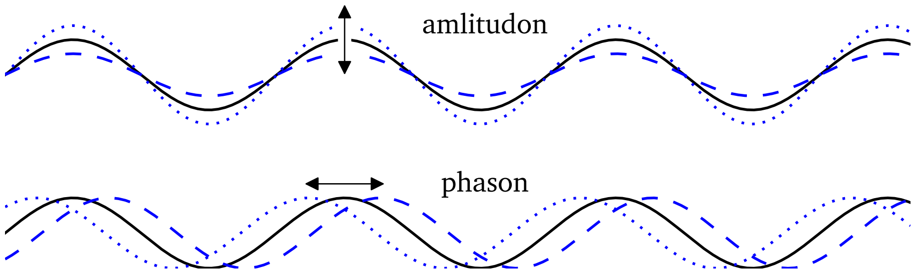

Figure 2.3: Excitation of amplitude A (amplitudon) and phase (phason) of a charge density wave in the $q \to 0$ limit. The black solid lines represent the CDW ground state. The excited CDW oscillates between the two extrema indicated by dashed and dotted blue lines.

microscopic mechanisms which take place on different time scales [36].

Another interesting development in the field of CDWs is the study of exotic charge ordered phases like chiral CDWs which are intimately related to orbital order [37]. In chapter 5.4 we will demonstrate that the CDW in several layered transition metal dichalcogenides is also intertwined with an orbital texture.

2.3 Collective excitations of charge density waves

There are two different kinds of (long wavelength) collective excitations of a CDW. The so-called amplitudon refers to a collective breathing mode of the CDW, i. e. an oscillation of the CDW amplitude A. A collective oscillation of the phase of the CDW φ is usually referred to as a phason. These two types of excitations are depicted in Fig. 2.3. It is interesting to note that for a homogeneous incommensurate CDW the ground state energy does – in first approximation – not depend on the phase φ. Accordingly, excitations related to the phase – the phasons – have a gap-less dispersion. This point holds unless the wavelength of the CDW and the periodicity of the underlying lattice crystal become commensurate (or close to commensurate). In this case the interaction between the CDW and the underlying crystal lattice cannot be neglected and the ground state energy is a periodic function of φ. Thus, the phason dispersion will be gapped in the $q \to 0$ limit. This becomes clear when we look back to Fig. 2.1 on page 6 which shows a commensurate situation. Apparently, the CDW is aligned with the lattice in such a way that the charge maxima are always in-between two nuclei, hence minimizing the Coulomb interaction between the crystal lattice and the CDW. Consequently, a shift of the CDW according to a phason with $q = 0$ (cf. Fig. 2.3) will increase the Coulomb energy which causes the gap in the phason dispersion.

The amplitude excitation, in contrast, is always associated with a gap in the limit $q \to 0$, since the energy cost to create an amplitude fluctuation is always finite and does – in first approximation – not depend on the CDW lattice interaction.

The collective excitations of a CDW can be studied on a quantitative level in the framework of Ginzburg-Landau theory (see references 38 and 19). The associated expressions and algebra are rather tedious and will not be reviewed here. However, an important result of these considerations is that the coupling between CDW and lattice leads to Sine-Gordon type nonlinear differential equations which have various soliton solutions for the phase excitations[5]. These soliton solutions represent local distortions or defects of the CDW phase that behave like particles, which means that they can propagate through the crystal without changing their shape. Moreover, the phase-solitons are associated with a charge which renders such objects highly interesting.

In the subsequent section we will discuss – on an heuristic level – the slightly different situation of a CDW that is close to being commensurable since this case is relevant for the results presented in chapter 4.

2.4 Discommensurations

We stick to the 1D CDW model introduced in Eq. 2.2 and consider an incommensurate modulation wave vector $q_m = q_c + \delta$ which is close to a commensurate vector q_c, where δ refers to the incommensurability[6]. In that case we write the CDW in the following form:

$$\phi(x) = A\cos(q_c x + \eta(x)), \tag{2.10}$$

where the function $\eta(x)$ is simply given by $\eta(x) = \delta x$. The function 2.10 is illustrated in Fig. 2.4 (b) together with the sites of the underlying 1D lattice for an exemplary $q_c = (1/3)\ a^*$ and $\delta = (1/30)\ a^*$, where $a^* = 2\pi/a$ is the shortest reciprocal lattice vector. As opposed to the commensurate case shown in Fig. 2.4 (a) it is not possible for the incommensurate CDW to globally align its charge maxima with the interspaces between the nuclei. Rather, there are extended regions where this alignment is reasonably fulfilled (highlighted in blue) and regions where the charge maxima lie on top of the nuclei (highlighted in red), which poses an unfavorable configuration in terms of Coulomb interaction. The extent of these regions apparently depends on δ and increases when δ decreases. This means that in particular for small δ, there will be large regions where the CDW is misaligned with the crystal lattice which aggregate a lot of Coulomb energy.

However, as first pointed out by McMillan [41], such an incommensurate CDW can lower

---

[5] Localized amplitude excitations – so-called amplitude-solition – also emerge [39].

[6] Note that strictly speaking δ needs to be irrational so that q_m is incommensurate. However, in practice a CDW with a wave vector $\mathbf{q}_m = \mathbf{G}/n$, where n is an integer and $\mathbf{G}$ denotes a reciprocal lattice vector, is regarded as incommensurate when n becomes sufficiently large ($n \gtrapprox 10$) [40].

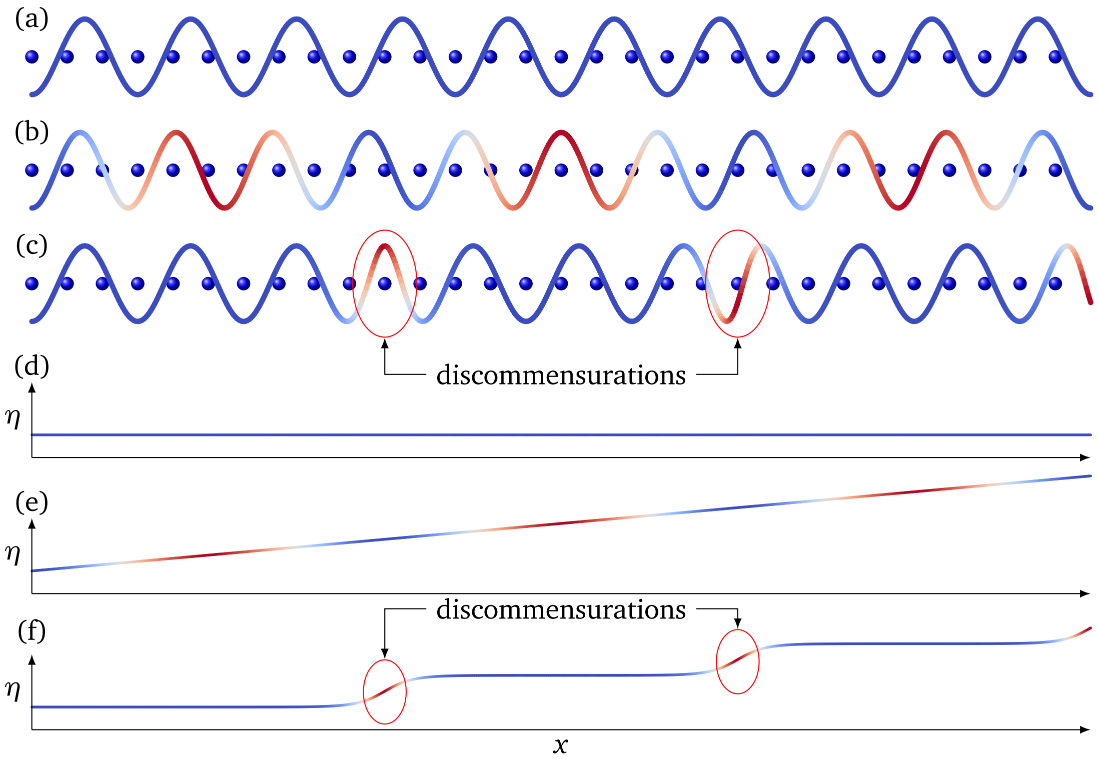

Figure 2.4: Interaction between CDW and crystal lattice and the formation of discommensurations. (a)-(c) illustrate a CDW of the form $\phi(x) = A\cos(q_c x + \eta(x))$ with $q_c = (1/3)\,a^*$, $a^* = 2\pi/a$ along with the underlying crystal lattice (blue dots) for different $\eta(x)$ which are shown in (d)-(f), respectively. (a): A commensurate CDW with $\eta(x) = 0$ as shown in (d). The charge maxima are aligned with the lattice and appear in-between two nuclei. (b): An incommensurate CDW with $\eta(x) = (1/30)\,a^* \cdot x$ as shown in (e). The color reveals regions where the charge maxima lie in-between two nuclei (blue) and regions where the maxima lie on top of a nuclei (red). (c): An incommensurate CDW with discommensurations. The corresponding function $\eta(x)$ is shown in (f). The formation of the discommensurations minimizes the regions where the charge maxima lie on top of the nuclei (red).

its energy by distorting itself in order to form commensurate regions separated by so-called discommensurations. It is clear that when the simple linear function $\eta(x) = \delta x$ for the incommensurate CDW (cf. Fig. 2.4 (e)) is distorted so that it attains a step-like form as depicted in Fig. 2.4 (f), the resulting CDW is characterized by large commensurate regions. These large regions correspond to the flat sections in $\eta(x)$ and the narrow regions where the phase rapidly changes are the discommensurations. Accordingly, the range where the CDW is misaligned with the lattice is reduced to the small regions of the discommensurations, as shown in Fig. 2.4 (c). Thus the formation of discommensurations can reduce the energy of the CDW ground state significantly. The function η may then be expanded as:

$$\eta(x) = \delta x + \sum_n a_n \sin(Mn\delta x), \tag{2.11}$$

where M is defined by the commensurate wave vector[7] $q_c = (1/M)a^*$ (with $M = 3$ in the present example) and a_n are coefficients to be determined. Heuristically, Eq. 2.11 describes the sum of a linear function and an inverse sawtooth function with a period of $\frac{2\pi}{M\delta}$ which results in the step-like function shown in Fig. 2.4 (f). Note that the fundamental wave vector of the CDW in Fig. 2.4 (c) and (f) is still given by $q_c + \delta$; the formation of the discommensurations is caused by inclusion of higher harmonics in $\eta(x)$. However, locally, i. e. within the flat regions, the wave vector is given by q_c and, hence, commensurate.

In terms of Ginzburg-Landau theory discommensurations arise from non-vanishing Lifschitz invariants in the free energy functional which give rise to terms of the form:

$$\mathcal{V} = V_0 \left[1 - \cos(M\eta(x))\right], \tag{2.12}$$

where V_0 denotes the coupling constant. These terms describe the interaction between the CDW and lattice.

In the previous section 2.3 it was pointed out that the fundamental phase excitations of the commensurate CDW state represent solitons which can be regarded as localized defects in the CDW phase with particle-like properties like charge. More precisely, a single soliton is associated with a local phase change of $2\pi/M$. In that context it is worth noting that the discommensurations can be viewed as a lattice of such solitons [31]. Accordingly, for a slightly incommensurable or nearly commensurate CDW it is energetically favourable to develop phase excitations which crystallize on a lattice. Since the discommensurations are charged they can interact with each other, which makes those defect lattices an interesting research topic. We will come back to discommensurations and the possibilities for their detection by means of X-ray diffraction in section 4.1.3. In section 4.3 and 4.4 we will discuss these effects in relation with the CDWs in 1T-TaS$_2$.

---

[7] In general q_c can be expressed as $q_c = (N/M)a^*$ with $N, M \in \mathbb{N}$. For simplicity it has been assumed that $N = 1$.

3 Layered transition metal dichalcogenides and the model system 1T-TaS$_2$

3.1 Layered transition metal dichalcogenides

Layered transition metal dichalcogenides (TMDs) are systems of the form MX_2 where M refers to a transition metal like Tantalum, Titanium or Niobium. X denotes an element from the chalcogen group: Sulfur, Selenium or Tellurium. All these compounds are characterized by a layered crystal structure consisting of X-M-X sandwich layers in which the transition metal is coordinated by six chalcogen sites. These structures exist in several polytypes. Most prominent are the 1T polytype where the coordination is trigonal octahedral and the 2H polytype with a trigonal prismatic coordination. As illustrated in Fig. 3.1 the number in 1T and 2H refers to the number of MX_2 units contained in the unit cell while T and H denote trigonal and hexagonal symmetry, respectively. The bonding between the layers is commonly associated with a weak Van der Waals type coupling. As a result of this Van der Waals gap these systems exhibit strongly anisotropic properties. For instance the electrical resistivity perpendicular to the MX_2 layers is commonly several orders of magnitude larger than in the perpendicular direction. Similar anisotropies are also observed in the thermal expansion, sound velocity and thermal conductivity [42].

Even though the layered TMDs are rather simple systems in terms of composition and structure they bear extremely diverse and interesting physics. For instance, most of the layered TMDs are known to exhibit transitions into charge density wave phases which are accompanied by anomalies in macroscopic properties like electrical resistivity and the formation of superlattices as revealed by X-ray or electron diffraction [24]. With decreasing temperature often an incommensurate CDW develops which transforms into a commensurate CDW when the temperature is further lowered. This incommensurate to commensurate transition is usually referred to as a lock-in transition. In addition, many of these systems have been found to become superconducting either in the pristine form or induced as a function of a tuning parameter like chemical substitution, intercalation or external pressure [43–45], which renders

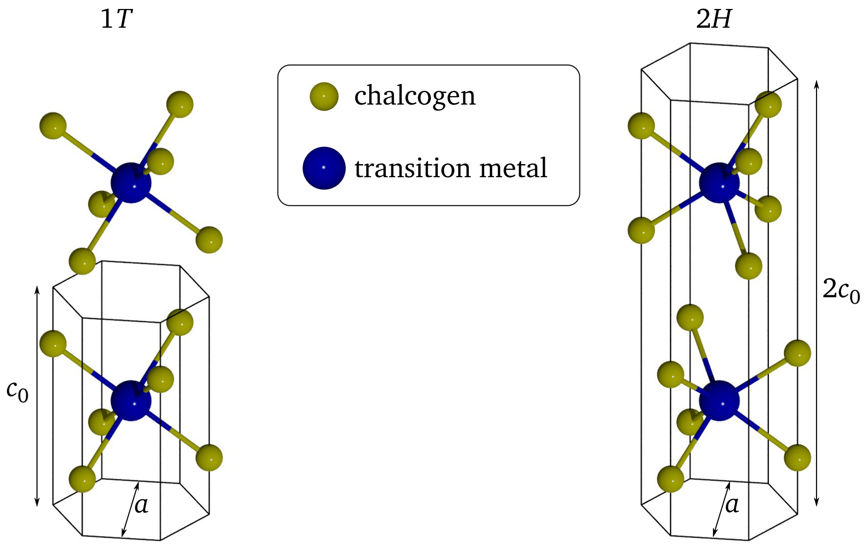

Figure 3.1: Schematic crystal structure of layered transition metal dichalcogenides. The trigonal octahedral polytype (1*T*, space group: P$\bar{3}$m1) is shown in the left panel and the trigonal prismatic polytype (2*H*, space group: P6_3/mmc) in the right panel. The Wigner-Seitz unit cell of both structures is indicated with black lines. For 1*T* the unit cell comprises one *X*-*M*-*X* sandwich. In the case of 2*H* two *X*-*M*-*X* sandwiches belong to the unit cell. c_0 refers to the distance between *X*-*M*-*X* layers.

these systems particularly appealing. Accordingly, layered TMDs are, despite several decades of intensive investigations, still a vital and alluring research topic. Not only the interplay between superconducting and charge density wave order attracts interest [45–49], but also the microscopic mechanism which drives the charge density wave instabilities is still intensively debated [28, 50] for some materials. In this context it should be mentioned that also new and exotic ideas in relation to CDWs in TMDs are emerging. For instance CDW states which break the inversion symmetry of the underlying crystal lattice – so-called chiral CDW states – are discussed [37, 51].

Due to their layered structure TMDs can be rather easily prepared in thin-film form. This characteristic along with the multitudinous electronic properties which are found in these materials makes them also suitable for nanotechnology applications. Consequently, layered TMDs recently started to attract more and more interest with respect to their high potential for the development of novel, miniaturized devices for electronic and sensing applications [12, 14–16, 52].

In this thesis we focus in particular on the system 1*T*-TaS_2 which will be discussed more detailed in the following section.

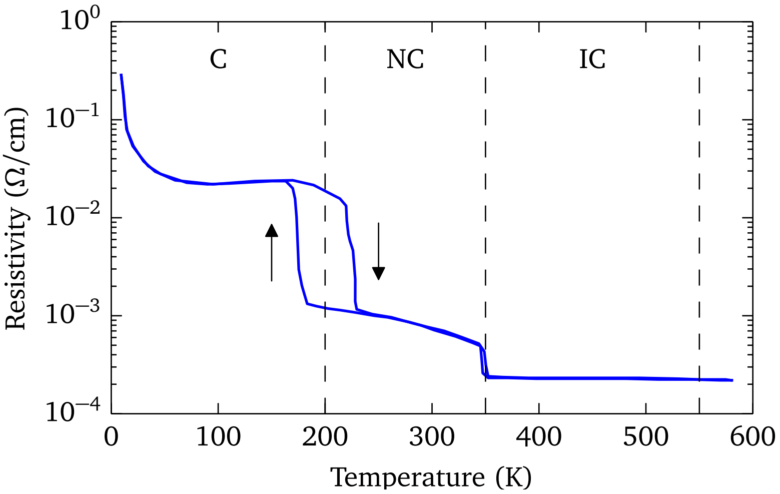

Figure 3.2: Electrical resistivity as a function of temperature at ambient pressure for 1*T*-TaS_2. The transitions between the commensurate (C-CDW), nearly commensurate (NC-CDW) and incommensurate (IC-CDW) CDW phases are accompanied by pronounced changes in resistivity. The data taken from reference 45.

3.2 The model system 1*T*-TaS_2

3.2.1 The complex electronic phase diagram

Among the TMDs, 1*T*-TaS_2 stands out because of its particularly rich electronic phase diagram as a function of temperature and pressure. This phase diagram features various different CDWs and has been first established by means of resistivity measurements [45]. As a function of decreasing temperature an incommensurate (IC) CDW is reached below ≈ 550 K. Upon further lowering the temperature the IC-CDW transforms into a nearly commensurate (NC) CDW at about 350 K which finally becomes commensurate (C) as the temperature falls below ≈ 180 K. All these transitions are associated with anomalies in the electrical resistivity as can be seen in Fig. 3.2. Furthermore, it was found that not only the individual transition temperatures depend on the external pressure but also that pressure-induced superconductivity emerges with a critical temperature of $T_c \approx 5$ K [45, 53]. The corresponding complex pressure-temperature electronic phase diagram is depicted in Fig. 3.3.

Based on this phase diagram it is clear that 1*T*-TaS_2 provides an excellent model system to study the interplay between the various electronically ordered states and superconductivity. In this context, the external pressure represents a well-defined tuning parameter which has the advantage that a single sample can be used to analyze the induced effects.

The periodic lattice modulations associated with the different CDWs in 1*T*-TaS_2 (at least for the C-CDW and NC-CDW) have been previously analyzed at ambient pressure by means of X-ray diffraction [54, 55]. These studies revealed the clustering of 13 Ta sites into a “star-of-

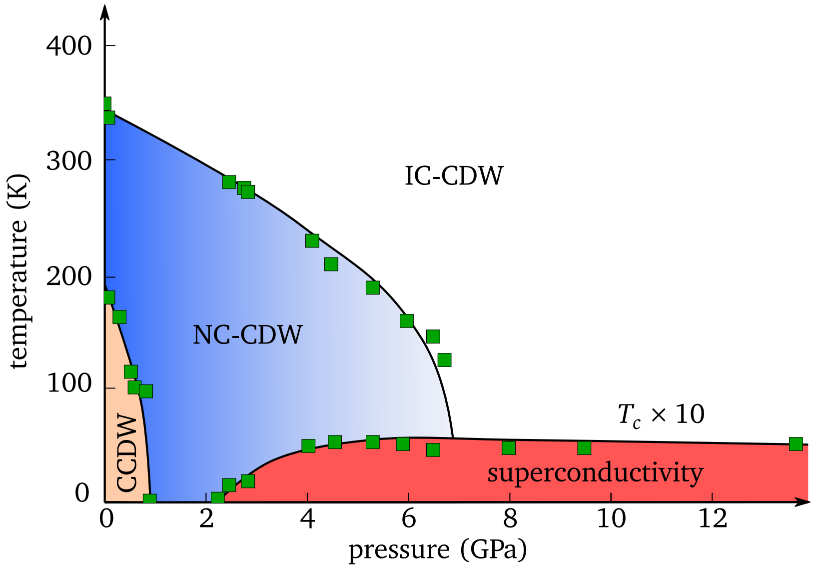

Figure 3.3: Schematic electronic pressure-temperature phase diagram of 1*T*-TaS_2 as established by means of electrical resistivity measurements [45]. The transitions between the commensurate (C-CDW), nearly commensurate (NC-CDW) and incommensurate (IC-CDW) CDW phase are pressure-dependent. Above 2 GPa a superconducting phase with $T_c \approx 5$ K occurs. In Fig. 4.8 on page 35 we will show this phase diagram again supplemented with data found in this thesis.

David" arrangement as a common structural feature which is shared by all the CDWs in 1*T*-TaS_2. As shown in Fig. 3.4 the formation of these clusters is a result of the Ta-displacements which are predominantly parallel to the ab-plane. In contrast, the S-displacements are mainly perpendicular to the ab-planes and cause a breathing mode-like buckling of the Sulfur sites (see also Fig. 5.4 on page 72).

3.2.2 The commensurate charge density wave

The C-CDW is characterized by an in-plane $\sqrt{13} \times \sqrt{13}$-superstructure built up by the "star-of-David" clusters as illustrated in Fig. 3.4. For this structure the superlattice vectors are given by $\mathbf{a}_{SL} = 4\mathbf{a} + \mathbf{b}$ and $\mathbf{b}_{SL} = -\mathbf{a} + 3\mathbf{b}$, where the length of the superlattice vectors is $|\mathbf{a}_{SL}| = \sqrt{13} \cdot |\mathbf{a}|$. Note that an equivalent superstructure with $\mathbf{a}_{SL} = 3\mathbf{a} - 1\mathbf{b}$ and $\mathbf{b}_{SL} = \mathbf{a} + 4\mathbf{b}$ also exists. Throughout this thesis we will refer to the configuration with $\mathbf{a}_{SL} = 4\mathbf{a} + \mathbf{b}$ if not stated differently.

A particularly interesting feature of the C-CDW is its partially disordered stacking along the direction perpendicular to the TaS_2 planes, which will be discussed in full length in section 4.5.

As can be seen in Fig. 3.2 the C-CDW in 1*T*-TaS_2 exhibits semiconducting transport prop-

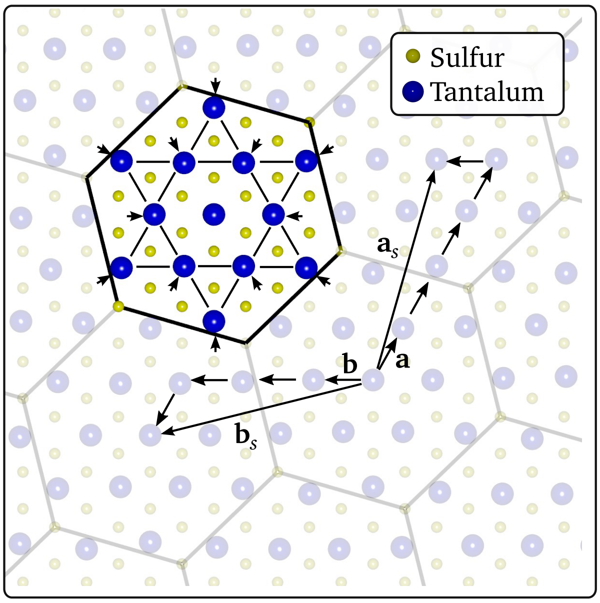

Figure 3.4: The $\sqrt{13} \times \sqrt{13}$-supercell structure of 1T-TaS$_2$ within the ab-plane. The Ta-displacements indicated by black arrows are mainly parallel to the ab-planes (**a** and **b**: in-plane lattice vectors of the undistorted P$\bar{3}$m1 crystal structure), resulting in clusters containing 13 Ta-sites, which are usually referred to as "star-of-David" arrangement. In the C-CDW these clusters form a $\sqrt{13} \times \sqrt{13}$ superlattice ($\mathbf{a}_s$ and $\mathbf{b}_s$ superlattice vectors) within the ab-plane.

erties at low temperature which represents a unique feature among the CDWs in transition metal dichalcogenides. All other CDWs which occur in these materials are metallic or even superconducting at low temperatures. Commonly, this behaviour of the C-CDW in 1T-TaS$_2$ is attributed to electron correlations as first proposed by Fazekas [56]. It was argued that – in a local picture – the $\sqrt{13} \times \sqrt{13}$-clusters may be considered as quasi-molecules in which twelve out of thirteen Ta 5d electrons occupy six localized bounding orbitals, while one electron remains in a delocalized state. According to the Mott-Hubbard-scenario, these mobile electrons can hop from cluster to cluster and localize at low temperatures due to the onsite Coulomb interaction U acting on each cluster. This Mott-Hubbard transition was further assumed to yield overlapping Hubbard subbands [56, 57]. The remaining states at the Fermi level are then prone to Anderson localization which in turn could explain the semiconducting properties of the C-CDW and the observed pseudogap [58, 59]. Experimental evidence for the presence of Mott physics in the C-CDW of 1T-TaS$_2$ has indeed been obtained recently by time-resolved pump-probe photoemission spectroscopy (cf. section 5.2) [36, 60–62]. These experiments investigate the response of the electronic structure to an optical excitation pulse as a function of the pump-probe delay. The experimental electronic band structure of the C-CDW, as measured

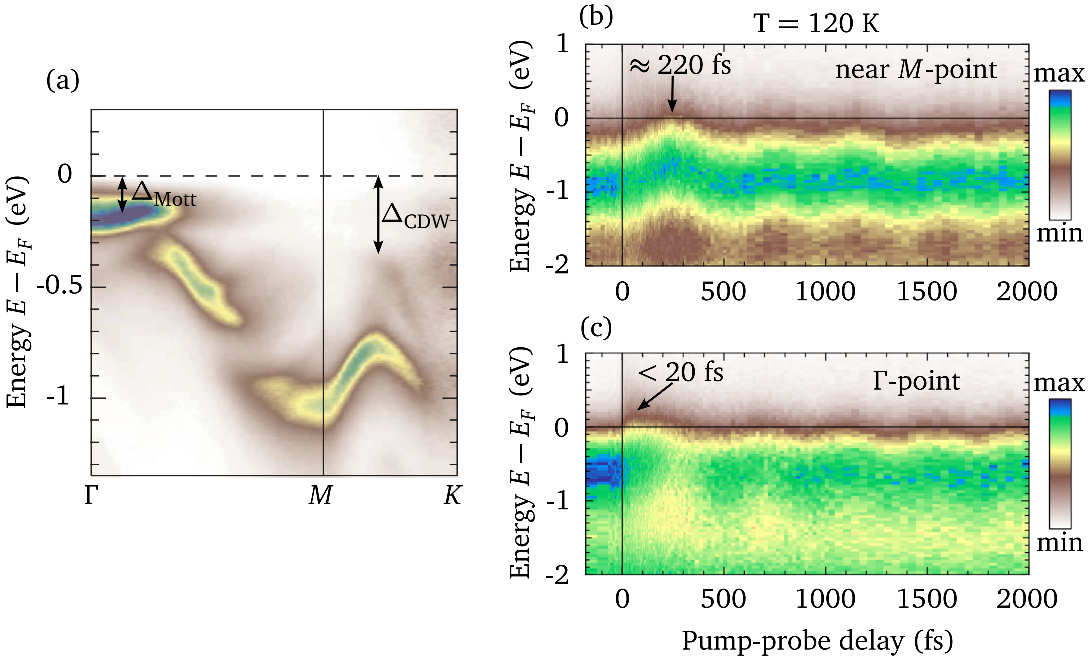

Figure 3.5: (a): Angle-resolved photoemission spectra for the C-CDW of 1*T*-TaS$_2$ along high-symmetry directions of the Brillouin zone corresponding to the unmodulated crystal structure (see section 5.4 for details). Black arrows indicate the two gaps at the Γ and near the *M* point. (b) and (c): Time-dependent angle-resolved photoemission spectra at different crystal momenta after an optical pump pulse. (b): near the *M*-point. (c): at the Γ-point. Figures taken from reference 36.

by angle-resolved photoemission spectroscopy (see section 5.2), is characterized by two gaps which are indicated in Fig. 3.5 (a). Hellmann *et al.* [36] demonstrated that these two gaps react on very different timescales to an optical excitation pulse as can be seen in Fig. 3.5 (b) and (c). The gap close to the so-called *M*-point (see section 5.4 for details) in Fig. 3.5 (b) is usually attributed to the CDW in terms of a Peierls gap as discussed in section 2.1. Accordingly, the timescale on which this gap closes is rather slow since electron-phonon coupling is crucially involved. In contrast, the gap at the Γ-point closes on an ultra-fast timescale as can be observed in Fig. 3.5 (c). This was interpreted as evidence that electron-electron interactions which give rise to ultra-fast electronic timescales play a significant role for the formation of the gap at the Γ-point [36] and, hence, for the stabilization of the C-CDW.

Although the above Mott-Hubbard scenario for the C-CDW is widely accepted, it is clear that this model is certainly oversimplified because the Tantalum 5*d* states are rather extended and, hence, itinerant which renders the local approach questionable. In chapter 5 we will investigate the electronic structure of the C-CDW theoretically as well as experimentally. One key result will be that Mott-Hubbard-type electron correlations are very likely not crucial for

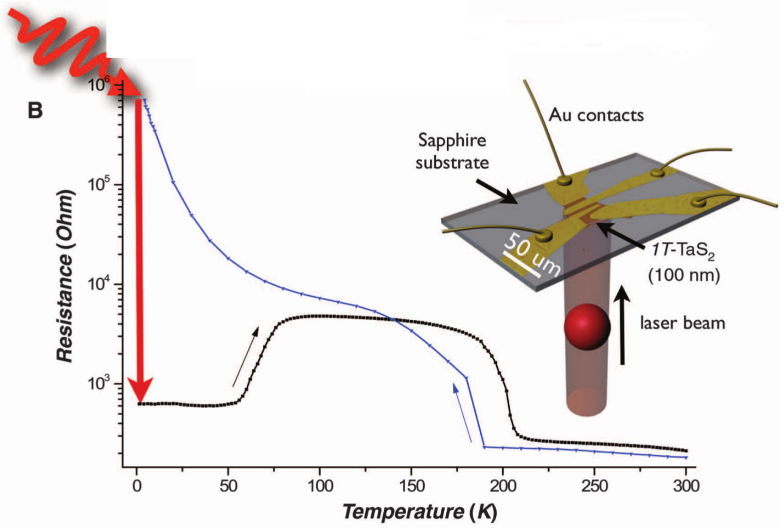

Figure 3.6: Resistivity switching in 1T-TaS$_2$ induced by a femtosecond laser pulse. At 1.5 K a 35-fs laser pulse at 800 nm causes a drop in the resistivity (red arrow) which persists unless the temperature is raised above 60 K (black curve). Figure taken from reference 63.

the properties of the C-CDW in 1T-TaS$_2$. In contrast, we will demonstrate that another purely electronic mechanism – namely the formation of orbital textures – plays a central role for the CDW in 1T-TaS$_2$.

Another highly intriguing phenomenon associated with the C-CDW is the recently observed ultra-fast resistivity switching which may be triggered by means of a femtosecond laser pulse. Stojchevska *et al.* [63] demonstrated that for a flake of 1T-TaS$_2$ at a temperature of 1.5 K a 35-fs laser pulse induces a drop of the in-plane resistivity by about three orders of magnitude as illustrated in Fig. 3.6. Most noteworthy, this new photoinduced state is persistent, which means that the system remains in this state indefinitely unless the temperature is raised or longer laser pulses are used to erase the photoinduced state. With increasing temperature the resistivity reverts to the resistivity of the C-CDW at about 100 K. It was further shown that this effect is completely reversible and the number of switching cycles is not limited [63]. Stojchevska *et al.* proposed that photoinduced domain walls (discommensurations) which also exist in the NC-CDW could account for the observed resistivity drop. However, in chapter 5.4 we will show that effects related to the discovered orbital textures in 1T-TaS$_2$ may also provide a mechanism for the observed resistivity switching.

3.2.3 The nearly commensurate charge density wave

The NC-CDW of 1T-TaS$_2$ at room temperature and ambient pressure features an in-plane modulation wave vector which is rather close to the in-plane modulation wave vector of the C-CDW.

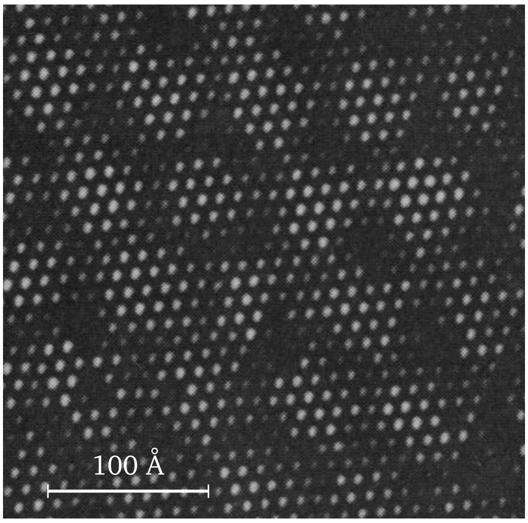

Figure 3.7: Scanning tunneling microscopic image of the surface of 1*T*-TaS$_2$ at room temperature. The bright spots are the CDW maxima and correspond to the "star-of-david" structure shown in Fig. 3.4. The additional domain structure which characterizes the NC-CDW is clearly observable. Image taken from reference 65.

As outlined in section 2.4 such a setting gives rise to the emergence of discommensurations. Indeed, the existence of the latter in the NC-CDW of 1*T*-TaS$_2$ has been verified experimentally by means of X-ray diffraction and scanning tunneling microscopy (STM) [55, 64–66]. According to these studies, the in-plane structure of the NC-CDW is given by hexagonally shaped commensurate domains separated by discommensurations [55, 65]. As can be observed in the scanning tunneling microscopy image shown in Fig. 3.7 the commensurate domains are arranged on a regular hexagonal lattice with a period of about 73 Å [65]. As opposed to the C-CDW, the stacking of the NC-CDW along the direction perpendicular to the TaS$_2$-layers is well ordered with a periodicity of three.

In order to explain the emergence of superconductivity in 1*T*-TaS$_2$ Sipos *et al.* [45] proposed – based on detailed resistivity measurements – a microscopic real space phase separation scenario. It was assumed that the superconductivity forms within the metallic discommensurations (i. e. section 2.4) which were supposed to grow with increasing pressure. Nonetheless, it is quite evident that macroscopic measurements – like electrical resistivity – cannot deliver insights into the spatial microscopic structure of the CDW. For this reason we performed X-ray diffraction on 1*T*-TaS$_2$ as a function of pressure and temperature. The corresponding results are thoroughly presented and discussed in chapter 4 and – amongst others – shed light on the relation between CDW order and superconductivity in 1*T*-TaS$_2$.

4 X-ray diffraction studies of the charge density wave order in 1*T*-TaS$_2$

In this chapter we present a study of the charge density wave order in 1*T*-TaS$_2$ as a function of temperature and pressure by means of state-of-the-art X-ray diffraction. The microscopic changes of the charge density wave order with pressure and temperature are characterized in terms of the corresponding modulation wave vectors and satellite peak intensities.

Section 4.1 and 4.2 review some basics of X-ray diffraction from modulated structures and introduce the experimental setup. In section 4.3 we show that the nearly commensurate charge density wave indeed exists in the superconducting region of the phase diagram of 1*T*-TaS$_2$. This section is an extended version of the journal article [T. Ritschel *et al.*, Phys. Rev. B **87**, 125135 (2013)]. The different incommensurate phases observed at high pressure are investigated in section 4.4. In Section 4.5 the stacking order of the charge density wave layers along the direction perpendicular to these layers is discussed.

4.1 Theory of X-ray diffraction from modulated structures

In this section, some theoretical basics of X-ray diffraction (XRD) from solids are reviewed. The focus will be on effects due to structural modulations. It is, however, not possible to elaborate this topic in an exhaustive manner. Therefore, the interested reader is relegated to the existing literature. A good chapter covering the basics of XRD can be found in the textbook of Als-Nielsen [67]. Details of the more advanced aspects like scattering from modulated structures and effects of thermal fluctuations are described in references 40, 68, 69.

4.1.1 X-ray diffraction from a periodic crystal

In kinematic[1] and classic approximation the elastic X-ray scattering from a crystal can be described by the so-called elastic scattering amplitude:

$$S(\mathbf{Q}) = P \int \mathrm{d}\mathbf{r}\rho(\mathbf{r})e^{i\mathbf{r}\cdot\mathbf{Q}}, \tag{4.1}$$

where $\mathbf{Q} = \mathbf{k} - \mathbf{k}'$ is the momentum transfer given by the scattering geometry and $\rho(\mathbf{r})$ is the electron density. P is the polarization factor and will be set to $P = 1$ for the remainder of this section. By employing the translation symmetry of the crystal lattice and, hence, of $\rho(\mathbf{r})$ the integral in Eq. 4.1 may be expressed as:

$$S(\mathbf{Q}) = \underbrace{\sum_{\mathbf{R}_n \in \mathscr{A}} e^{i\mathbf{Q}\cdot\mathbf{R}_n}}_{\text{lattice sum}} \underbrace{\sum_{\mathbf{r}_j} e^{i\mathbf{Q}\cdot\mathbf{r}_j} \overbrace{f_j(\mathbf{Q})}^{\text{atomic form factor}}}_{\text{geometric structure factor}} . \tag{4.2}$$

The first term is a sum over all lattice vectors ($\mathscr{A}$) and produces – in the limit of an infinite crystal – delta functions located at the points of the reciprocal lattice ($\mathscr{B} := \{\mathbf{b} : \mathbf{ba} = 2\pi n, \forall \mathbf{a} \in \mathscr{A}, n \in \mathbb{Z}\}$). The second term is the geometric structure factor $F_{\text{u.c}}(\mathbf{Q})$ and is a sum over all sites ($\mathbf{r}_j$) in the basis with the corresponding atomic form factors f_j. $F_{\text{u.c.}}(\mathbf{Q})$ merely modulates the intensity of the diffraction peaks but does not alter their position.

In principle it is possible to reconstruct $\rho(\mathbf{r})$ from the structure factors $F_{\text{u.c.}}(\mathbf{G}_n)$, $\mathbf{G}_n \in \mathscr{B}$ by Fourier synthesis:

$$\rho(\mathbf{r}) \sim \sum_{\mathbf{G}_n \in \mathscr{B}} e^{-i\mathbf{r}\mathbf{G}_n} F_{\text{u.c.}}(\mathbf{G}_n). \tag{4.3}$$

However, it is usually not possible to measure $F_{\text{u.c.}}$ because the scattered X-ray intensity is proportional to the square of the absolute value of $S(\mathbf{Q})$:

$$I(\mathbf{Q}) \sim S(\mathbf{Q})S^*(\mathbf{Q}) = |S(\mathbf{Q})|^2 \tag{4.4}$$

and, hence, the phase information gets lost in a X-ray diffraction experiment. This is known as the phase problem of crystallography.

---

[1] The kinematic approximation neglects multiple scattering processes and is therefore suited to describe the scattering from imperfect or small crystals. In cases where the scattering is strong, i. e. for perfect crystals the dynamical scattering theory is the more appropriate theory.

4.1.2 Modulated structures

As discussed in chapter 2 a charge density wave is in general accompanied by a periodic modulation of the underlying crystal lattice (periodic lattice modulation: PLM). From an experimentalist's point of view this is good news because the X-ray diffraction is governed by the regions where the electron density is high, as can be seen in Eq. 4.1. Since the valence electron density is rather low compared to the electron density in the vicinity of the ions in a crystal, a modulation of the former can be hardly detected by X-ray diffraction. The PLM in contrast, concerns the positions of the atoms in a crystal and can therefore be measured by means of elastic X-ray diffraction. Accordingly, X-ray diffraction does not measure the CDW directly but indirectly in terms of the accompanying PLM as explained below.

A PLM will slightly alter the positions of the atoms $\mathbf{r}_j$ in the n^{th} unit cell and may be written as:

$$\mathbf{r}_j \rightarrow \mathbf{r}_j(\mathbf{R}_n) = \mathbf{r}_j + \underbrace{\sum_k \mathbf{e}_k e^{i\mathbf{q}_k(\mathbf{r}_j+\mathbf{R}_n)} + \text{c. c.}}_{\mathbf{u}_j(\mathbf{R}_n)} \tag{4.5}$$

Eq. 4.5 describes the general case of multiple PLMs with different modulation wave vectors $\mathbf{q}_k$ and polarization vectors $\mathbf{e}_k$. Note that $\mathbf{e}_k$ is not normalized but contains the amplitude of the corresponding PLM.

It is clear that in the case where $\mathbf{q}$ can be expressed as $\mathbf{q} = h\mathbf{G}_1^* + k\mathbf{G}_2^* + l\mathbf{G}_3^*$ where $\mathbf{G}_i$ are reciprocal basis vectors and the Miller indices h, k, l are *rational* coefficients the $\mathbf{u}_j(\mathbf{R}_n)$ will be periodic in n. This means that it is possible to describe such a structure in the usual way by using a larger unit cell, the so-called supercell. A CDW or PLM with this property is called commensurate. In the other case where at least one of the coefficients h, k, l is *irrational* the $\mathbf{u}_j(\mathbf{R}_n)$ are not periodic and, hence, the discrete (3D) translation symmetry of the crystal is broken. Such a structure is called incommensurate. In fact, an experiment cannot distinguish between rational and irrational numbers and therefore – in practice – a structure is said to be incommensurate when the denominator of at least one of the Miller indices is sufficiently large.

To leading order in the displacement $\mathbf{u}_j(\mathbf{R}_n)$ the scattering amplitude for the modulated structure is given by:

$$S(\mathbf{Q}) = \sum_{\mathbf{R}_n \in \mathscr{A}} e^{i\mathbf{Q}\cdot\mathbf{R}_n} \sum_{\mathbf{r}_j} e^{i\mathbf{Q}\cdot\mathbf{r}_j} f_j(\mathbf{Q}) \underbrace{e^{i\mathbf{Q}\mathbf{u}_j(\mathbf{R}_n)}}_{\cong 1 + i\mathbf{Q}\mathbf{u}_j(\mathbf{R}_n)} \tag{4.6}$$

$$\cong \sum_{\mathbf{R}_n \in \mathscr{A}} e^{i\mathbf{Q}\cdot\mathbf{R}_n} \sum_{\mathbf{r}_j} e^{i\mathbf{Q}\cdot\mathbf{r}_j} f_j(\mathbf{Q})(1 + i\mathbf{Q}\mathbf{u}_j(\mathbf{R}_n))$$

$$= \sum_{\mathbf{R}_n,\mathbf{r}_j} e^{i\mathbf{Q}\cdot\mathbf{R}_n} e^{i\mathbf{Q}\cdot\mathbf{r}_j} f_j(\mathbf{Q}) + i\mathbf{Q} \sum_{\mathbf{R}_n,\mathbf{r}_j,k} \mathbf{e}_k e^{i(\mathbf{Q}\pm\mathbf{q}_k)\mathbf{R}_n} e^{i(\mathbf{Q}\pm\mathbf{q}_k)\mathbf{r}_j} f_j(\mathbf{Q}). \tag{4.7}$$

In the limit where the lattice becomes large the scattered intensity is then given by:

$$I(\mathbf{Q}) \sim \underbrace{\left|\sum_{\mathbf{r}_j} e^{i\mathbf{Q}\mathbf{r}_j} f_j(\mathbf{Q})\right|^2}_{|F_{\text{u.c.}}(\mathbf{Q})|^2} \sum_{\mathbf{G}_n} \delta(\mathbf{Q}-\mathbf{G}_n) + \\ + \sum_{\mathbf{G}_n,k} (\mathbf{Q}\mathbf{e}_k)^2 \underbrace{\left|\sum_{\mathbf{r}_j} e^{i(\mathbf{Q}\pm\mathbf{q}_k)\mathbf{r}_j} f_j(\mathbf{Q})\right|^2}_{|F'_{\text{u.c.}}(\mathbf{Q},\mathbf{q}_k)|^2} \delta(\mathbf{Q}\pm\mathbf{q}_k-\mathbf{G}_n). \quad (4.8)$$

The first term in Eq. 4.8 represents the usual scattering from the undistorted lattice with the corresponding Bragg peaks at the reciprocal lattice points $\mathbf{G}_n$. The intensity of the Bragg peaks is scaled by the geometric structure factor $F_{\text{u.c.}}$. As a consequence of the PLM a second term appears in Eq. 4.8 yielding peaks at $\mathbf{G}_n \pm \mathbf{q}_k$. These so-called superlattice peaks are usually much weaker than the Bragg peaks since their intensity scales as $(\mathbf{Q}\mathbf{e}_k)^2 \sim \mathbf{e}_k^2$ and $|\mathbf{e}_k| \ll 1$. This also means that the superlattice peak intensity increases with $\mathbf{Q}\mathbf{e}_k$ and if $\mathbf{Q}$ is perpendicular to the polarization of the PLM $\mathbf{e}_k/|\mathbf{e}_k|$ no superlattice peaks are observable. It is worth pointing out that the superlattice peak structure factor $F_{\text{u.c.}'}$ is of the same form as the Bragg peak structure factor $F_{\text{u.c.}}$. Given that $|\mathbf{q}_k| < |\mathbf{Q}|$ it is reasonable to assume that $f_j(\mathbf{Q}) \cong f_j(\mathbf{Q} \mp \mathbf{q}_k)$ and therefore $F_{\text{u.c.}} = F'_{\text{u.c.}}$. Accordingly, the superlattice peak intensity depends on the structure factor of the related Bragg peak, i. e., a strong Bragg peak will be surrounded by strong superlattice peaks.

In order to illustrate these features of the X-ray scattering from a modulated structure, the sum in Eq. 4.6 is explicitly evaluated for a finite 1D-lattice with two atoms in the unit cell in Fig. 4.1. The upper part depicts the modulation of the atomic positions in real space and the plot below shows the scattered X-ray intensity as a function of Q. It is clearly visible that not only Bragg peaks at $Q = 2\pi n/a$ but also superlattice peaks at $Q = 2\pi n/a \pm q$ appear. Furthermore, the intensity of the superlattice peaks increases with increasing Q since $\mathbf{Q}$ is parallel to $\mathbf{e}_k$. The position of the two atoms in the unit cell was chosen in a way that the geometric structure factor $F_{\text{u.c.}}$ vanishes for the Bragg peak at $Q = 4\pi/a$. In other words, the intensity of this Bragg peak is zero and – as can be seen in Fig. 4.1 – also the related superlattice peaks at $Q = 4\pi/a \pm q$ vanish. In Fig. 4.1 additional second order superlattice peaks at $Q = 2\pi n/a \pm 2q$ can be observed. These peaks do not appear in the analytical expression 4.7 because the exponential function containing the displacement $\mathbf{u}_j$ was expanded to first order only[2].

---

[2] A more sophisticated analysis shows that the intensity of the n^{th}-order superlattice reflection scales as the square of the corresponding Bessel function of first kind $J_n(\mathbf{Q}\mathbf{e}_k)^2$. In that context the 0-order reflections are the Bragg reflections. The Bessel functions are discussed in section 4.1.3 and are plotted on page 28 in Fig. 4.2. One

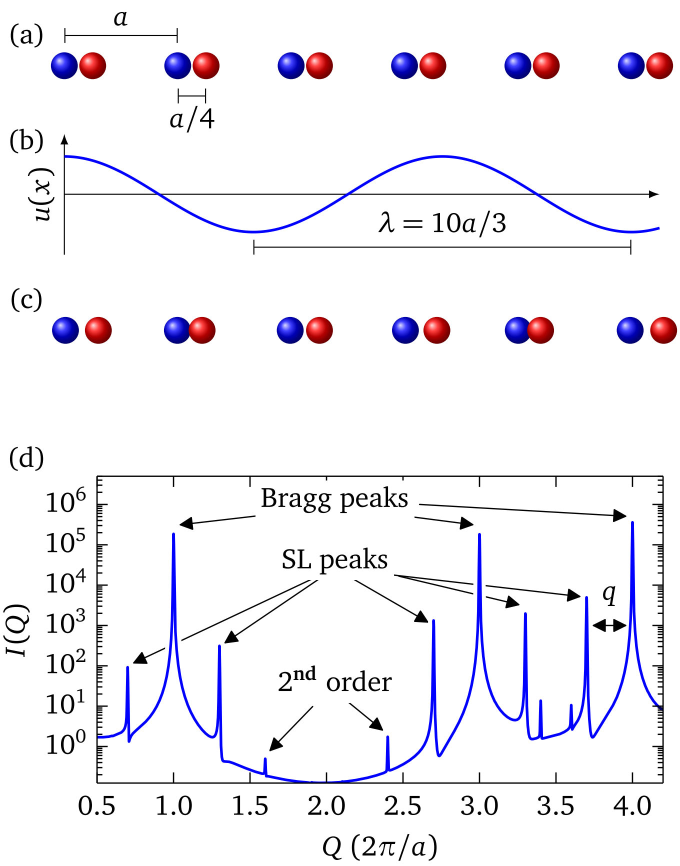

Figure 4.1: The X-ray intensity scattered from a modulated 1D lattice. A 1D lattice with lattice constant a and two atoms in the unit cell (a) is modulated by a PLM $u(x) = \hat{u}\cos(qx)$ with $q = 2\pi/\lambda = 0.3 \cdot 2\pi/a$ and $\hat{u} = 0.01$ (c). This modulation yields superlattice peaks around every Bragg peak (d) and is accompanied by a CDW (b). Note that since the structure factor vanishes for $q = 4\pi/a$ also the superlattice peaks at $4\pi/a \pm q$ become invisible. The intensity plot was obtained by numerical evaluation of the scattering amplitude 4.6 for a lattice of 500 unit cells. The atomic form factor f_j for both sites were taken to be unity. Since the numerical evaluation goes beyond the linear approximation of Eq. 4.7 also second order superlattice peaks at $2\pi n/a \pm 2q$ appear.

These considerations suggest that a measurement of the intensity and position of the superlattice peaks allows to determine the modulation wave vector and the amplitude of the corresponding PLM. This is still true for more complicated shaped modulation functions $\mathbf{u}_j(\mathbf{r})$.

It was pointed out earlier that an incommensurate PLM breaks the translation symmetry of the crystal. This makes it very difficult to perform crystallographic refinements because no real unit cell exists. However, it is possible to restore the translation symmetry by formally describing the system in an higher-dimensional space, as first pointed out by de Wolff *et al.* [70]. This

---

may clearly observe that $J_1(x) \propto x$ for small x and therefore the intensity of the first order superlattice reflection scales as $(\mathbf{Q}\mathbf{e}_k)^2$ in line with the result obtained by expanding the exponential function in Eq. 4.6.

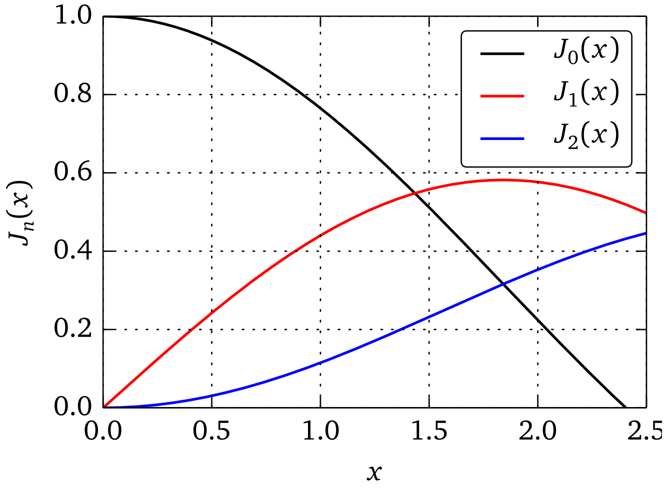

Figure 4.2: Bessel functions of first kind for $n = 0, 1$ and 2. For small x the magnitude of $J_n(x)$ rapidly decreases with increasing n. Note that $J_0(x = 0) = 1$ but $J_m(x = 0) = 0, \forall m \neq 0$.

approach introduces an extra dimension perpendicular to the 3D reciprocal space for every incommensurate PLM yielding a $(3+d)$ dimensional superspace, where d is the number of independent PLMs. It turns out that the projection of a $(3+d)$ dimensional reciprocal lattice to 3 dimensions corresponds to the positions of the Bragg and superlattice peaks. In other words, it is possible to index the position of all diffraction peaks with $(3+d)$ indices. The direct lattice corresponding to this reciprocal lattice defines a periodic crystal lattice in $(3+d)$-dimensional superspace. Based on this approach the superspace crystallography provides an efficient tool to analyze incommensurately modulated structures but also quasicrystals and composite crystals. A more profound introduction is beyond the scope of this chapter and may be found in reference 71.

4.1.3 Scattering from discommensurations

In chapter 2.4 it was pointed out that a CDW with a modulation wave vector which is close to a commensurate vector tends to develop discommensurations due to the interaction with the crystal lattice. These discommensurations represent phase slips in the homogeneous CDW which separate commensurate regions. In the simplest case the PLM associated with a phase modulated 1D-CDW may be expressed as:

$$u(x) = \hat{u}(e^{iq_c x+\eta(x)} + \mathrm{c.\,c.}), \tag{4.9}$$

where $q_c = (N/M)a^*$ corresponds to a commensurate wave vector with a^* being the shortest reciprocal lattice vector and N, M are integers. According to the example used in section 2.4

we pick the particular values: $N = 1$ and $M = 3$. As outlined in section 2.4 the function $\eta(x)$ describes the phase modulation and may be expanded as:

$$\eta(x) = \delta x + \sum_{l=1}^{\infty} A_l \sin(Ml\delta x). \tag{4.10}$$

In order to obtain some analytical insights how such a phase modulation affects the diffraction pattern it is instructive to consider only the first Fourier component in Eq. 4.10. In this case the structure factor is given to leading order in $\hat{u}$ for the superlattice peaks ($\mathbf{Q} \neq \mathbf{G}_n$) by:

$$S(Q) = i(Q\hat{u}) \sum_n e^{iQn} (e^{i(q_c n + \delta n)} e^{iA\sin(3\delta n)} + \text{c. c.}), \tag{4.11}$$

where we explicitly inserted $M = 3$. The exponential function containing the sine function may be transformed using the Jacobi-Anger identity:

$$e^{iz\sin\Theta} = \sum_{n=-\infty}^{\infty} J_n(z) e^{in\Theta}, \tag{4.12}$$

where J_n are the Bessel functions of the first kind. With the help of this expression the structure factor is given by:

$$S(Q) = i(Q\hat{u}) \sum_n \sum_{m=-\infty}^{\infty} e^{i(Q \pm q_c \pm \delta \pm m3\delta)n} J_m(A). \tag{4.13}$$

The sum over n produces superlattice reflections at

$$Q = q_{DC}^m \equiv q_c + \delta + 3m\delta, m \in \mathbb{Z}, \tag{4.14}$$

with intensities proportional to $J_m(A)^2$. In other words, the main superlattice reflection ($m = 0$) shifts by the distance δ away from the commensurate position q_c. In addition, higher order superlattice reflections ($m \neq 0$) appear although only the leading order in the modulation amplitude $\hat{u}$ was considered. This is a direct consequence of the phase modulation and is well known from signal theory of frequency modulated signals. The Bessel functions $J_n(x)$ have the property that, for small x, they rapidly decay with increasing order n and, hence, the intensity of the higher order superlattice reflections decreases rather fast. This behavior may be observed in Fig. 4.2 which shows a plot of $J_n(x)$ for $n = 0, 1, 2$. It is easy to show that higher order terms ($l > 1$) in Eq. 4.10 do not generate new peaks. Rather they solely modify the intensity of the already existing superlattice peaks corresponding to q_{DC}^m.

Fig. 4.3 illustrates the properties of the X-ray scattering from a modulated 1D lattice hosting discommensurations. In the commensurate case the modulation function $\eta(x)$ is equal to 0 and the corresponding superlattice peak appears at q_C. A smooth incommensurate PLM

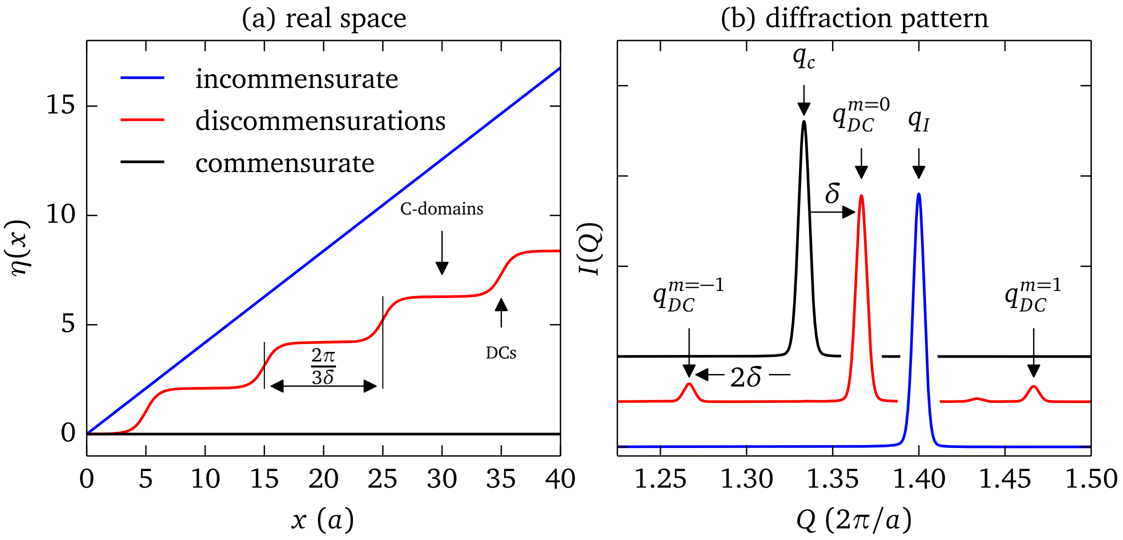

Figure 4.3: The X-ray intensity scattered from a modulated 1D lattice with discommensurations. (a) shows $\eta(x)$ (Eq. 4.10) for the commensurate (black), smooth incommensurate (blue) and the modulated (red) case with discommensurations in real space. (b) shows the corresponding superlattice reflections in the diffraction pattern. For the incommensurate case only a shift of the superlattice reflection is observed. The discommensurations lead to a shift of the main superlattice reflection ($m = 0$) along with the appearance of relatively strong higher order superlattice reflections ($m = \pm 1$). In real space (a) the discommensurations are the smooth steps in $\eta(x)$ and the flat plateaus in-between are called commensurate domains (C-domains). Note that the Y-axis scaling of the right plot is linear as opposed to the plot in Fig. 4.1. The scattered intensity was obtained in the same way as in Fig. 4.1.

implies that $\eta(x)$ is a linear function of x and the superlattice peak merely shifts to q_I. The discommensurations deform $\eta(x)$ to a step-like function as shown in the left panel of Fig. 4.3. As a result the main superlattice reflection shifts away from q_C to $q_{DC}^0 = q_C + \delta$ and rather intense higher order superlattice peaks occur at $q_{DC}^{-1} = q_C - 2\delta$ and $q_{DC}^1 = q_C + 4\delta$ as expected from Eq. 4.14. It is worth noting that the PLM hosting discommensurations is locally commensurate. This means that all plateaus of $\eta(x)$ correspond to commensurate regions which are separated by the discommensurations. Nonetheless, in the diffraction pattern no superlattice peak appears at q_C, rather the peak is shifted by δ.

The fingerprint of discommensurations in the XRD will be of immediate importance for the discussion of the nearly commensurate CDW phase of 1T-TaS$_2$ and its pressure dependence in chapter 4.3. For this discussion it is important to note that the intensity ratio between first and higher order superlattice peaks crucially depends on the sharpness of the discommensurations. As illustrated in Fig. 4.4 the intensity of the higher-order superlattice peaks at $q_{DC}^{-1} = q_C - 2\delta$ and $q_{DC}^1 = q_C + 4\delta$ decreases when the discommensurations smear out. At the same time the intensity of the first order superlattice peak at $q_{DC}^0 = q_C + \delta$ increases. In the case where

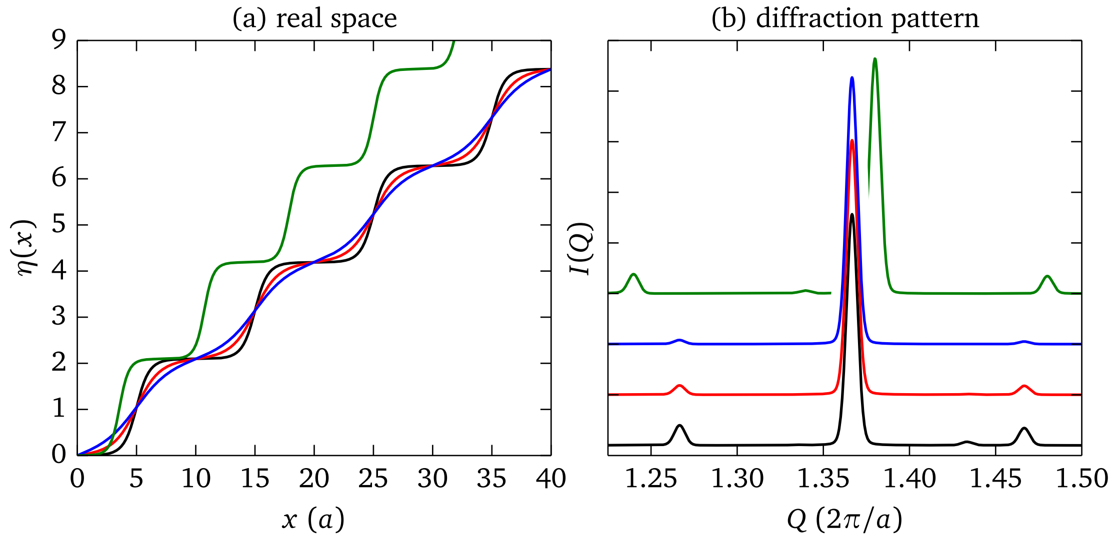

Figure 4.4: Influence of the sharpness of the discommensurations on the superlattice peak intensities. Sharp discommensurations yield intense higher-order superlattice peaks (black line). When the sharp discommensurations smear out, the corresponding higher-order superlattice peaks become increasingly weaker (red and blue line). When only the distance between the discommensurations changes the superlattice peak intensities do not change and solely the peak positions shift (green line).

only δ and accordingly the distance between discommensurations changes, the intensity ratio remains as it is and solely the superlattice peak positions shift.

4.2 High-pressure X-ray diffraction

In this section we will briefly explain the experimental setup employed to obtain XRD data as a function of pressure and temperature. As discussed in section 4.1.1 the superlattice peaks associated with CDWs are relatively weak. In order to measure these signals in a complex sample environment (pressure cell and cryostat) it is necessary to use a synchrotron radiation source. Hence, the majority of the XRD measurements presented in this chapter were conducted at the beamline ID09 of the European Synchrotron Radiation Facility (ESRF) in Grenoble. Fig. 4.5 shows the experimental setup used at ID09.

The high-quality single crystals used for the present XRD studies were grown by the iodine vapor transport method as described in reference 72. Oriented samples of about 80 μm diameter were loaded in a membrane driven diamond anvil pressure cell (DAC) filled with helium as the pressure transmitting medium. The working principle of the DAC is schematically illustrated in Fig. 4.6. For the low-temperature measurements the pressure cell was then installed in a continuous He-flow cryostat and exposed to a 10×10 μm^2 beam with a photon

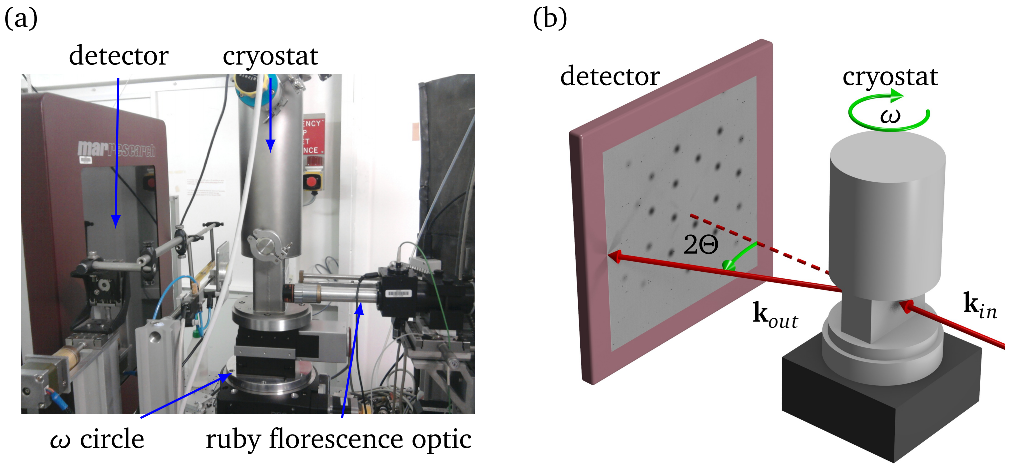

Figure 4.5: XRD setup at ID09 of the ESRF. A photograph of the end station is shown in (a). The scattering geometry is illustrated in (b). The setup allowed for sample rotations about the ω-axis. A MAR555 flat panel detector was used to collect the diffraction data up to $2\Theta \approx 20°$.

energy of 30 keV. A MAR555 flat panel detector was used to collect the diffraction data in large regions of reciprocal space. At each pressure, we collected a dataset of 120 images over a sample rotation of 60° with 0.5° scan width per image. The raw data (detector images) represent curved slices in reciprocal space according to the corresponding surface of the Ewald sphere and are not suited for a direct interpretation. Therefore it is necessary to transform the recorded intensity data onto a rectangular grid in reciprocal space – a procedure called *unwarp*. For this purpose the software package CrysAlisPRO [73] was employed.

We increased the pressure up to 15 GPa and 8 GPa at constant temperatures of 300 K and 15 K, respectively, and monitored the pressure *in situ* using the ruby fluorescence as described in references 74 and 75. During the low-temperature measurements we also cooled the sample to 3.5 K at every pressure point above 4 GPa, in order to reach the superconducting phase.

In addition to these measurements, the C-NC transition at lower pressures was investigated at beamline BW5 of the storage ring DORIS at the Deutsches Elektronen-Synchrotron (DESY) in Hamburg. This endstation is equipped with a triple-crystal diffractometer along with a solid-state point detector as described in reference 76. The advantage of such a setup is the very high **q**-resolution as compared to the area detector setup used at ID09. In addition, the signal to noise ratio is very good due to the analyzer crystal. For this experiment we used a clamp-type pressure cell [77] and performed measurements as a function of temperature at constant pressure.

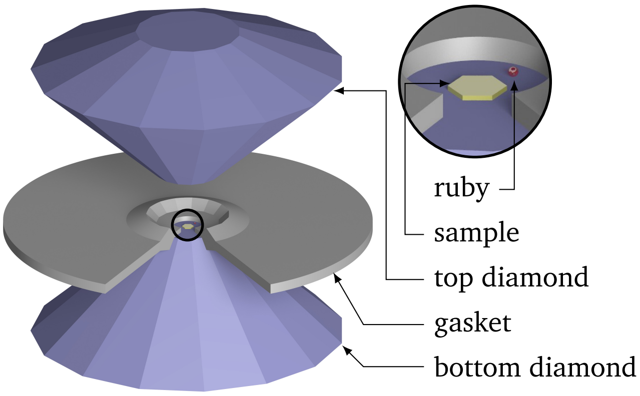

Figure 4.6: Diamond anvil pressure cell (DAC). The sample is located within a small hole (diameter $\approx 300\ \mu$m) in a gasket in-between two diamond anvils. The black circle in the left image indicates the region which is magnified in the right image. A force can be applied to the top anvil via a membrane, which increases the hydrostatic pressure within the pressure transmitting medium (Helium) and, hence, on the sample. A ruby crystal next to the sample serves as a pressure gauge.

4.3 Pressure dependence of the nearly commensurate CDW in 1*T*-TaS$_2$ and its relation to superconductivity

In this section we investigate the relation between CDW and superconductivity in 1*T*-TaS$_2$. As outlined in section 3.2.3 Sipos *et al.* deduced – based on detailed resistivity measurements – a microscopic scenario for superconductivity in 1*T*-TaS$_2$, according to which superconductivity develops in metallic regions (discommensurations) that separate insulating C-CDW domains and grow with increasing pressure [45]. In other words, the pressure induced superconductivity and its coexistence with CDW order was explained in terms of a microscopic phase separation in real space. It is clear, however, that macroscopic measurements cannot provide information about the microscopic spatial structure of the CDW. Since this information is essential in order to understand the coexistence of superconductivity and CDW in 1*T*-TaS$_2$, we investigated the CDW order by means of XRD experiments as a function of pressure and temperature.

The reflections observed in XRD allow to determine the spatial arrangement of the lattice sites in a solid. In a CDW material Bragg reflections which are related to the underlying average structure can be generally observed. The CDW induces additional modulations of that structure and since the period of the CDW in real space is larger than that of the underlying lattice, additional reflections appear around the Bragg peaks. These are referred to as superlattice or satellite reflections. The position, intensity and width of the satellite reflections provides direct information about the spatial structure, the amplitude and the correlation length of the CDW (see section 4.1.1).

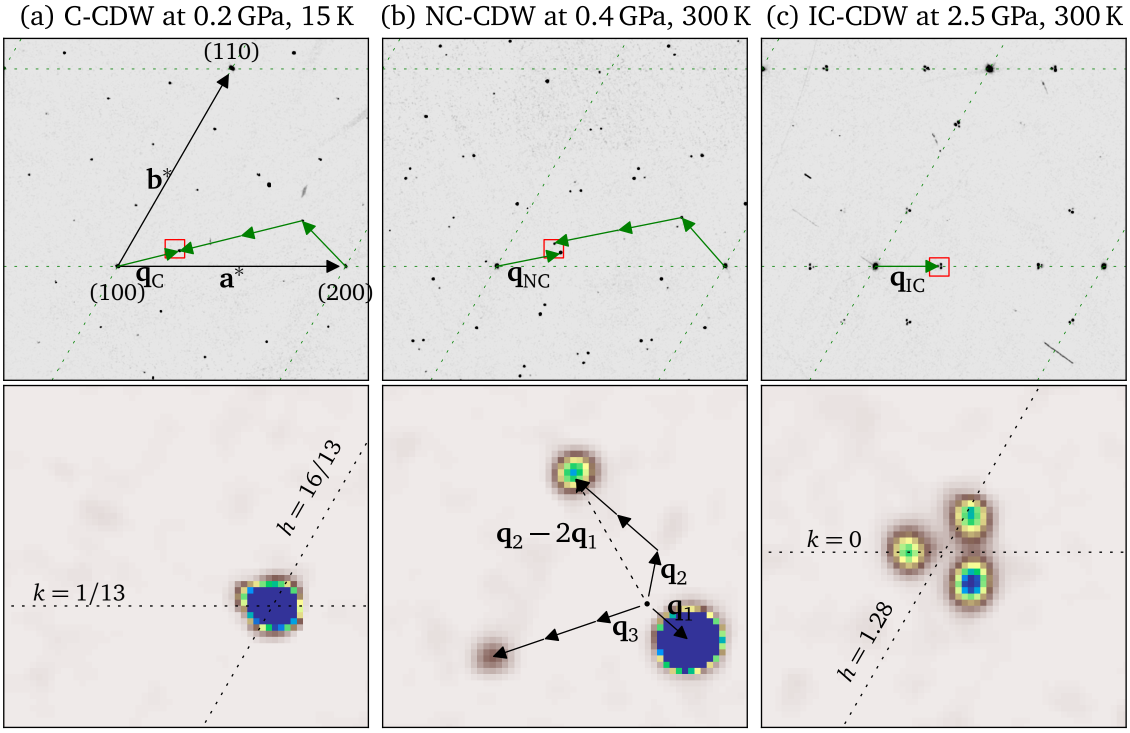

Figure 4.7: Reciprocal space maps of the XRD intensity for the C-CDW (a), the NC-CDW (b) and the high-pressure IC-CDW (c). In (a) the Bragg reflections are indicated by the Miller indices (hkl) and the reciprocal lattice vectors $\mathbf{a}^*$, $\mathbf{b}^*$ of the hexagonal plane are shown by black arrows. A magnified region (marked by red rectangles) in reciprocal space is displayed in the lower panel, where the threefold splitting of the satellite reflections for the NC-CDW and the high pressure IC-CDW can be clearly observed.

The XRD intensity was recorded as a function of the scattering vector $\mathbf{Q}$, which is commonly given in terms of the Miller indexes (hkl): $\mathbf{Q} = h\,\mathbf{a}^* + k\,\mathbf{b}^* + l\,\mathbf{c}^*$ with $\mathbf{a}^*$, $\mathbf{b}^*$ and $\mathbf{c}^*$ the reciprocal lattice vectors of the unmodulated structure (cf. Fig. 4.7 (a)). Since the satellite reflections in 1T-TaS$_2$ occur at different none-zero l-values [55], we integrated the scattered intensity along the l-direction, resulting in diffraction pattern that correspond to projections of the X-ray intensity within a slice of thickness $\Delta l = 2/3$ onto the hk-plane in reciprocal space. Typical XRD datasets obtained in this way are presented in Fig. 4.7, where the additional satellite reflections around every Bragg peak can be clearly observed.

4.3.1 Phase transitions observed in X-ray diffraction

In Fig. 4.8 we show the electronic pressure-temperature phase diagram as deducted from resistivity measurements [45] supplemented with transition temperatures established in the present thesis.

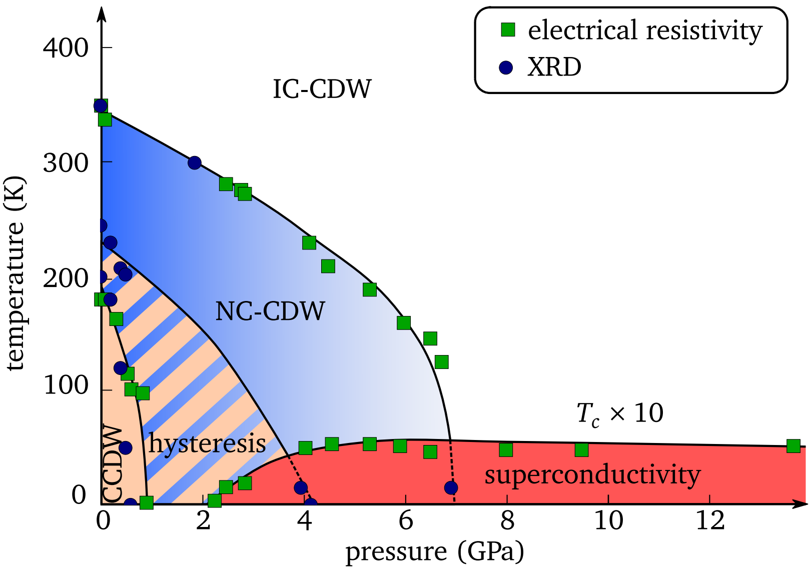

Figure 4.8: Schematic electronic pressure-temperature phase diagram of 1T-TaS$_2$ as established by means of electrical resistivity measurements [45] supplemented with transition temperatures obtained in this study. The C-CDW is characterized by a large hysteresis as illustrated by the hatched area.

The diffraction pattern taken at 300 K and close to ambient pressure is shown in Fig. 4.7 (b). Under these conditions the NC-CDW is characterized by a wave vector $\mathbf{q}_{\mathrm{NC}}$, which deviates slightly from the commensurate wave vector $\mathbf{q}_{\mathrm{C}}$. As illustrated in Fig. 4.7 (b), the small incommensurability of $\mathbf{q}_{\mathrm{NC}}$ results in two third order satellite peaks close to the first order peak. The observation of strong higher order satellite reflections verifies that the NC-CDW is characterized by a domain-like structure with sharp boundaries [55]. In fact, these sharp boundaries are the discommensurations introduced in section 2.4. The occurrence of the strong higher order superlattice peaks is directly related to the discommensurations as explained in section 4.1.3. It can be seen in Fig. 4.7 (a) that the incommensurability and the resulting splitting of the satellite peaks vanishes in the C-CDW phase, which is reached when the sample is cooled down while keeping the pressure close to ambient pressure (vertical path close to p=0 GPa in Fig. 4.8). This phase is characterized by a commensurate wave vector $\mathbf{q}_{\mathrm{C}}$ in the hk-plane. Perpendicular to the hk-plane, i. e. along the l-direction, the corresponding superlattice peaks are very broad indicating that the CDW layer stacking is disordered. The CDW layer stacking will be discussed thoroughly in section 4.5.

By keeping the temperature constant at room temperature and increasing the pressure, the IC-CDW is reached in agreement with earlier reports (horizontal path close to T=300 K in Fig. 4.8). However, as shown in the bottom panel of Fig. 4.7 (c), the pressure-induced IC-

CDW differs from the one at ambient pressure as it shows an additional splitting of the satellite reflections within the *hk*-plane. This observation is in accordance with a previous study [78]. The incommensurate CDWs at high pressure are not shown in Fig. 4.8 but will be investigated separately in section 4.4.

4.3.2 The pressure dependence of the nearly commensurate phase

The effect of increasing pressure at constant temperature on the wave vector $\mathbf{q}_{\mathrm{NC}}$ is presented in Fig. 4.9 (a) and (b). We determined the peak positions by fitting 2D-Gaussian profiles to the measured diffraction pattern, including up to 50 first order and 25 third order satellite reflections. This enabled us to determine the peak positions with high accuracy. As can be observed in Fig. 4.9 (a) and (b), the position of the satellite reflections clearly changes upon increasing the pressure, which corresponds to $\mathbf{q}_{\mathrm{NC}}$ moving towards $\mathbf{q}_{\mathrm{IC}}$. For geometrical reasons the shift in position is more pronounced for the third order satellite reflections (cf. Fig. 4.9 (a) and (b)). The shift in position together with the behavior of the peak width and intensity is illustrated in Fig. 4.9 (c), which shows scans along the reciprocal *k*-direction. Not only the peak shifts according to the change of $\mathbf{q}_{\mathrm{NC}}$ but also the intensity of the reflection is strongly suppressed, revealing a pronounced reduction of the CDW amplitude. The analysis of the peak profiles, however, does not show any significant broadening of the peaks, i. e. no change in the coherence length of the CDW is observed.

The in-plane components of the modulation wave vector determined by the fitting procedure are summarized quantitatively for the measurement at room temperature and at 15 K in Fig. 4.10. Starting with the low-temperature data set, the C-NC transition is observed close to 4 GPa with increasing pressure. Within the NC-CDW phase, the $\mathbf{q}_{\mathrm{NC}}$ moves clearly towards $\mathbf{q}_{\mathrm{IC}}$ without reaching it completely. Then at about 7 GPa a sudden jump of the modulation vector to $\mathbf{q}_{\mathrm{IC}}$ signals a first order transition to the IC-CDW phase (the threefold splitting is neglected and only the midpoint is shown). A corresponding behavior of the NC-IC transition is observed at room temperature. These data agree very well with the pressure-temperature phase diagram deduced from resistivity measurements as illustrated in Fig. 4.8.

It is remarkable that the CDW remains commensurate up to 4 GPa, when the pressure is increased at constant $T=15$ K, because the C-CDW is suppressed already at 0.6 GPa for temperature sweeps at constant pressure. This was shown by resistivity measurements [45, 53] and also verified by our XRD. Both experiments also showed a very large differences for the transition temperatures, depending on whether the sample is cooled or heated at constant pressure. These observations imply that the C-CDW is metastable in a large pressure-temperature region (cf. Fig. 4.8).

In order to search for possible changes of the CDW order in the superconducting phase,

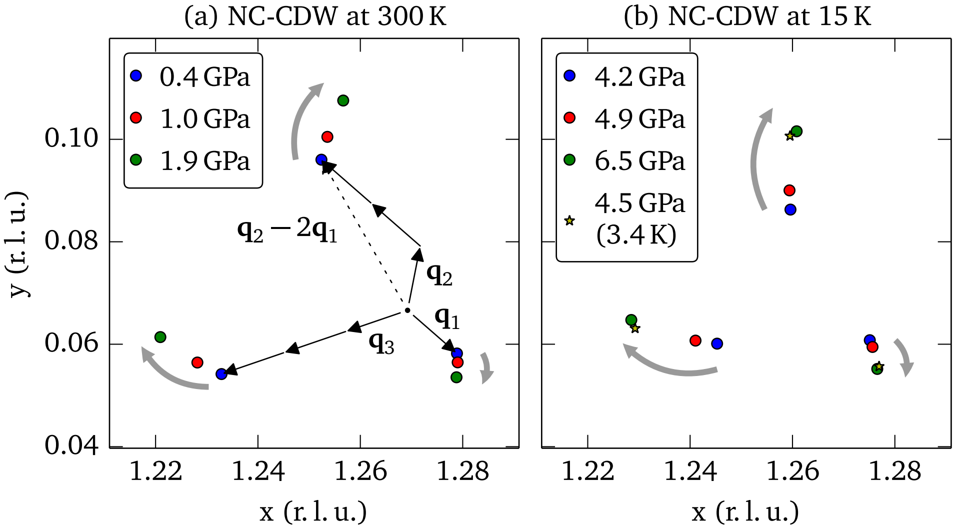

(c) NC-CDW at 300 K

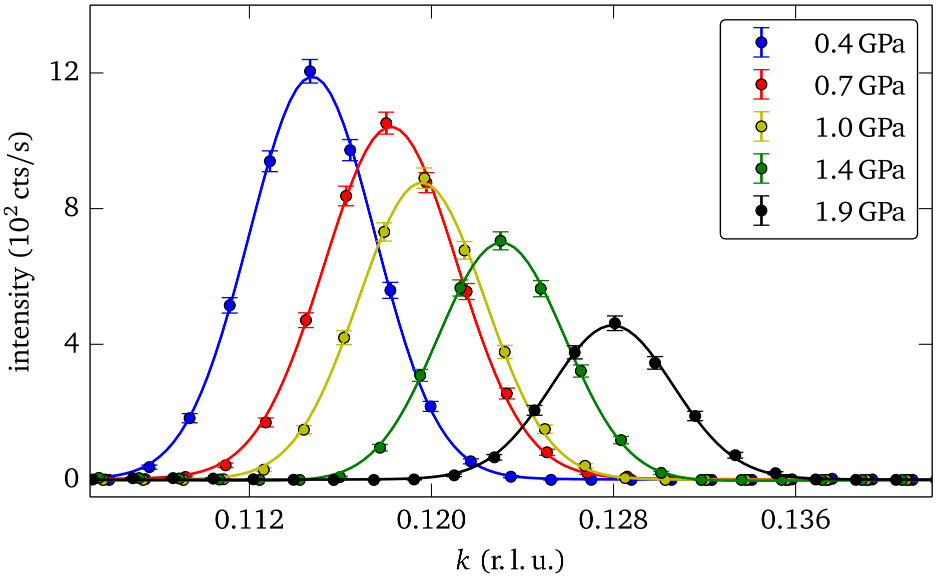

Figure 4.9: The superlattice peak positions in the NC phase as a function of pressure at 300 K (a) and 15 K (b), respectively. In (a) $\mathbf{q}_1 = \mathbf{q}_{NC} - \mathbf{q}_C$ and rotating $\mathbf{q}_1$ by 120° and 240° yields $\mathbf{q}_2$ and $\mathbf{q}_3$, respectively. At both 300 K and 15 K, the modulation wave vector clearly shifts towards the IC-position with increasing pressure. Additionally, (b) includes data taken in the superconducting region of the phase diagram at 4.5 GPa and 3.4 K. (c) shows k-scans through the 3$^{\mathrm{rd}}$ order satellite peak versus pressure at T=300 K, illustrating that peak position and intensity are clearly pressure-dependent. The solid lines represent fitted pseudo-Voigt profiles.

we cooled the sample from 15 K down to ≈ 3.5 K at every pressure point within the NC-CDW phase. However, no significant change of the CDW order could be detected upon entering the superconducting region of the phase diagram (cf. star marker in Fig. 4.9 (b)). Note that upon

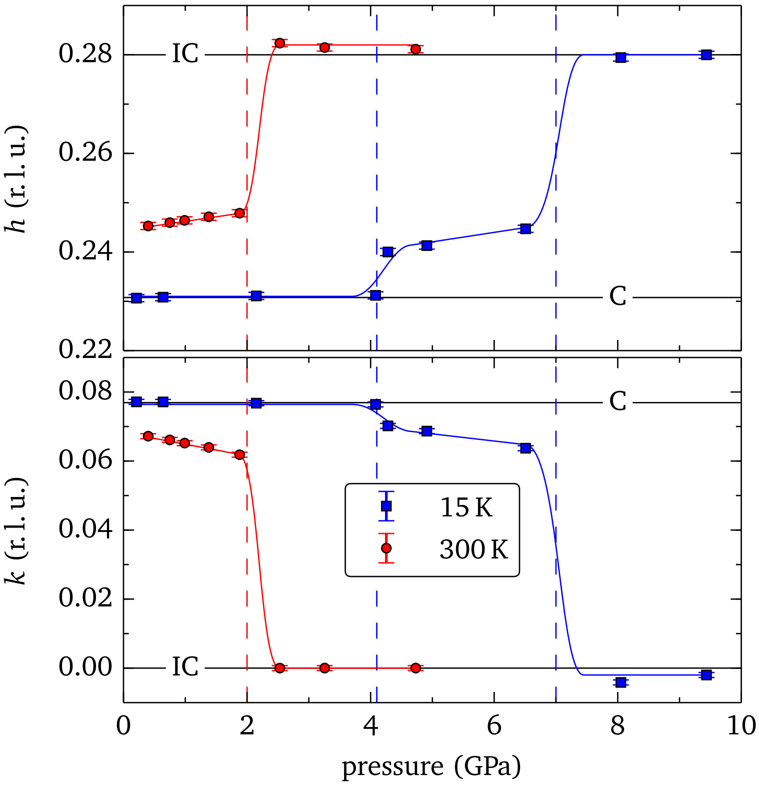

Figure 4.10: In plane components of the modulation wave vector as a function of pressure. Closed circle markers and square markers represent the room and low temperature measurement, respectively. At room temperature the NC-IC-transition occurs at $p \approx 2$ GPa (red dashed line). For low temperatures we observed the C-NC-transition and the NC-IC-transition at about 4 GPa and 7 GPa, respectively (blue dashed lines). Within the NC-CDW phase the **q**-vector shifts towards $\mathbf{q}_{\mathrm{IC}}$. Solid lines are guides to the eye.

cooling to the lowest temperature, the pressure decreased as well. Yet no significant changes of the CDW order were observed, which we attribute to hysteresis effects.

4.3.3 Coexistence of charge density wave order and superconductivity

We now turn to the discussion of the presented XRD results and their implications for the coexistence of superconductivity and CDW in 1*T*-TaS$_2$. As already mentioned in section 3.2, the pressure-induced superconductivity in this compound was recently explained in terms of a phase separation scenario, which is based on the microscopic structure of the NC-CDW [45]. The NC-CDW at ambient pressure is characterized by hexagonally shaped C-CDW domains separated by domain boundaries, which are also called discommensurations [41, 55, 64–66, 79, 80]. The latter are commonly regarded as charged and metallic regions in-between C-CDW domains [45]. However, it is important to realize that this is not a domain structure in the usual sense, because the C-CDW domains have a well-defined shape and size and, importantly, their spatial arrangement is periodically ordered. As a result, the C-CDW domains and the domain boundaries together form a regular Kagome lattice with a large coherence length, yielding sharp satellite reflections in reciprocal space (cf. section 4.1.3).

It was shown previously [80] that the average distance R of neighboring C-CDW domains (see Fig. 4.11) is directly related to the incommensurability of the CDW via

$$R = \frac{8\pi}{3\sqrt{13}\cdot|\mathbf{q}-\mathbf{q}_C|}, \tag{4.15}$$

where R is given in lattice units, $\mathbf{q}$ is the measured modulation vector and $\mathbf{q}_C$ is the modulation vector of the commensurate phase. In addition to this, the sharpness of the C-domain boundaries determines the intensity ratio between first and higher order satellite reflections. This relation was shown for the one-dimensional case in section 4.1.3 (cf. Fig. 4.4 on page 31).

According to the scenario proposed in reference 45, the insulating C-CDW domains shrink with increasing pressure and, hence, the metallic domain boundaries widen and become interconnected as sketched in Fig. 4.11 (d). At a certain pressure, superconductivity can eventually occur at low temperature within the connected metallic regions. In this scenario, R will remain essentially constant with increasing pressure. Furthermore, the widening of the domain walls corresponds to smooth boundaries between neighboring C-CDW domains, which will result in a substantial change of the intensity ratio between the first and third order satellite reflection I_1/I_3. As can be seen in Fig. 4.11 (a) and (b) these two characteristic changes are not observed. Instead, we find a clear reduction of R and a constant I_1/I_3 ratio within the errors of the experiment. Our data therefore does not agree with the scenario illustrated in Fig. 4.11 (d).

The constant I_1/I_3 shows that the boundaries between neighboring C-CDW domains remain sharp, while R and with it the size of the C-CDW domains shrink with increasing pressure. Our results hence imply that the spatial structure of the CDW changes as illustrated in Fig. 4.11 (e). Furthermore, the data in Fig. 4.11 (c) shows that the intensity of the satellite reflections decreases by a factor of 3, i. e., the overall amplitude of the lattice modulation decreases by $\approx 1/\sqrt{3}$ with pressure.

The shrinking of the C-CDW domains and the reduction of the CDW-amplitude observed by XRD agrees with the conclusions reported previously in reference 45. The important new result here is that the domain boundaries in the NC-CDW phase do not form large interconnected metallic regions. We also do not observe a dissociation of the C-CDW domains, which would result in a strong broadening and, eventually, the disappearance of the NC-superlattice reflections. Instead, the sharp XRD peaks in the NC-CDW phase prove that the metallic regions and

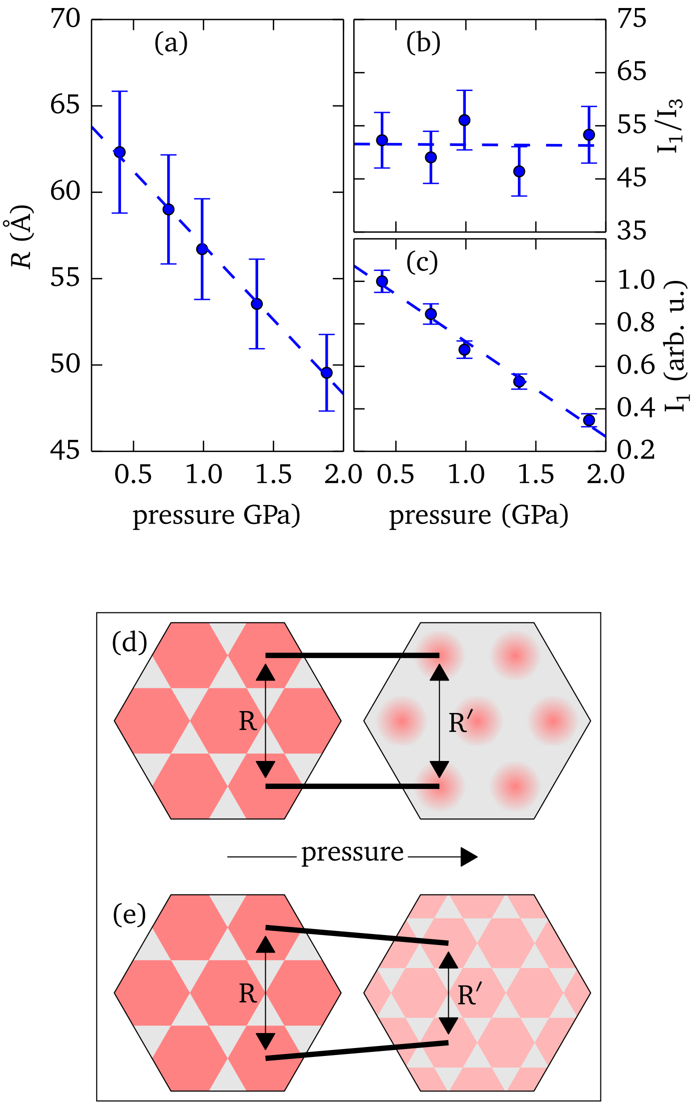

Figure 4.11: Possible scenarios of C-domain shrinking. (a): Calculated C-domain distance as a function of pressure using Eq. 4.15. (b): Intensity ratio between the first and third order satellite reflection. Dashed lines are guides to the eye. (d) and (e) illustrate two possible scenarios of pressure-induced C-domain shrinking in real space. The dark and light red hexagons refer to C-domains where dark red means large CDW amplitude and light red corresponds to a smaller CDW amplitude. The gray areas represent the discommensurations. (d): The distance between C-domains remains constant and the domain boundaries smear out. In (e) the C-domain distance shrinks and the domain boundaries remain sharp.

the C-CDW domains in this phase always form a long-ranged ordered and periodic structure.

The pressure-induced formation of large metallic regions therefore seems not to be crucial for the superconductivity in 1*T*-TaS$_2$. Rather, the behavior illustrated in Fig. 4.11 (e) requires that the ordered structure as a whole becomes superconducting. In other words, not only the metallic regions support superconductivity, but the whole NC-CDW structure illustrated in Fig. 4.11 (e) forms a coherent macroscopic superconducting state. The same conclusion was recently also reached for the superconducting phase that is induced in 1*T*-TaS_2 by a subtle substitution of Iron for Tantal: From a completely different point of view, namely that of angle-resolved photoemission spectroscopy, Ang *et al.* also found that the NC-CDW and superconductivity must coexist in real space [48]. Our results for the pressure-induced superconductivity together with the study of Fe-induced superconductivity by Ang *et al.* provide solid experimental evidence for superconductivity occurring in the NC-CDW structure as a whole – a situation which is fundamentally different from the previously proposed phase separation in real space. The essentially pressure-independent superconducting transition temperature T_c, together with the pressure-induced changes of the NC-CDW observed here, further implies that NC-CDW and superconductivity are not competing. We therefore argue that instead of a phase separation in real space there is a phase separation in k-space: NC-CDW gap and superconductivity gap occur in separate regions of the Fermi surface.

While the same should also be true for the IC-CDW, according to the pressure-temperature phase diagram, the Mott C-CDW clearly competes with superconductivity. Most likely the C-CDW completely gaps the Fermi surface and hence leaves no states for the superconducting condensate. Further dedicated studies of the electronic structure as a function of pressure are however necessary to verify these conjectures. Notwithstanding the obvious competition between the Mott C-CDW and superconductivity, it remains to be clarified whether or not electron-electron interactions are relevant for the superconductivity in 1*T*-TaS_2. This issue will be discussed more detailed in chapter 5. We believe that the superconducting CDW in 1*T*-TaS_2 can serve as a viable model which will help to understand other complex materials, sharing the same pathology such as the high-temperature cuprate superconducters.

4.4 Incommensurate charge density waves at high pressure

As already mentioned in section 4.3 the incommensurate CDW at high pressure and room temperature differs from the incommensurate CDW at ambient pressure and high temperature. Moreover, it turns out that there are at least three distinct incommensurate orderings apart from the nearly commensurate CDW. In this section we will summarize and discuss the experimental results obtained for these phases.

4.4.1 Splitting of the superlattice peaks as a function of pressure

Fig. 4.12 provides an overview of reciprocal space maps recorded within the different incommensurate phases. For convenience the pressure-temperature points at which the data were measured are indicated in a schematic phase diagram in Fig. 4.12 (a). The reciprocal space

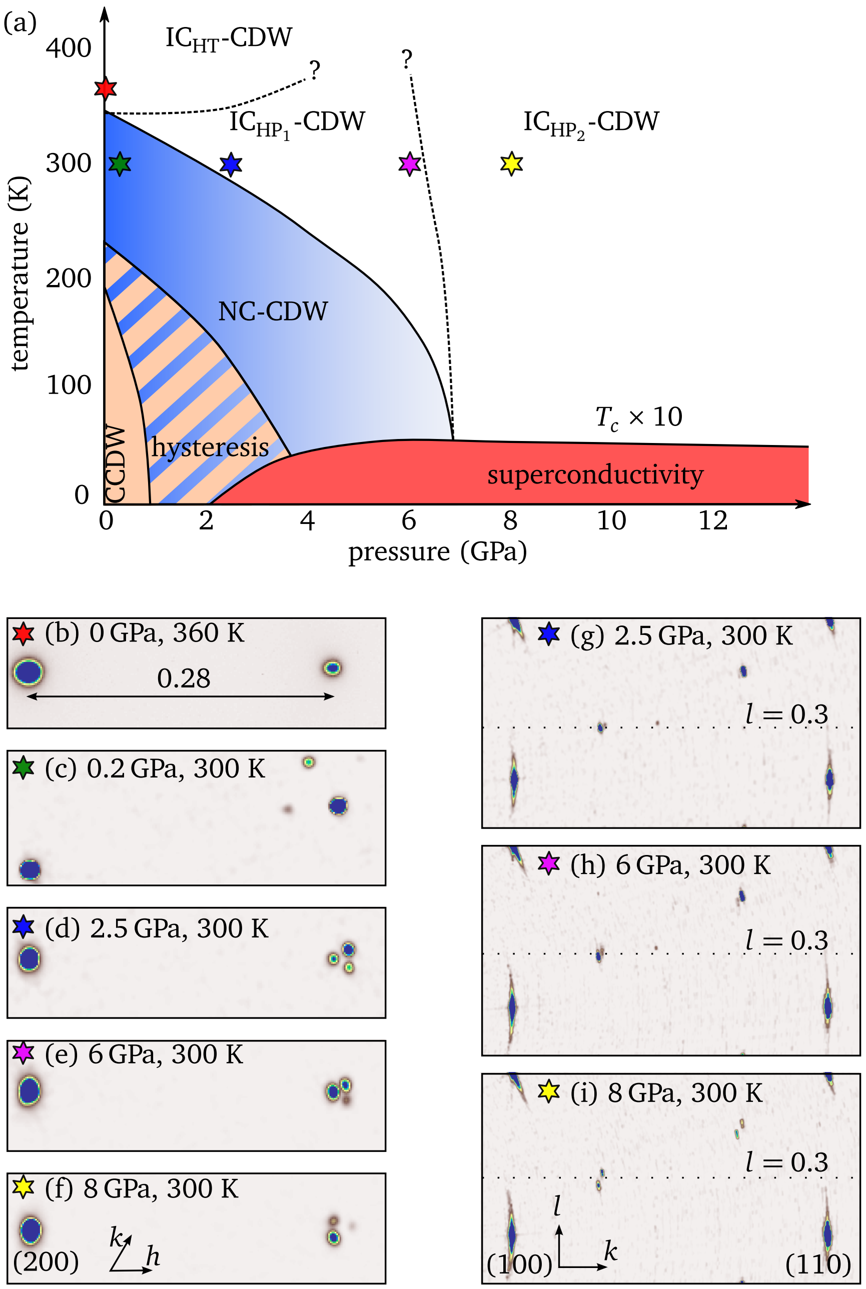

Figure 4.12: Reciprocal space maps for the various incommensurate CDW phases observed in 1*T*-TaS$_2$. (a) shows a schematic electronic phase diagram. Reciprocal space maps of the *hk*-plane and *kl*-plane are shown in (b)-(f) and (g)-(i), respectively. The pressure-temperature points at which the data were recorded are indicated by colored stars in (a). The different incommensurate phases are characterized by different splittings of the superlattice reflections.

maps shown in Fig. 4.12 (b)-(f) correspond to the *hk*-plane and are similar to those presented in Fig. 4.7. It is clearly visible that all CDWs at room temperature are governed by a splitting of the superlattice peaks. We have seen in section 4.1.3 that such splittings may be associated with well-ordered defects (discommensurations) of the CDW phase. Since these defects form a long-ranged ordered lattice the corresponding diffraction peaks are sharp. It was also shown that the distance between the split peaks is inverse proportional to the period of the defect lattice. In other words, large defect lattice periods cause small splittings and vice versa. We will take up these interesting considerations in relation to the incommensurate CDWs of $1T$-TaS_2 in section 4.4.3 but for now we solely focus on the experimental findings.

For the NC-CDW (Fig. 4.12 (c)) the splitting of the superlattice peaks is pressure-dependent and discussed thoroughly in section 4.3. Fig. 4.12 (d) reveals that the incommensurate phase reached by increasing the pressure to ≈ 2.5 GPa also features a threefold splitting of the superlattice peak, in line with the observation reported in reference 78. Apparently, such a splitting does not occur in the high-temperature phase ($\mathrm{IC_{HT}}$ at 360 K) as can be seen in Fig. 4.12 (b). We will call this phase $\mathrm{IC_{HP_1}}$. At 6 GPa (Fig. 4.12 (e)) the splitting of the superlattice peak is in principle the same as at 2.5 GPa, although the intensities change somewhat and the three peaks move together slightly. However, at 8 GPa (Fig. 4.12 (f)) the diffraction pattern changes significantly: While the superlattice peak splitting is still threefold, the arrangement of the three peaks is now different, giving reason to name this phase $\mathrm{IC_{HP_2}}$. The transition from $\mathrm{IC_{HP_1}}$ to $\mathrm{IC_{HP_2}}$ also effects the out-of-plane component l of the superlattice peaks as can be observed in Fig. 4.12 (h) and (i): At 2.5 GPa and 6 GPa the superlattice peaks of the $\mathrm{IC_{HP_1}}$ phase are located at $l = 1/3$ (Fig. 4.12 (g),(h)). This changes in the $\mathrm{IC_{HP_2}}$ phase at 8 GPa where the peaks split along the l-direction and appear at $l = 0.4$ and $l = 0.2$ (Fig. 4.12 (i)).

4.4.2 Elastic properties as a function of pressure

The transitions between the different incommensurate phases also effect the stiffness of the lattice. In Fig. 4.13 the unit cell volume as a function of pressure is shown at room temperature (a) and at 15 K (b). The relation between the volume of a solid and the pressure to which it is subjected is given by the so-called equation of state (EOS). A commonly used expression to model experimental data, in particular in earth science, is the 3rd-order Birch-Murnaghan EOS [81]:

$$p(V) = \frac{3K_0}{2}\left[\left(\frac{V_0}{V}\right)^{\frac{7}{3}} - \left(\frac{V_0}{V}\right)^{\frac{5}{3}}\right]\left\{1 + \frac{3}{4}(K_0' - 4)\left[\left(\frac{V_0}{V}\right)^{\frac{2}{3}} - 1\right]\right\}, \tag{4.16}$$

where $K_0 = -V\left(\frac{\mathrm{d}p}{dV}\right)$ represents the bulk modulus at $p = 0$ and K_0' is the first derivative of the bulk modulus at $p = 0$. The reference volume at $p = 0$ is given by V_0. Eq. 4.16 provides a smooth continuous relation between V and p. However, the data in Fig. 4.13 rather indic-

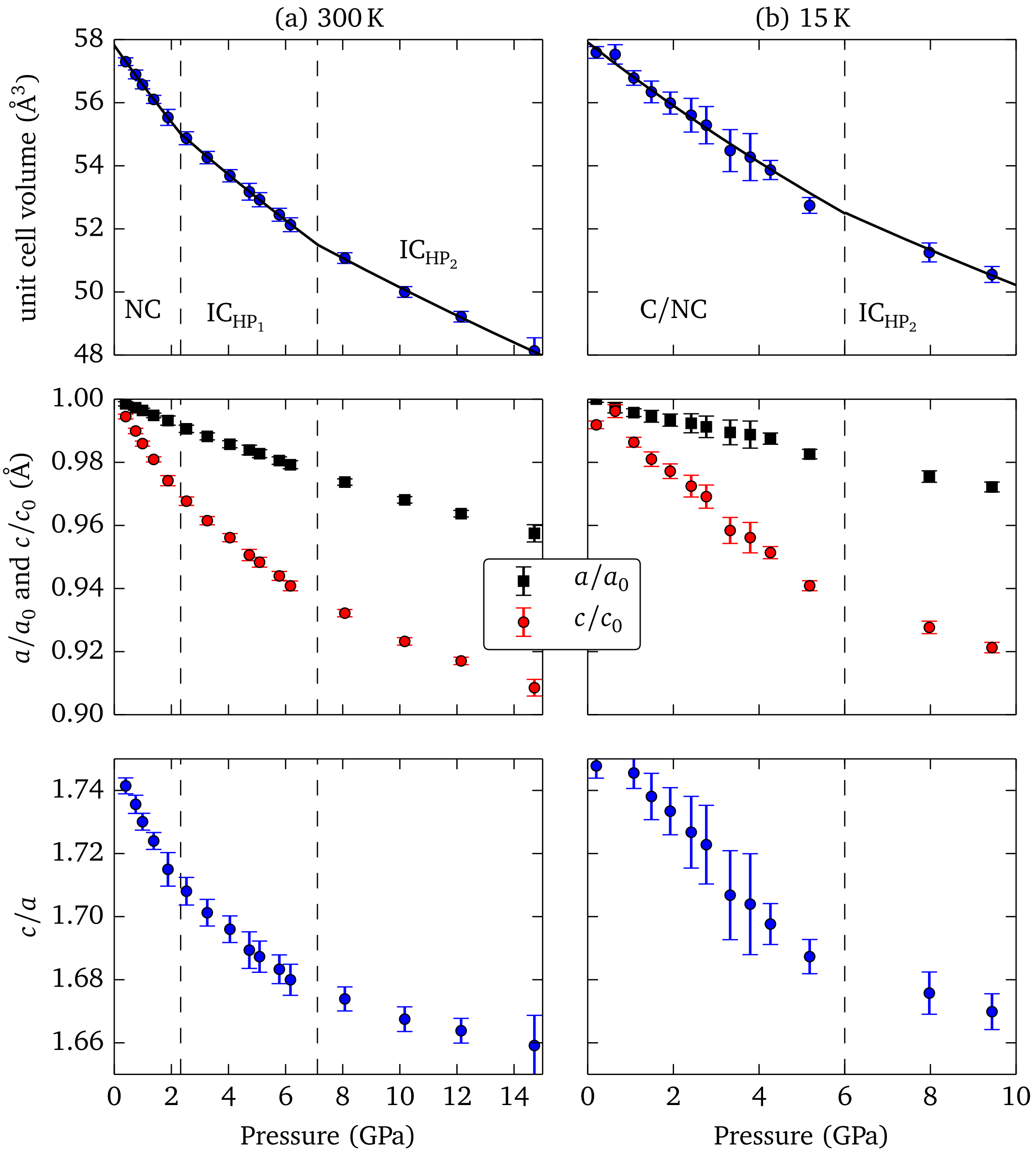

Figure 4.13: Pressure dependence of the lattice parameters at 300 K (a) and 15 K (b). The top panel shows the unit cell volume as a function of pressure for both temperatures. Solid lines are fits of a Birch-Murnaghan-EOS to the data. The relative change of the a and c-lattice parameter is shown in the middle panel. The ration between the c and a lattice parameter as a function of pressure is plotted in the bottom panel.

	300 K			15 K	
phase	NC	$\mathrm{IC}_{\mathrm{HP}_1}$	$\mathrm{IC}_{\mathrm{HP}_2}$	C/NC	$\mathrm{IC}_{\mathrm{HP}_2}$
K_0 (GPa)	45 ± 1	64 ± 1	93 ± 4	53 ± 1	76 ± 10
V_0 (Å^3)	57.81 ± 0.02	56.97 ± 0.03	55.3 ± 0.2	57.91 ± 0.07	56.6 ± 0.7
$K \parallel a$ (GPa)	272 ± 5	324 ± 4	408 ± 14	326 ± 11	377 ± 40
$K \parallel c$ (GPa)	72 ± 2	137 ± 3	276 ± 16	91 ± 3	189 ± 27

Table 4.1: Elastic properties for the different incommensurate phases. K_0 is the bulk modulus and V_0 the reference volume obtained by fitting a Birch-Murnaghan EOS to the data in Fig. 4.13 (a). $K \parallel a = -a_0 \left(\frac{\mathrm{d}p}{\mathrm{d}a}\right)$ and $K \parallel c = -c_0 \left(\frac{\mathrm{d}p}{\mathrm{d}c}\right)$ are the inverse linear compressibilities along the a and c axis, respectively, obtained by linear fits to the data in Fig. 4.13 (b).

ate that the slope $\left(\frac{\mathrm{d}V}{\mathrm{d}p}\right)$ changes discontinuously at the phase transitions between the incommensurate phases and is almost constant within those phases. Therefore, we fitted Eq. 4.16 piecewise to the data with a small fixed $K_0' = 2$, which turned out to describe the data better than a purely linear model function. The result of these fits is shown as black solid lines in Fig. 4.13 (a) and (b) and the fitted parameters are given in Tab. 4.1. The data may also be fitted with Eq. 4.16 over the whole pressure range yielding $K_0 = (39 \pm 1)$ GPa, $K_0' = 8.3 \pm 0.3$ and $V_0 = (57.88 \pm 0.03)$ Å^3 at 300 K as well as $K_0 = (42 \pm 3)$ GPa, $K_0' = 5 \pm 1$ and $V_0 = (58.02 \pm 0.09)$ Å^3 at 15 K. At the first glance such a fit also describes the data quite well and the fitted parameters are of the same magnitude as reported values for the isostructural compound $1T$-TiS$_2$ ($K_0 \approx 36$ GPa and $K_0' \approx 8$) [82]. However, a closer analysis reveals that the aforementioned piecewise model function obviously better accounts for the observed kinks in the pressure dependency of V. The quality of the two different fit models may also be quantified by evaluating the corresponding residuals. In Fig. 4.14 we plot histograms of the residuals related to the continuous Birch-Murnaghan model and the piecewise Birch-Murnaghan model. Fig. 4.14 (b) clearly reveals that the residuals of the piecewise model function obey a normal distribution whereas the distribution of the residuals of the continuous model function Fig. 4.14 (a) differ significantly from a normal distribution. It has been shown that the distribution of residuals is a good choice when it comes to the assessment and comparison of different (non-linear) fit models [83]. Therefore, it is valid to assume that our piecewise Birch-Murnaghan model function describes the data best. This implies that the phase transitions between the different incommensurate phases are accompanied by an abrupt change of the elastic parameters.

The pressure dependence of the lattice parameters a and c (Fig. 4.13 middle panel) further reveals that the c parameter is much more compressible than the a parameter. This becomes most obvious when looking at the ratio c/a of the lattice parameters as a function of pressure

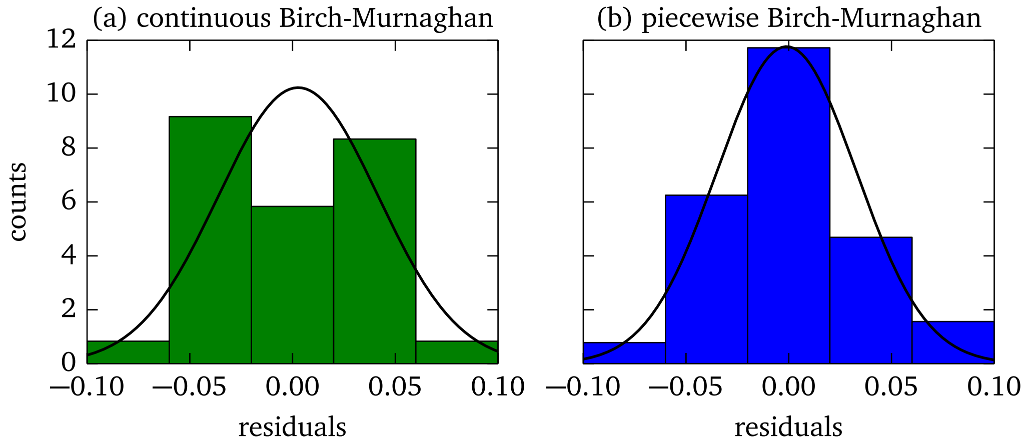

Figure 4.14: Comparison of the continuous (a) and piecewise (b) Birch-Murnaghan fit model based on the distribution of the corresponding residuals. Solid lines represent a fit of a Gaussian distribution to the histogram.

(Fig. 4.13 bottom panel). Moreover, the kinks observed at the phase transitions occur predominantly for the c parameter. We fitted a piecewise linear model to the data and present the obtained elastic constants in Tab. 4.1. At 300 K the inverse linear compressibility along the c axis changes roughly by a factor of two across the NC-IC$_{\mathrm{HP}_1}$ and IC$_{\mathrm{HP}_1}$-IC$_{\mathrm{HP}_2}$ transition. In contrast, this parameter changes only slightly for the a-direction.

4.4.3 Structural phase transitions of a defect lattice?

In section 4.3 it was pointed out that the splitting of the superlattice peaks of the NC-CDW is directly related to the defect lattice (discommensurations) which exists in this phase. The experimental fact that all incommensurate CDWs at room temperature are also characterized by a similar splitting (cf. Fig. 4.12) rises the obvious question whether these splittings stem from a defect lattice, too. However, the splittings are much smaller for the incommensurate CDWs compared to the nearly commensurate CDW which indicates that the involved period of the defect lattice is significantly larger. It is further hard to assign a nearby commensurate wave vector and, hence, a distinct order to the individual superlattice peaks. This constitutes a somewhat different characteristic as found for the nearly commensurate CDW.

Nonetheless, for the nearly commensurate CDW we showed that with increasing pressure the split superlattice peaks essentially move away from each other. We concluded that the defect lattice shrinks without changing its symmetry (cf. section 4.3). Since the arrangement of the superlattice peaks markedly changes for the various different incommensurate CDWs (cf. Fig. 4.12) it could be argued that the transitions between them are related to structural phase transitions of the defect lattice, where not only the scaling of the defect lattice changes but also its symmetry. As discussed above, the phase transitions at high pressure also effect the elastic properties of the crystal lattice. Yet these changes are rather subtle compared to structural phase transitions involving the crystal lattice, which further indicates that the observed phase transitions in $1T$-TaS$_2$ are indeed predominantly related to the defect lattice within the CDW order. Beyond that, Fig. 4.12 (b) shows that the superlattice peaks of the IC$_{\mathrm{HT}}$-CDW at elevated temperature and ambient pressure are not split. This could either mean that the defects completely disappear in this phase or that the defects no longer form a static well ordered lattice but become dynamic. In other words, the defect lattice melts with increasing temperature.

In section 2.4 it was outlined that in the framework of Ginzburg-Landau theory the defect lattice of discommensurations represents a lattice of solitons which appears due to the interaction between CDW and the crystal lattice. Most importantly, these solitons have particle-like properties which means that they are localized and their shape is maintained as a function of time. In addition, each discommensuration is associated with an electric charge which gives rise to (repulsive) interactions between individual solitons. In this regard the defect lattices in CDWs pose intriguing analogies to skyrmions. These are topological solitons in magnetic systems which also tend to form ordered lattices [18].

Unfortunately, we cannot directly confirm the existence of structural phase transitions of a defect lattice in $1T$-TaS$_2$ at this point. In order to do so it would be necessary to refine the structure of the high-pressure incommensurate phases as it has been done for the nearly commensurate phase [55]. This is a non-trivial and highly demanding task since it requires the collection of high-resolution datasets covering large regions in reciprocal space. By now the accessible portion of reciprocal space is rather limited due to the experimental setup and the pressure cell. Furthermore, it would be very interesting to survey the phase boundaries between the different incommensurate phases. In Fig. 4.12 (a) these phase boundaries are indicated by dotted lines and labeled with question marks since for now these lines should be considered as conceptional due to the lack of data.

Apparently, the notion of self-organized soliton lattices with particle-like properties undergoing structural phase transitions is very interesting and deserves closer investigation in future work.

4.5 Stacking disorder of CDW layers in the C-CDW phase

In this section we will discuss the stacking of the TaS$_2$ layers along the c direction within the different CDW phases of $1T$-TaS$_2$. The XRD results presented in section 4.3 concerned primarily the CDW structure within the ab-plane and its pressure dependence. In order to study the stacking of the CDW layers along the c direction it is necessary to investigate the XRD intensity distribution of the superlattice peaks as a function of l.

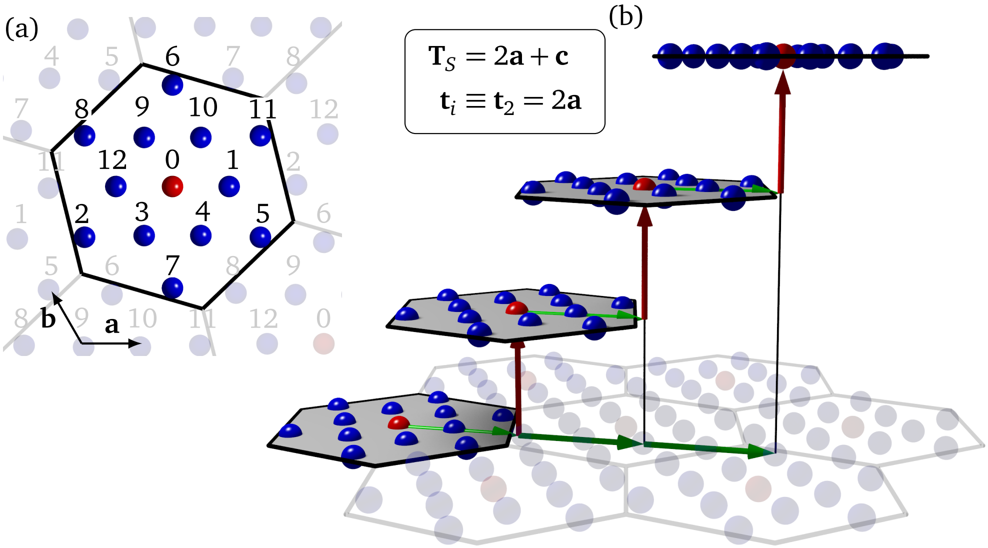

Figure 4.15: Possible CDW layer stackings. The Ta-sites within the $\sqrt{13} \times \sqrt{13}$ supercell are labeled according to the numbers in (a). The vector $\mathbf{t}_i$ points from Ta-site 0 to Ta-site i. A certain layer is in configuration m when it is shifted by $\mathbf{t}_m$ with respect to some reference layer. A periodic stacking with $\mathbf{t}_i = \mathbf{t}_2$ is shown in (b).

The stacking of CDW layers in TMDs and in particular 1*T*-TaS$_2$ has been extensively investigated in terms of Ginzburg-Landau theory [84, 85] and experimentally by means of XRD [86, 87]. Below, we will revisit and extent the analysis presented in references 85 and 87 in order to characterize the CDW layer stacking in more detail.

As explained in chapter 3.2 the in-plane lattice modulation of the C-CDW phase results in the formation of an in-plane $\sqrt{13} \times \sqrt{13}$ supercell containing 13 Tantalum and 26 Sulfur sites. Apparently, there are 13 possibilities for the orientation of two adjacent layers according to the 13 Ta-sites in the supercell. Therefore it is possible to characterize the stacking of CDW layers in terms of the stacking vector $\mathbf{T}_S$ which connects the central Ta-sites in successive layers.

It is also useful to define a shift vector $\mathbf{t}_i, i = 0, \ldots, 12$ which is the projection of $\mathbf{T}_S$ onto the ab-plane for the 13 possibilities i. The labeling i starts with 0 at the central Ta-site and increases towards the a-direction obeying periodic boundary conditions. This situation is illustrated in Fig. 4.15 (a), where the Ta-sites within the $\sqrt{13} \times \sqrt{13}$ supercell are shown along with the labels i. A particular layer is in configuration i with respect to some reference layer when it is shifted by $\mathbf{t}_i$ against the reference layer. In other words a shift by $\mathbf{t}_i$ transforms a layer in configuration n into a layer in configuration $(n+i) \mod 13$. In that way it is possible to describe a particular stacking of N CDW layers with a sequence of N numbers $(i_1 i_2 \ldots i_N)$ denoting the configuration of each layer. Alternatively, it is possible to use $N-1$ shift vectors

$(\mathbf{t}_i^{(1)}\mathbf{t}_i^{(2)}\ldots\mathbf{t}_i^{(N-1)})$ with $\mathbf{t}_i^{(l)} = \mathbf{t}_{i_{(l+1)}-i_l}$. For instance, the stacking of the 4 CDW layers shown in Fig. 4.15 (b) is given by (0246) or $(\mathbf{t}_2\mathbf{t}_2\mathbf{t}_2)$. In order to describe infinite periodic stackings we use the symbol $\left\langle \mathbf{t}_i^{(1)}\ldots\mathbf{t}_i^{(M)} \right\rangle$ where the block of M shift vectors defines the repeating unit[3]. In that notation the infinite continuation of the stacking shown in Fig. 4.15 (b) would be expressed as $\langle \mathbf{t}_2 \rangle$. It is easy to show that for the simple periodic stackings $\langle \mathbf{t}_i \rangle$ the XRD intensity $I(\mathbf{Q})$ has sharp peaks at

$$\mathbf{Q} = \mathbf{q}_j^{||} + (k_j + l)\mathbf{c}^*,\ l \in \mathbb{Z}, \tag{4.17}$$

where $\mathbf{q}_j^{||}$ is an in-plane modulation wave vector and k_j is given by $k_j = \mathbf{q}_j^{||}\mathbf{t}_i/2\pi$.

4.5.1 Disordered CDW layer stacking

Walker and Withers [84] and later Nakanishi *et al.* [85] studied the stacking of CDW layers in $1T$-TMDs in terms of Ginzburg-Landau theory. For the case of only nearest neighbor interlayer coupling they found that the stackings $\langle \mathbf{t}_i \rangle$ $i = 2, 5, 6$ are degenerated among each other. The same is also true for the groups with $i = 7, 8, 11$; $i = 4, 10, 12$; $i = 1, 3, 8$ and $i = 0$. This is plausible since these vectors are equivalent by the threefold symmetry of the in-plane $\sqrt{13} \times \sqrt{13}$ supercell. When a group of stackings is degenerated one may expect that the corresponding shift vectors occur randomly and the resulting stacking sequence is not periodical but partially[4] disordered. In order to describe such disordered stackings we introduce the following notation: $\left\langle \mathbf{t}_{\{256\}} \right\rangle$ which denotes an infinite stacking where the shift vector $\mathbf{t}$ is chosen randomly from the group $\mathbf{t}_2, \mathbf{t}_5$ and $\mathbf{t}_6$. Such a stacking sequence is visualized in Fig. 4.17 (d). Nakanishi *et al.* [85] further considered interlayer coupling up to next nearest neighbor layers and found stackings of the form $\left\langle \mathbf{t}_0\mathbf{t}_{\{256\}} \right\rangle$ to be stable. $\left\langle \mathbf{t}_0\mathbf{t}_{\{256\}} \right\rangle$ stands for an alternation of the shift vector $\mathbf{t}_0$ and a vector chosen randomly from the group $\mathbf{t}_2, \mathbf{t}_5$ and $\mathbf{t}_6$, which is again a partially disordered stacking. Fig. 4.17 (c) illustrates this kind of alternating stacking.

In order to reveal which type of stacking occurs in the real material it is necessary to compare the theoretical structure factor of different stackings with XRD data. In Fig. 4.16 we show the XRD intensity of the first order superlattice peak measured along the l-direction at 100 K in the C-CDW phase and at 230 K in the NC-CDW phase. In the C-CDW phase at 100 K the two broad peaks indicate that the stacking order of the CDW-layers is indeed disordered. At 230 K the diffraction pattern changes markedly and only a single sharp peak implies that the NC-CDW phase is characterized by a long-range ordered CDW-layer stacking. Below we will calculate structure factors for different disordered stackings and compare them with the XRD data taken at 100 K in order to shed light on the CDW-layer stacking order of the C-CDW phase.

---

[3] Note that the notation chosen in this thesis is slightly different from the one used in reference 85.

[4] The stacking is not completely disordered because the stacking vector is chosen from a subset of all possible stacking vectors.

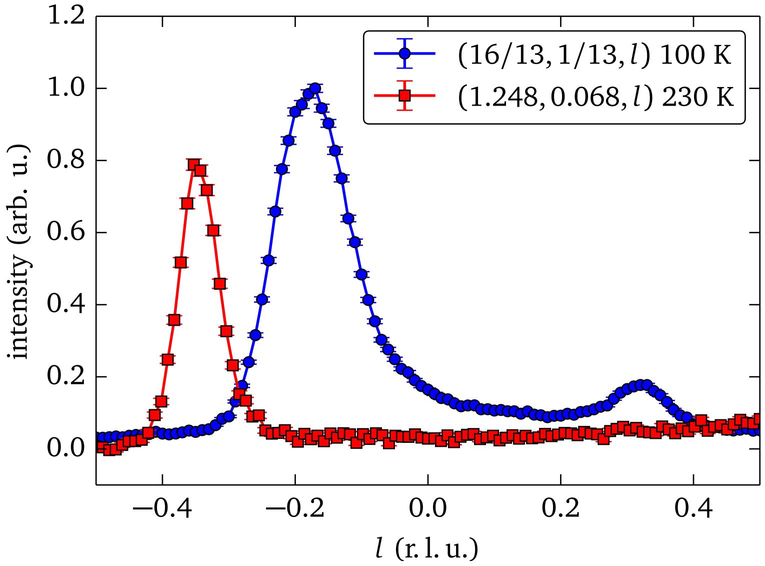

Figure 4.16: XRD intensity of the first order superlattice peak across the C-CDW to NC-CDW transition. The single peak observed for the NC-CDW phase implies a well-ordered stacking along c. Upon entering the C-CDW phase the XRD diffraction pattern changes markedly and two broad peaks appear due to the presence of disordered stacking along c.

Following reference 85 the XRD intensity for partially disordered stackings may be calculated from:

$$I(\mathbf{Q} = \mathbf{q}_k^{\|} + l\mathbf{c}^*) \propto \sum_{n,n'} G_{nn'}(l) e^{-i\mathbf{q}_k^{\|}(\mathbf{t}_n - \mathbf{t}_{n'})}, \tag{4.18}$$

where

$$G_{nn'}(l) \propto \sum_{m,m'} P_{nn'}(m' - m) e^{i2\pi l(m'-m)}. \tag{4.19}$$

$P_{nn'}(m' - m)$ describes the conditional probability to find the m'-th layer in configuration n' when the m-th layer is in configuration n. Nakanishi *et al.* showed that for the case of the stacking $\left\langle \mathbf{t}_0 \mathbf{t}_{\{256\}} \right\rangle$ $G_{nn'}(l)$ may be expressed as:

$$G_{nn'} \propto (1 + \cos(2\pi l))\{[1 - \hat{R}e^{i4\pi l}]^{-1}_{nn'} + \text{h.c.} - \delta_{nn'}\}, \tag{4.20}$$

and for $\left\langle \mathbf{t}_{\{256\}} \right\rangle$:

$$G_{nn'} \propto \{[1 - \hat{R}e^{i2\pi l}]^{-1}_{nn'} + \text{h.c.} - \delta_{nn'}\}, \tag{4.21}$$

where $\hat{R}$ is a 13 × 13 matrix with:

$$\hat{R}_{nn'} = \begin{cases} \frac{1}{13} & \text{if } (n'-n) \mod 13 = 2, 5, 6 \\ 0 & \text{otherwise.} \end{cases} \tag{4.22}$$

From Eqs. 4.18, 4.20 and 4.21 it is possible to calculate $I(l)$ for the superlattice peaks. In Fig. 4.17 we reproduce these results for $\left\langle \mathbf{t}_0\mathbf{t}_{\{256\}} \right\rangle$ and $\left\langle \mathbf{t}_{\{256\}} \right\rangle$ and compare them to XRD data taken in the C-CDW phase. Apparently, the alternating stacking $\left\langle \mathbf{t}_0\mathbf{t}_{\{256\}} \right\rangle$ describes the double peak structure observed in XRD correctly. However, the calculated peaks are systematically sharper and also slightly shifted in position. Also, the intensity ratio is somewhat different from the observed one. The non-alternating stacking $\left\langle \mathbf{t}_{\{256\}} \right\rangle$ clearly fails to reproduce the double peak structure and peak positions. As demonstrated in reference 85 the $\left\langle \mathbf{t}_0\mathbf{t}_{\{256\}} \right\rangle$ stacking is the only stacking capable to reproduce the critical features of the XRD data showing that this stacking is indeed relevant for the case of $1T$-TaS$_2$. In the following section we will extend the model of the $\left\langle \mathbf{t}_0\mathbf{t}_{\{256\}} \right\rangle$ stacking by introducing a finite correlation length ξ.

4.5.2 Numerical simulation of XRD structure factors for disordered stackings

Instead of dealing with the conditional probability $P_{nn'}(m'-m)$ in Eq. 4.19 we choose a numerical approach for the simulation of the structure factors. Therefore, we calculate the structure factor of many ($\approx 10^6$) finite stacking sequences and sum them incoherently to obtain the simulated XRD intensity. The stacking sequences are generated randomly according to the particular stacking model. Thus, this algorithm may be interpreted as a Monte Carlo simulation. In detail, this procedure reads as follows:

The structure factor of a stacking sequence of M layers $(i_1 i_2 \dots i_M)$ may be calculated from:

$$S(l) \equiv S(\mathbf{Q} = \mathbf{q}_k^{\|} + l\mathbf{c}^*) \propto \sum_{m=1}^{M} \exp(i2\pi ml + i\mathbf{q}_k^{\|}\mathbf{t}_{i_m}). \tag{4.23}$$

In order to obtain the XRD intensity as a function of l we calculated Eq. 4.23 for N different stacking sequences resulting in N structure factors $S_i(l)$. The XRD intensity is finally given by the incoherent sum:

$$I(l) \propto \sum_{i=1}^{N} S_i(l) S_i^*(l). \tag{4.24}$$

The problem hence reduces to the generation of the stacking sequences. To this end we implemented the following algorithm for the $\left\langle \mathbf{t}_0\mathbf{t}_{\{256\}} \right\rangle$ stacking with finite correlation length,

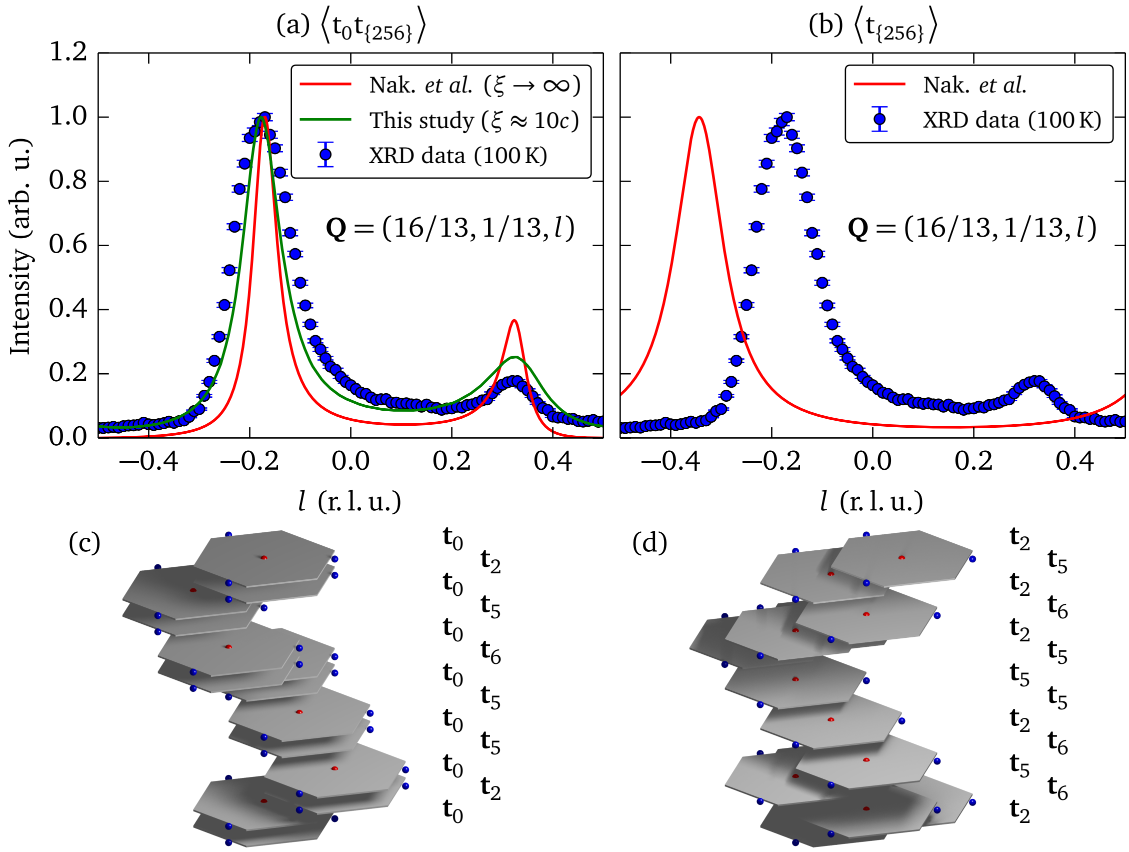

Figure 4.17: Comparison of simulated structure factors for the stackings $\langle \mathbf{t}_0\mathbf{t}_{\{256\}}\rangle$ (a) and $\langle \mathbf{t}_{\{256\}}\rangle$ (b) with XRD data taken at 100 K in the C-CDW phase. The red lines reproduce results from reference 85. The green line shows the result obtained in this study for a finite correlation length of $\xi \approx 10$ layers. A visualization of the two stackings is given in (c) and (d).

which we denote as $\langle \mathbf{t}_0\mathbf{t}_{\{256\}}\rangle_f$: The first and second layer are set to an arbitrary configuration i. Then a loop, in which for every iteration n a random number α between 0 and 1 is generated, starts. If α is lower than the stacking fault parameter f the algorithm checks if layers $n-1$ and $n-2$ are in the same configuration. When this is the case the configuration of layer n is set to $(i_{n-1}+a) \mod 13$, where a is chosen randomly from the set $\{2,5,6\}$. If layer $n-1$ and $n-2$ are not in the same configuration, layer n is set to i_{n-1}. When α is greater than f the configuration of layer n is set to $(i_{n-1}+a) \mod 13$ where a is chosen randomly from the set $\{0,2,5,6\}$. As n exceeds a certain number the loop aborts and returns the stacking sequence $(i_1 i_2 \ldots i_M)$. This procedure is also illustrated as pseudo-code in Fig. 4.18.

This algorithm may be readily adapted to other stacking types as for example a non-alternating stacking $\langle \mathbf{t}_{\{0256\}}\rangle_f$. In Fig. 4.19 we show results obtained by our numerical simulations

```
$f$ := stacking fault probability ;
$S$ := stacking sequence ;
$S[1] = S[2]$ = random choice from $0 \dots 12$ ;
for $l$ in $3 \dots M$ do
    $\alpha$ = random number in $(0, 1]$;
    if $\alpha < f$ then
        if $S[l-1] - S[l-2] = 0$ then
            $S[l] = (S[l-1] +$ random choice from $2, 5, 6)$ mod 13 ;
        else
            $S[l] = S[l-1]$
        end
    else
        $S[l] = (S[l-1] +$ random choice from $0, 2, 5, 6)$ mod 13 ;
    end
end
return $S$ ;
```

Figure 4.18: Pseudo-code of an algorithm for the generation of stacking sequences according to the $\left\langle \mathbf{t}_0 \mathbf{t}_{\{256\}} \right\rangle$ stacking with finite coherence length.

for the alternating stacking $\left\langle \mathbf{t}_0 \mathbf{t}_{\{256\}} \right\rangle_f$ and, solely for demonstration, for the non-alternating stacking $\left\langle \mathbf{t}_{\{0256\}} \right\rangle_f$ as a function of the stacking fault probability parameter f. In the case of $\left\langle \mathbf{t}_{\{0256\}} \right\rangle_f$ the parameter f denotes the probability that a random shift vector from the set $\{\mathbf{t}_0, \mathbf{t}_2, \mathbf{t}_5, \mathbf{t}_6\}$ occurs. Otherwise the shift vector is the same as for the precedent layers. This means that for $f \to 0$ the simulation yields macroscopic domains governed by the periodic stackings $\langle \mathbf{t}_0 \rangle, \langle \mathbf{t}_2 \rangle, \langle \mathbf{t}_5 \rangle$ and $\langle \mathbf{t}_6 \rangle$ resulting in sharp peaks at positions consistent with the condition in Eq. 4.17. As f increases the peaks smear out and finally for $f = 1$ a single broad peak at $l \approx -0.28$ remains.

For the $\left\langle \mathbf{t}_0 \mathbf{t}_{\{256\}} \right\rangle_f$ stacking f describes the probability that the $\left\langle \mathbf{t}_0 \mathbf{t}_{\{256\}} \right\rangle$ stacking is interrupted by a random shift vector from the set $\{\mathbf{t}_0, \mathbf{t}_2, \mathbf{t}_5, \mathbf{t}_6\}$. Therefore, the simulation for $f = 0$ should give the same result as obtained for the $\left\langle \mathbf{t}_0 \mathbf{t}_{\{256\}} \right\rangle$ stacking via Eq. 4.18. This is indeed the case as can be observed in Fig. 4.19 (upper line) where we compare the result of both approaches. With increasing f the peaks become broader and shift in position. In addition the peak at $l \approx 1/3$ loses intensity and vanishes for $f \to 1$. It is worth noting that for $f = 1$ both stackings are equal $\left\langle \mathbf{t}_0 \mathbf{t}_{\{256\}} \right\rangle_{f=1} = \left\langle \mathbf{t}_{\{0256\}} \right\rangle_{f=1}$. An interesting result of this numerical analysis is that for partially disordered structures the coherence length, the observed modulation wave vector (peak position) and the intensity distribution are coupled as can be clearly seen in Fig. 4.19. In contrast, for ordinary structures a decreasing coherence length solely causes a broadening but not a shifting of the related peaks.

In comparison with the XRD data shown in Fig. 4.17 it turns out that the simulated XRD for the $\left\langle \mathbf{t}_0 \mathbf{t}_{\{256\}} \right\rangle_f$ stacking with $f = 0.27$ fits very well to the data. The corresponding correlation length ξ is given by:

$$\xi = \sum_{n=1}^{\infty} n \cdot (1-f)^n = \frac{1-f}{f^2} \tag{4.25}$$

and results in $\xi \approx 10$ layers for $f = 0.27$. In Fig. 4.17 on page 52 the simulated XRD intensity for $\xi = 10$ layers is shown along with the experimental data. The very good agreement of the presented simulations with the experimentally observed XRD verifies that the stacking of the CDW layers in the C-CDW phase of $1T$-TaS$_2$ is well described by the $\left\langle \mathbf{t}_0 \mathbf{t}_{\{256\}} \right\rangle_f$ stacking model. We will come back to the CDW layer stacking and its impact on the electronic structure in chapter 5.4.

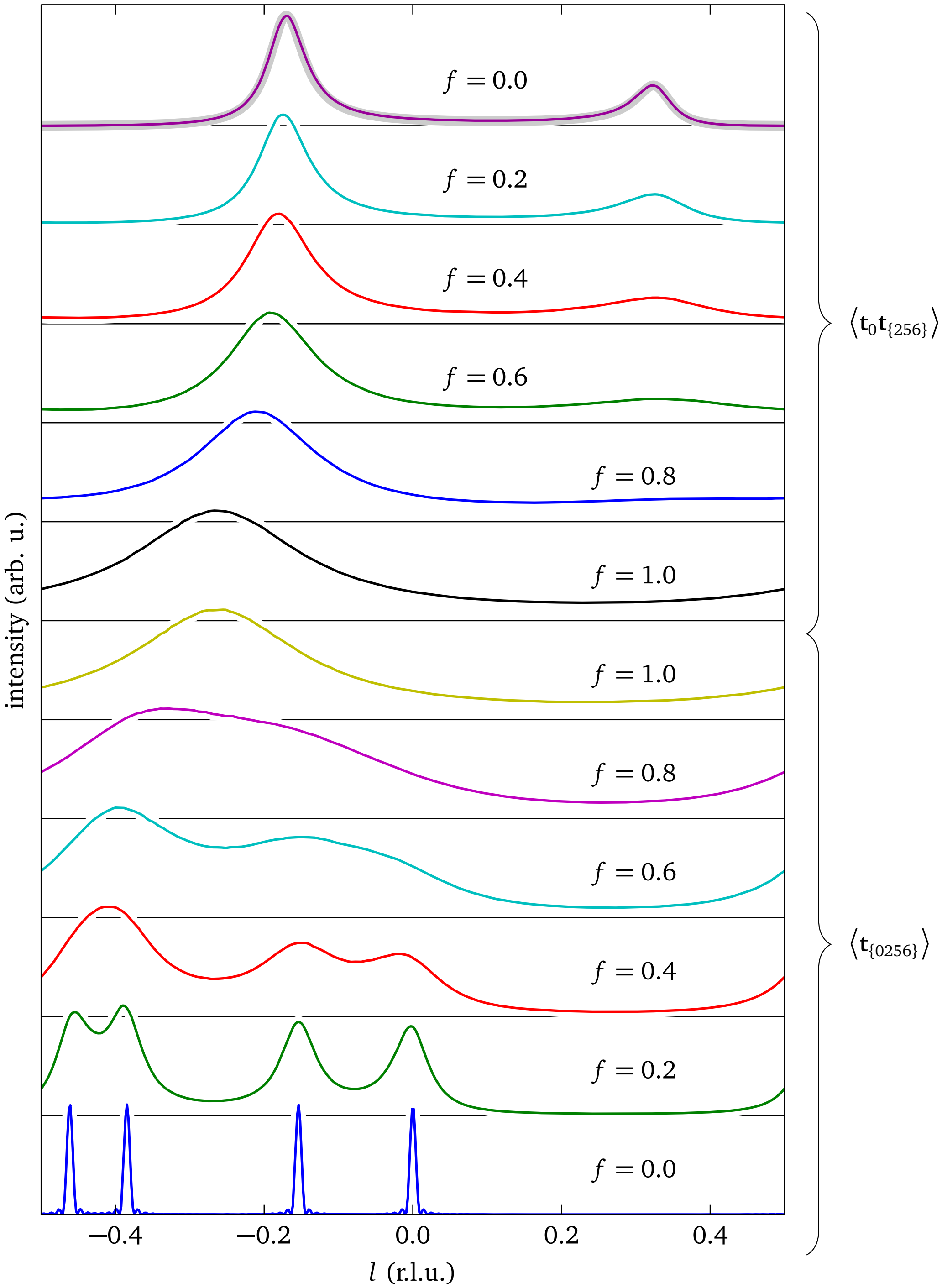

Figure 4.19: Simulated XRD intensity for the alternating stacking $\langle \mathbf{t}_0\mathbf{t}_{\{256\}} \rangle$ (top) and a non-alternating stacking $\langle \mathbf{t}_{\{0256\}} \rangle$ for different stacking fault probabilities f. For $\langle \mathbf{t}_0\mathbf{t}_{\{256\}} \rangle$ and $f = 0$ the result of Eq. 4.18 is shown (thick gray line) along with our simulation to show the equivalence of booth approaches.

5 Electronic band structure of charge density wave phases in $1T$-TaS$_2$

This chapter deals with the electronic structure of the charge density wave phases in $1T$-TaS$_2$ studied experimentally and theoretically in terms of high-resolution angle-resolved photoemission spectroscopy and state-of-the-art density functional theory calculations.

In this study we reveal a remarkable and surprising feature of charge density waves, namely their intimate relation to orbital order. For the prototypical material $1T$-TaS$_2$ we not only show that the charge density wave within the two-dimensional TaS$_2$-layers involves previously unidentified orbital textures of great complexity. We also demonstrate that two metastable stackings of the orbitally ordered layers allow to manipulate salient features of the electronic structure. Indeed, these orbital effects provide a route to switch the properties of $1T$-TaS$_2$ nanostructures from metallic to semiconducting with technologically pertinent gaps of the order of 200 meV. This new type of orbitronics is especially relevant for the ongoing development of novel, miniaturized and ultrafast devices based on layered transition metal dichalcogenides [13–17].

The chapter is organized as follows: Sections 5.1, 5.2 and 5.3 introduce the theoretical and experimental methods. The key results of this chapter are presented and discussed in section 5.4 which is a extended version of the journal article [T. Ritschel *et al.*, Nat Phys **11**, 328-331 (2015)]. In section 5.5 we relate our results to tight-binding approaches and demonstrate their limitations. An improved density functional theory model is presented and related to the angle-resolved photoemission data in section 5.6. Finally, in section 5.7 we link our results for $1T$-TaS$_2$ to other isostructural transition metal dichalcogenides.

5.1 Density functional theory[1]

In this section we briefly review some basics of density functional theory (DFT). For deeper insights the reader is relegated to the original publication of W. Kohn and L. J. Sham [88] and the various text books (e. g. reference 89).

---

[1] The line of argument in this section is influenced by the lecture *"Vielteilchentheorie kondensierter Materie"* given by Prof. Timm at the TU-Dresden in 2014

The electronic structure of a crystal could – in principle – be calculated by solving a N-particle Schrödinger equation for the electrons in the crystal[2]:

$$\begin{aligned}\hat{H}\Psi(\mathbf{r}_1,\mathbf{r}_2,\ldots,\mathbf{r}_N) &= \left[\hat{T}+\hat{V}_{eI}+\hat{V}_{ee}\right]\Psi(\mathbf{r}_1,\mathbf{r}_2,\ldots,\mathbf{r}_N)\\ &= \left[\sum_i \frac{1}{2m}\nabla_i^2+\sum_i V(\mathbf{r}_i)+\sum_{ij,i\neq j}\frac{e^2}{4\pi\varepsilon_0}\frac{1}{|\mathbf{r}_i-\mathbf{r}_j|}\right]\Psi(\mathbf{r}_1,\mathbf{r}_2,\ldots,\mathbf{r}_N)\\ &= E\Psi(\mathbf{r}_1,\mathbf{r}_2,\ldots,\mathbf{r}_N), \qquad (5.1)\end{aligned}$$

where N constitutes the number of electrons and $\Psi(\mathbf{r}_1,\mathbf{r}_2,\ldots,\mathbf{r}_N)$ is the many-body wave function of the electrons. $\hat{T}$ is the kinetic energy, $\hat{V}_{eI}$ the single particle potential due to the interaction of the electrons with the nuclei and $\hat{V}_{ee}$ the two particle potential which describes the electron-electron interaction. In Eq. 5.1 we use the Born-Oppenheimer approximation which assumes that the motion of the electrons is much faster than that of the nuclei. Hence, the electrons move in a static potential represented by $\hat{V}_{eI}$. The solution of Eq. 5.1 would contain all information about the electronic system.

However, since $N \approx 10^{23}$ such a “brute force” approach is in general impossible to solve. In fact, it would not even be possible to save the solution of the N-particle Schrödinger equation because there is not enough memory. Therefore, these many body problems cannot be solved exactly, apart from some few exceptions.

In order to tackle this problem approximations have to be employed. One popular approximation is to treat the interaction between the electrons as a perturbation. The key quantity of the resulting perturbation theories is the so-called electronic Green’s function which is often given by infinite sums. In some cases it is possible to sum infinite many – but not all – terms in this sum yielding so-called Dyson series which result in an approximation for the electronic Green’s function. These theories have the advantage that they are, in principle, exact if one could sum all terms in the Green’s function. A famous perturbation theory is for instance the random phase approximation (RPA).

Mean field theories constitute another class of approximations in which the interacting many-electron system is mapped (approximately) onto a noninteracting system. The noninteracting reference systems are, in general, readily solvable. Common examples of mean field theories are the Hartree-Fock or BCS-theory.

The DFT tries to combine the advantages of the above approaches by a mapping of the interacting many-electron system onto a noninteracting system which – in principle – is exact. The key quantity DFT deals with is not the many-electron wave function but the electron

---

[2] The Schrödinger equation represents a non-relativistic theory. In cases where relativistic effects become important appropriate theories have to be taken into account.

density:

$$n(\mathbf{r}) = N \int \mathrm{d}^3\mathbf{r}_2 \mathrm{d}^3\mathbf{r}_3 \ldots \mathrm{d}^3\mathbf{r}_N \, |\Psi(\mathbf{r}, \mathbf{r}_2, \mathbf{r}_3, \ldots \mathbf{r}_N)|^2 \, . \tag{5.2}$$

The electron density $n(\mathbf{r})$ is a much simpler quantity than the many-electron wave function $\Psi(\mathbf{r}, \mathbf{r}_2, \mathbf{r}_3, \ldots \mathbf{r}_N)$ since it only depends on one position $\mathbf{r}$ instead of $N \approx 10^{23}$ positions. Kohn and Sham showed that all properties of the electronic system are uniquely determined by the ground-state electron density $n_{GS}(\mathbf{r})$ which yields the central idea of DFT to consider $n_{GS}(\mathbf{r})$ as the fundamental quantity.

5.1.1 The Hohenberg-Kohn theorems

It is important to note that $\hat{T}$ and $\hat{V}_{ee}$ in Eq. 5.1 are universal, which means that they are the same for all systems. The only term which depends on the particular system is the potential $V(\mathbf{r})$. This implies that every potential $V(\mathbf{r})$ (and electron number N) uniquely determines a ground state wave function $\Psi_{GS}(\mathbf{r}_1, \mathbf{r}_2, \ldots, \mathbf{r}_N)$ and hence an ground state electron density $n_{GS}(\mathbf{r})$.

The first Hohenberg-Kohn theorem [90] states that this mapping is bijective, which means that also every ground state electron density $n_{GS}(\mathbf{r})$ uniquely determines the potential $V(\mathbf{r})$. In other words, the unique mappings

$$n_{GS}(\mathbf{r}) \rightarrow V(\mathbf{r}) \rightarrow \Psi_{GS}(\mathbf{r}_1, \mathbf{r}_2, \ldots, \mathbf{r}_N) \rightarrow n_{GS}(\mathbf{r}) \tag{5.3}$$

exist. The second Hohenberg-Kohn theorem [90] states that for a fixed Hamiltonian, i. e. fixed $V(\mathbf{r})$ and N, the ground state electron density $n_{GS}(\mathbf{r})$ minimizes the energy functional:

$$E[n] = \left\langle \Psi[n] | \hat{H} | \Psi[n] \right\rangle . \tag{5.4}$$

$E[n]$ is indeed a unique functional of $n(\mathbf{r})$ due to the first Hohenberg-Kohn theorem. Accordingly, the ground state properties and in particular the ground state electron density $n_{GS}(\mathbf{r})$ of the interacting electron system may be found by minimizing $E[n]$ with respect to n.

5.1.2 The Kohn-Sham equations

In 1965 Kohn and Sham developed a method to practically solve the minimization problem posed by Eq. 5.4 [88]. The key idea is to map the interacting electron system onto a noninteracting electron system with the same ground-state electron density. This is always possible because the first Hohenberg-Kohn theorem applies for arbitrary fixed interactions $\hat{V}_{ee}$, in particular, hence, for the noninteracting case $\hat{V}_{ee} = 0$. Accordingly, for every ground-state electron density of an interacting electron system it is possible to find an effective potential $V_{\mathrm{eff}}(\mathbf{r})$ of a noninteracting electron system so that the ground-state electron densities of the interacting and the noninteracting system coincide.

For a noninteracting system, however, the ground-state is given by a Slater determinant of the N single particle eigenfunctions with the lowest energies. These eigenfunctions have to obey the so-called Kohn-Sham equations:

$$\left[-\frac{1}{2m}\nabla^2 + V_{\text{eff}}(\mathbf{r})\right]\phi_i(\mathbf{r}) = \epsilon_i\phi_i(\mathbf{r}). \tag{5.5}$$

Eq. 5.5 is merely a single particle Schrödinger equation for the Kohn-Sham orbitals $\phi_i(\mathbf{r})$ and an effective potential $V_{\text{eff}}(\mathbf{r})$. The effective potential may be written as:

$$V_{\text{eff}}[n](\mathbf{r}) = V(\mathbf{r}) + \frac{1}{2}\int \mathrm{d}^3\mathbf{r}\frac{e^2}{4\pi\varepsilon_0}\frac{n(\mathbf{r})}{|\mathbf{r}-\mathbf{r}'|} + V_{xc}[n](\mathbf{r}). \tag{5.6}$$

The first term is the potential given by the interaction of the electrons with the nuclei and depends on the particular system. The second term constitutes the mean-field Coulomb interaction between one electron and a charge density $-eN(\mathbf{r})$ given by all other electrons and is called the Hartree potential. $V_{xc}[n](\mathbf{r})$ finally is the so-called exchange-correlation potential and effectively contains all the many-body interactions. When the Kohn-Sham orbitals $\phi_i(\mathbf{r})$ are sorted with increasing corresponding energy ϵ_i the electron density of the noninteracting reference system is simply given by:

$$n(\mathbf{r}) = \sum_{i=1}^{N}|\phi_i(\mathbf{r})|^2. \tag{5.7}$$

The particular form of $V_{\text{eff}}[n](\mathbf{r})$ (Eq. 5.6) ensures that this electron density of the noninteracting reference system is the same as the ground state electron density of the interacting electron system with the potential $V(\mathbf{r})$. Thus the interacting many-electron problem has been reduced to the solution of the Kohn-Sham equations, which is an effective single particle problem. Since the Hartree potential and the exchange-correlation potential parametrically depend on $n(\mathbf{r})$ it is necessary to solve Eq. 5.5 self-consistently in an iterative process. Therefore, one starts with a guess for $n(\mathbf{r})$ and solves Eq. 5.5. The resulting Kohn-Sham orbitals ϕ_i yield a new electron density $n(\mathbf{r})$. This process is then iterated until a certain convergence criteria is met.

The result would indeed give the exact ground state electron density $n_{GS}(\mathbf{r})$ and ground state energy $E[n_{GS}]$ of the interacting electron system. But this would only be possible if the exchange-correlation potential $V_{xc}[n](\mathbf{r})$ would be known exactly. Unfortunately, this is not the case and one has to rely on approximations for $V_{xc}[n](\mathbf{r})$ which will be discussed briefly below. In this respect the exchange-correlation potential resembles the role of the self-energy in Green's functions perturbation theory which effectively absorbs the many-body effects.

For periodic crystalline systems the Kohn-Sham orbitals may be labeled by a wave vector $\mathbf{k}$ and the band index i. The usual DFT band structures show the Kohn-Sham energies $\epsilon_i(\mathbf{k})$ as a function of $\mathbf{k}$. At this point it is worth noting that the Kohn-Sham orbitals and Kohn-Sham energies are auxiliary quantities and in general do not correspond to quasi-particle peaks in the spectral function $A(\omega,\mathbf{k})$, which is the physical quantity accessible by means of angle-resolved photoemission spectroscopy (see section 5.2). One also has to admit that this type of DFT is purely a theory of the ground state. This has to be kept in mind when DFT results are compared to experiments. However, in the limit of small interactions the Kohn-Sham energies often provide a good approximation for the single particle energies.

5.1.3 Local density approximation

As explained above the DFT is – in principle – an exact theory given that the exact form of the exchange-correlation potential V_{xc} would be known. Since this is not the case one has to employ approximations for V_{xc}. In solid state applications the local density approximation (LDA) is the most widely used approximation for the exchange-correlation potential. The LDA exploits that the exchange-correlation potential for the interacting *homogeneous* electron gas is – at least numerically – well known. The exchange-correlation energy per particle of the homogeneous electron gas with the constant electron density n may be written as:

$$e_{xc}(n) \equiv \frac{E_{xc}}{N} = e_x(n) + e_c(n), \tag{5.8}$$

where $e_x(n)$ is the exchange part of the energy and $e_c(n)$ is the correlation part. For $e_x(n)$ an analytical expression is known:

$$e_x(n) = -0.916 \cdot \mathrm{Ry}\left(\frac{4\pi}{3}\right)^{1/3} n^{1/3} a_0, \tag{5.9}$$

where Ry is the Rydberg unit of energy and a_0 is the Bohr radius. For the correlation energy $e_c(n)$ no analytical expression exists, but Monte Carlo simulations provide very accurate numerical values for $e_c(n)$ [91].

The key idea of LDA is to use Eq. 5.8 – which is exact for homogeneous electron densities – for non-homogeneous electron densities. Therefore, the exchange-correlation energy in LDA is written as:

$$E_{xc}^{LDA}[n(\mathbf{r})] = \int \mathrm{d}^3\mathbf{r}\, n(\mathbf{r}) e_{xc}(n(\mathbf{r})). \tag{5.10}$$

Accordingly, the exchange-correlation potential $V_{xc}^{LDA}[n(\mathbf{r})]$ in LDA reads as:

$$V_{xc}^{LDA}[n(\mathbf{r})] = \frac{\delta E_{xc}^{LDA}[n]}{\delta n(\mathbf{r})} = e_{xc}(n(\mathbf{r})) + n(\mathbf{r}) \frac{\partial e_{xc}(n(\mathbf{r}))}{\partial n(\mathbf{r})}. \tag{5.11}$$

Apparently, Eq. 5.11 depends only locally on the electron density, hence the name local density approximation. There are more advanced approximations which for instance also include gradient terms in e_{xc} [92].

5.1.4 The full potential local orbital method

The DFT calculations presented in this thesis were performed using the FPLO14 software package which is developed at the IFW Dresden and implements the full potential local orbital method (FPLO) [93]. In this section we will briefly introduce the main concept of the FPLO method. For more details the reader is relegated to references 93 and 94.

The FPLO method expands the Kohn-Sham orbitals $\phi_{\mathbf{k}i}(\mathbf{r})$ with the wave vector $\mathbf{k}$ and the band index i in non-orthogonal overlapping local atomic-like basis orbitals:

$$\phi_{\mathbf{k}i}(\mathbf{r}) = \langle \mathbf{r}|\mathbf{k}i\rangle = \sum_{\mathbf{R}\mathbf{s}L} C_{L\mathbf{s},\mathbf{k}i} \langle \mathbf{r}|\mathbf{R}\mathbf{s}L\rangle \, e^{i\mathbf{k}(\mathbf{R}+\mathbf{s})}, \tag{5.12}$$

with

$$\langle \mathbf{r}|\mathbf{R}\mathbf{s}L\rangle = \Phi_{\mathbf{s}}^{l}(|\mathbf{r}-\mathbf{R}-\mathbf{s}|)\, Y_L(\mathbf{r}-\mathbf{R}-\mathbf{s}). \tag{5.13}$$

Here $\mathbf{R}$ labels the Bravais vectors and $\mathbf{s}$ the basis vectors in the unit cell. $L = \nu, l, m$ denotes a set of quantum numbers and $C_{L\mathbf{s},\mathbf{k}i}$ are coefficients. Y_L represents spherical harmonics and Φ is the radial part of the atomic-like orbital. With Eq. 5.12 the Kohn-Sham equations reduce to the following matrix equation:

$$\sum_{\mathbf{R}\mathbf{s}L} \langle \mathbf{0}\mathbf{s}'L'|\hat{H}|\mathbf{R}\mathbf{s}L\rangle \, C_{L\mathbf{s},\mathbf{k}i} e^{i\mathbf{k}(\mathbf{R}+\mathbf{s}-\mathbf{s}')} = \sum_{\mathbf{R}\mathbf{s}L} \langle \mathbf{0}\mathbf{s}'L'|\mathbf{R}\mathbf{s}L\rangle \, C_{L\mathbf{s},\mathbf{k}i} \epsilon_{\mathbf{k}i} e^{i\mathbf{k}(\mathbf{R}+\mathbf{s}-\mathbf{s}')} \tag{5.14}$$

$$HC = SCE, \tag{5.15}$$

with the matrices:

$$(H)_{L'\mathbf{s}',L\mathbf{s}} = \sum_{\mathbf{R}} \langle \mathbf{0}L'\mathbf{s}'|\hat{H}|\mathbf{R}L\mathbf{s}\rangle \, e^{i\mathbf{k}(\mathbf{R}+\mathbf{s}-\mathbf{s}')} \tag{5.16}$$

$$(S)_{L'\mathbf{s}',L\mathbf{s}} = \sum_{\mathbf{R}} \langle \mathbf{0}L'\mathbf{s}'|\mathbf{R}L\mathbf{s}\rangle \, e^{i\mathbf{k}(\mathbf{R}+\mathbf{s}-\mathbf{s}')} \tag{5.17}$$

$$E = \mathrm{diag}(\epsilon_{\mathbf{k}i})\,. \tag{5.18}$$

The numerical effort to solve Eq. 5.15 can be significantly reduced by dividing the basis states into valence states $|\mathbf{R},\mathbf{s}L_v\rangle$ and core states $|\mathbf{R},\mathbf{s}L_c\rangle$. Per definition core states on different sites do not overlap:

$$\langle\mathbf{R}'\mathbf{s}'L_c'|\mathbf{R}\mathbf{s}L_c\rangle = \delta_{cc'}\delta_{\mathbf{R}\mathbf{R}'}\delta_{\mathbf{s}\mathbf{s}'}, \tag{5.19}$$

and obey

$$\hat{H}\,|\mathbf{R}\mathbf{s}L_c\rangle = |\mathbf{R}\mathbf{s}L_c\rangle\,\epsilon_{\mathbf{s}L_c}. \tag{5.20}$$

Therefore, the overlap matrix S has four blocks:

$$S = \begin{pmatrix} S_{cc} & S_{cv} \\ S_{vc} & S_{vv} \end{pmatrix}, \tag{5.21}$$

where $S_{cc} = \mathbb{1}$ and the Hamiltonian matrix simplifies to

$$H = \begin{pmatrix} H_{cc} & H_{cc}S_{cv} \\ S_{vc}H_{cc} & H_{vv} \end{pmatrix}, \tag{5.22}$$

with $H_{cc} = \mathrm{diag}(\epsilon_{\mathbf{s}L_c})$. The particular form of S allows for the application of a simplified Cholesky decomposition of S [94]:

$$S = \begin{pmatrix} \mathbb{1} & S_{cv} \\ S_{vc} & S_{vv} \end{pmatrix} = \begin{pmatrix} \mathbb{1} & 0 \\ S_{vc}^L & S_{vv}^L \end{pmatrix}\begin{pmatrix} \mathbb{1} & S_{cv}^R \\ 0 & S_{vv}^R \end{pmatrix} = S^L S^R. \tag{5.23}$$

Inserting Eq. 5.23 into Eq. 5.15 yields

$$(S^L)^{-1}H(S^R)^{-1}D = DE, \quad D = S^R C. \tag{5.24}$$

After some algebra and with the help of Eq. 5.22 the eigenvalue problem reduces to:

$$(S_{vv}^L)^{-1}(H_{vv} - S_{vc}H_{cc}S_{cv})(S_{vv}^R)^{-1}D_{vv} = D_{vv}E_v, \tag{5.25}$$

and the coefficient matrix C is given by:

$$C = (S^R)^{-1}D. \tag{5.26}$$

As Eq. 5.25 shows, the eigenvalue problem is reduced to the valence state basis functions, although all electrons remain in the calculation. This provides a significant performance gain in particular for heavy atoms.

5.2 Angle-resolved photoemission spectroscopy

When light shines on a metallic sample very often electrons – so-called photoelectrons – are emitted from the surface. This effect is known as the photoelectric effect which was first explained by A. Einstein in 1905 [95]. Angle-resolved photoemission spectroscopy (ARPES) exploits exactly this effect in order to study the electronic structure of solids. On the one hand, the difference between the kinetic energy of the photoelectron and the photon energy of the incident light contains information about the binding energy of the electron in the crystal. On the other hand, the emission angle of the photoelectron is related to the in-plane crystal momentum of its initial state.

Nowadays, APRES has been established as a standard technique to study the low-energy electronic structure of solids. However, one important limitation of APRES is its extreme surface sensitivity – at least in the ultra-violet (UV) regime. Accordingly, UV ARPES is predominantly employed for layered systems which allow for an *in situ* preparation of the sample surface under ultra-high vacuum.

In this section some general aspects of ARPES will be briefly reviewed along with a few theoretical considerations that may be helpful for the interpretation of the calculations and data presented in chapter 5.4. Comprehensive introductions may be found in references 96–99.

5.2.1 General aspects

In a typical ARPES experiment (cf. Fig. 5.1 (a)) a clean sample surface is illuminated with ultra-violet light and the intensity of the photoelectrons is measured as a function of their kinetic energy E_{kin} and emission angles φ and ϑ. As depicted in Fig. 5.1 (b), due to the energy conversation law, the initial state energy of the electron E_i is related to the measured kinetic energy via:

$$E_{kin} = h\nu - \Phi - |E_i|, \tag{5.27}$$

where $h\nu$ is the photon energy of the incident light and Φ is the work function. Φ is an individual property of the respective material and corresponds to the minimal energy needed to lift an electron from the Fermi level into the vacuum. Typical values of Φ are in the order of several eV which is the reason that the photoelectric effect is in general not observed for visible light. When the photoelectron leaves the crystal surface the initial state crystal momentum parallel to the surface is conserved and linked to the polar angle via:

$$|\mathbf{k}_{\|}| = \frac{1}{\hbar}\sqrt{2m_e E_{kin}} \cdot \sin\vartheta. \tag{5.28}$$

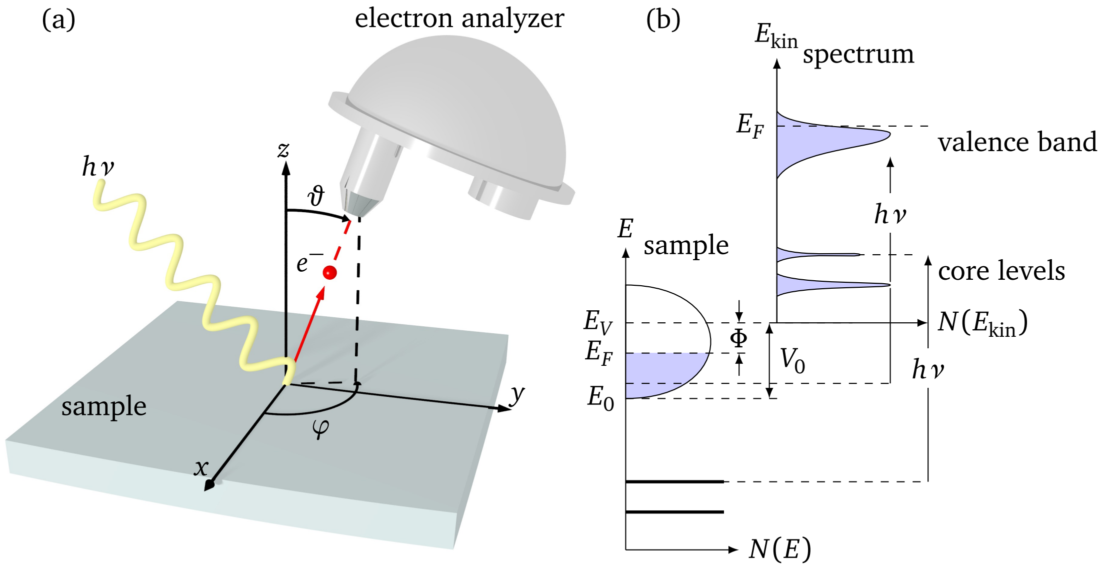

Figure 5.1: Experimental geometry of an ARPES experiment and energetics of the photoemission process. (a): The experimental geometry. The intensity of the emitted photoelectrons is measured as a function of the kinetic energy E_{kin} and the polar (ϑ) and azimuthal (φ) angles. (b): Energetics of the photoemission process. The kinetic energy E_{kin} of the photoelectron is given by the difference between the binding energy of the electron in the sample and the work function Φ. Figures are in the style of reference 97.

For typical excitation energies $\lesssim 100\,\mathrm{eV}$ the momentum of the photon is small compared to the initial state momentum of the photoelectron and, hence, can be neglected in Eq. 5.28. At this point it is important to note that $\mathbf{k}_{\parallel}$ refers to a crystal momentum in the extended-zone scheme, which will be crucial for the discussion of supercell band structures in the next section 5.3.

Since the crystal surface constitutes a broken translational symmetry, the initial state crystal momentum perpendicular to the surface $\mathbf{k}_{\perp}$ is not conserved. For strictly two-dimensional band structures this would not cause any problems but in the general case with finite $\mathbf{k}_{\perp}$ dispersions one has to make assumptions about the final state of the photoelectron in order to reveal $\mathbf{k}_{\perp}$. Widely used is the assumption that the final state of the photoelectron is a plane wave, which should be valid for rather high excitation energies. In this approximation $\mathbf{k}_{\perp}$ is given by:

$$|\mathbf{k}_{\perp}| = \frac{1}{\hbar}\sqrt{2m_e(E_{kin}\cos^2\vartheta + V_0)}, \tag{5.29}$$

where V_0 denotes the inner potential and needs to be determined experimentally. The most convenient method to determine V_0 is to measure a series of spectra at normal emission ($\mathbf{k}_{\parallel} = 0$) with varying incident photon energy. V_0 can then be deduced from the observed periodicity in these spectra [97].

5.2.2 The spectral function

So far the emission angle and kinetic energy of the photoelectron have been related to the initial state crystal momentum and initial state energy. Now the actually measured ARPES intensity will be discussed, which demands some theoretical considerations.

Within the so-called sudden approximation the current of photoelectrons reads as:

$$I(\mathbf{k},\omega) \sim \sum_{f,i} |\underbrace{\mathbf{e}\cdot\langle f|\mathbf{p}|i\rangle}_{\Delta^{\mathbf{k}}_{fi}}|^2 A_{ii}(\mathbf{k},\omega), \tag{5.30}$$

where $|f\rangle$ denotes the final state of the photoelectron and $|i\rangle$ is a one-electron initial state [100, 101]. ω is the difference between the energy of the photoelectron in the final state and the excitation energy ($\omega = \epsilon^{\mathbf{k}}_f - h\nu$). $\mathbf{e}$ is the polarization vector of the light and $\mathbf{p}$ the electron momentum operator. The factor $A_{ii}(\mathbf{k},\omega)$ is the spectral function of the retarded single-particle Greens function. The coefficients $\Delta^{\mathbf{k}}_{fj}$ are commonly referred to as one-particle matrix elements. For non-interacting electron systems the spectral function reduces to delta peaks at the one-electron eigenenergies $\epsilon^{\mathbf{k}}_i$ and, hence, $I(\mathbf{k},\omega)$ is simply given by a band structure $\epsilon^{\mathbf{k}}_i$ modulated by $\Delta^{\mathbf{k}}_{fi}$:

$$I(\mathbf{k},\omega) \sim \sum_{f,i} |\Delta^{\mathbf{k}}_{fi}|^2 \delta(\omega - \epsilon^{\mathbf{k}}_i). \tag{5.31}$$

However, for interacting electron systems $A(\mathbf{k},\omega)$ can become a complicated function. By absorbing the many-body correlations into a complex self energy $\Sigma(\mathbf{k},\epsilon^{\mathbf{k}}_i)$ the spectral function may be written as:

$$A_{ii}(\mathbf{k},\omega) = \frac{1}{\pi} \frac{|\Sigma''(\mathbf{k},\epsilon^{\mathbf{k}}_i)|}{[\omega - \epsilon^{\mathbf{k}}_i - \Sigma'(\mathbf{k},\epsilon^{\mathbf{k}}_i)]^2 - [\Sigma''(\mathbf{k},\epsilon^{\mathbf{k}}_i)]^2} \tag{5.32}$$

The real part of the self energy $\Sigma'(\mathbf{k},\epsilon^{\mathbf{k}}_i)$ basically shifts the single-particle energy eigenvalues of the non-interacting problem. In contrast, the imaginary part $\Sigma''(\mathbf{k},\epsilon^{\mathbf{k}}_i)$ causes a broadening compared to the non-interacting case.

As can be seen from Eq. 5.30 the photocurrent is not only governed by the spectral function but also influenced by the one-particle matrix elements $\Delta^{\mathbf{k}}_{fi}$. These matrix elements depend on the excitation energy ω, the polarization vector $\mathbf{e}$ as well as on the initial and final states. Their behavior can become very complicated which one should keep in mind when interpreting ARPES spectra [102].

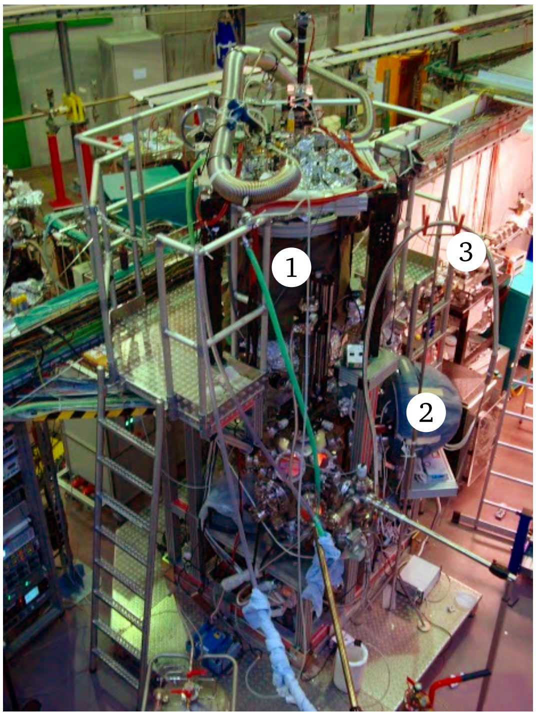

Figure 5.2: The “one-cube” ARPES end-station at beamline UE112 at BESSY. The numbers in the photograph indicate the cryo-manipulator (1), the electron-analyzer (2) and the beamline (3).

5.2.3 Experimental setup

The experimental method ARPES has largely profited from the increased availability of synchrotron radiation facilities during the last decades. In a typical experimental setup the white synchrotron-radiation produced in an undulator is monochromized and then focused on the sample [103]. The kinetic energy and the emission angle of the photoelectrons are measured by a hemispherical analyzer. It is necessary to keep the sample chamber and the analyzer under ultra-high vacuum conditions at pressures below 10^{-10} mbar.

The ARPES experiments presented in this thesis were conducted at the “one-cube” ARPES end-station at beamline UE112 at the Berlin Synchrotron (BESSY) which is shown in Fig. 5.2. The name “one-cube” originates from the design specifications for this end-station: It can perform with an energy resolution of the beamline and the analyzer below 1 meV and at sample temperature below 1 K.

However, for the measurements presented in this thesis the overall energy resolution of the used Gammadata R4000 electron analyzer was below 20 meV. We used p-polarized light with a photon energy of 96 eV. For this incident photon energy the final state crystal momentum at normal emission corresponds to the Γ-point as shown in reference [104]. The beam spot size on the sample was approximately 100 × 100 μm. The pressure in the sample chamber was below $1.1 \cdot 10^{-10}$ mbar and the sample temperature was kept at 1 K. The samples used for the ARPES experiments were from the same batch as the samples used in chapter 4 for the XRD measurements.

5.3 Supercell band structures and unfolding

We have seen in chapter 2 that a charge density wave in general breaks the discrete translational symmetry of the underlying crystal lattice. A popular practice to calculate the electronic structure of such phases with lowered symmetry in DFT is the supercell approach[3].

Since the supercell is larger in real space as the normal cell of the undisturbed structure the resulting first Brillouin zone of the supercell in reciprocal space becomes smaller and bands from the Brillouin zone of the normal cell are "folded"[4] into this new supercell Brillouin zone. For a large supercell the supercell Brillouin zone becomes very small and filled with many folded bands. However, the potential that gives rise to the supercell is – in general – rather small compared to the potential associated with the average crystal structure of the normal cell. Consequently, it should only slightly alter the band structure corresponding to the normal cell. In fact, in the limit of a vanishing supercell potential the band structure of the supercell calculation should coincide with the band structure of the normal cell. Nonetheless, even for vanishing supercell potential the supercell approach still yields the band structure in the supercell Brillouin zone with all folded bands. Therefore, it is clear that such a band structure contains little information and hardly resembles experimental ARPES spectra. As explained in section 5.2 the spectra measured in ARPES are – apart from matrix element effects – proportional to the spectral function $A(\mathbf{k}, \omega)$ of the retarded one-particle Green function. However, the supercell approach band structure only indicates for which momenta $\mathbf{k}$ and energies ω states exist but there is no information about their spectral weight $A(\mathbf{k}, \omega)$. This can also be formulated in another way: The supercell calculation produces a band structure in the reduced or repeated zone scheme. However, ARPES experiments are rather related to the extended zone scheme [97, 105].

We now further illustrate this problem by considering an explicit example of a simple 1D tight-binding model with a half-filled s-band and only nearest neighbor hopping $t = t_1 = t_2$ as illustrated in Fig. 5.3 (a). The corresponding electronic structure is given by a single band

---

[3] In cases where the order is commensurate one may define a supercell and a superlattice which has again a (different) discrete translational symmetry. However, for incommensurate modulations the translational symmetry is – at least in 3D – completely lost and a definition of a supercell is not straightforward and involves approximations (cf. 4.1).

[4] In literature these bands are often referred to as folded into the supercell Brillouin zone, but the proper term would be "translated".

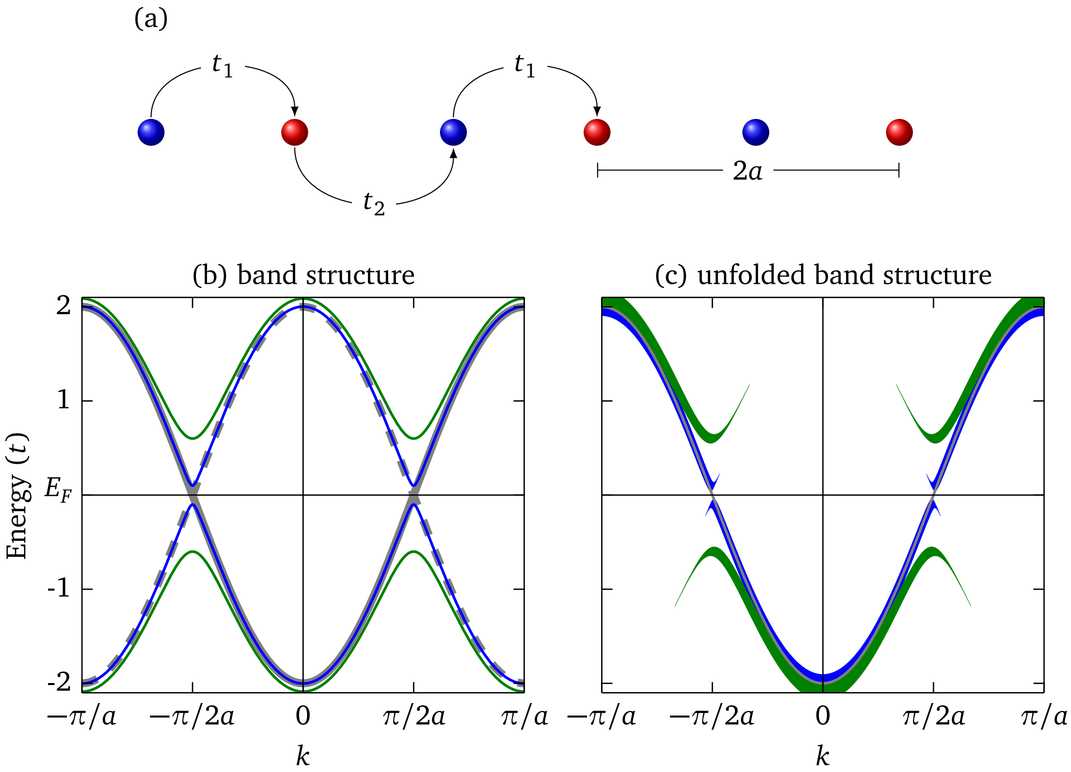

Figure 5.3: Band structure of a 1D chain (a) with a half-filled s-band. (b) shows the bare band structure obtained by diagonalizing the tight-binding Hamiltonian. The thick gray line indicates the unreconstructed band ($V = t_1 - t_2 = 0$) calculated in the normal cell and the dashed line corresponds to the folded band which appears when the calculation is done in the supercell. Blue and green lines are reconstructed bands for different finite values of V. (c) shows the corresponding unfolded band structure where the thickness of the bands indicates the spectral weight $A(\mathbf{k}, \omega)$ which is the relevant physical quantity. The spectral weight is concentrated in the vicinity of the unreconstructed band.

of the form $\epsilon(k) = -2t\cos(ka)$ (light gray line in Fig. 5.3 (b)). As explained in chapter 2 such a system is, due to the perfect nesting of the Fermi surface, susceptible to a periodic modulation corresponding to the nesting vector π/a which causes the hopping parameters to become different ($t_1 \neq t_2$). In order to calculate the electronic structure of this modulated chain the tight-binding Hamiltonian has to be extended into the supercell, which is twice as large as the normal cell. Diagonalization of the 2 × 2 supercell Hamiltonian yields two new eigenvectors with energy bands:

$$\epsilon_{1,2}(k) = \pm\sqrt{V^2 + 4\tilde{t}\cos^2(ka)}, \quad V = (t_1 - t_2), \quad \tilde{t} = \sqrt{t_1 t_2}, \tag{5.33}$$

which are separated by an energy gap of the size $2V$. In Fig. 5.3 (b) these bands are shown for two different finite values of V (blue and green line). Note that the representation of the bands in Fig. 5.3 (b) corresponds to the repeated zone scheme of the supercell Brillouin zone which ranges from $-\frac{\pi}{2a}$ to $\frac{\pi}{2a}$. However, the intensity measured in an ARPES experiment is proportional to the spectral function $A(\mathbf{k},\omega)$ which is predominantly concentrated along the band dispersions in the extended zone scheme. An approximation for $A(\mathbf{k},\omega)$ may be obtained by the so-called unfolding procedure [28, 105, 106]. When we denote the reconstructed (unreconstructed) bands and states with $\epsilon_J(\mathbf{k})$ ($\epsilon_j(\mathbf{k})$) and $|J\mathbf{k}\rangle$ ($|j\mathbf{k}\rangle$), respectively, the spectral function can be approximated by:

$$A(\mathbf{k},\omega) = \sum_{j,J} |\langle j\mathbf{k}|J\mathbf{k}\rangle|^2 \delta(\omega - \epsilon_J(\mathbf{k})). \tag{5.34}$$

For the particular case shown in Fig. 5.3 $\epsilon_J(\mathbf{k})$ is given in Eq. 5.33 and $|J\mathbf{k}\rangle$ are the corresponding eigenstates with band indices $J = 1, 2$. $\mathbf{k}$ refers to a crystal momentum in the normal cell Brillouin zone. $|j\mathbf{k}\rangle$ is the eigenstate corresponding to the unreconstructed band. Fig. 5.3 (c) shows the result of Eq. 5.34 where the thickness of the lines reflects $A(\mathbf{k},\omega)$. For small V (blue) the dispersion is almost identical to the dispersion for the unreconstructed band shown in gray in Fig. 5.3 (b). As V increases the gap at $\mathrm{E_F}$ widens and more spectral weight is transferred into the back-bended bands – so-called umklapp bands. In contrast to the reconstructed bands $\epsilon_\mu(\mathbf{k})$ which obey the periodicity of the supercell Brillouin zone, $A(\mathbf{k},\omega)$ exhibits the periodicity of the unreconstructed normal cell Brillouin zone. Intuitively, the form of Eq. 5.34 can be understood in the following way: For $V = 0$ the 2×2 supercell Hamiltonian yields two bands: The “original” band (light gray line in Fig. 5.3 (a)) and a folded band which is shown as a dashed gray line in Fig. 5.3 (a). The projection in Eq. 5.34 guarantees that the weight of the “original” band is equal to one while the other band – the folded band – has zero weight, because both states are orthogonal and the unreconstructed eigenstate is exactly given be one of them. For finite V the “original” eigenstate starts to mix with the folded eigenstate in the vicinity of the energy gap, hence both bands attain finite spectral weight close to the energy gap.

As demonstrated by Ku *et al.* an equivalent unfolding scheme may be applied to first principle DFT band structure calculations [106]: In this case the states $|j\mathbf{k}\rangle$ and $|J\mathbf{K}\rangle$ are Kohn-Sham states of the normal cell and supercell, respectively, where $\mathbf{K}$ was introduced to denote a crystal momentum in the supercell Brillouin zone. If one projects $|J\mathbf{K}\rangle$ onto local Wannier orbitals $|n\mathbf{r}\rangle$ instead of the band orbitals $|j\mathbf{k}\rangle$, it is possible to unfold the contribution of a certain orbital character of each band. Note that n refers to an orbital index instead of a band index and $\mathbf{r}$ denotes a normal cell lattice vector. The spectral function

$$A_n(\mathbf{k},\omega) = \sum_{J,\mathbf{K}} |\langle n\mathbf{k}|J\mathbf{K}\rangle|^2 \delta(\omega - \epsilon_J(\mathbf{K})), \tag{5.35}$$

where $|n\mathbf{k}\rangle = \sum_r |n\mathbf{r}\rangle \langle n\mathbf{r}|n\mathbf{k}\rangle = \sum_r |n\mathbf{r}\rangle\, e^{i\mathbf{kr}}/\sqrt{l}$ are the Fourier transform of the Wannier orbitals hence measures the spectral weight associated with $|n\mathbf{r}\rangle$ at $\mathbf{k}$ and ω (l is the number of the normal cell lattice sites).

The use of local Wannier orbitals can markedly reduce the numerical expense of calculating Eq. 5.35 as shown by Ku *et al.* [106]. Therefore, a definition of Wannier functions in the supercell $|N\mathbf{R}\rangle$, where $\mathbf{R}$ denotes a superlattice vector is needed. In addition a consistent mapping onto the normal cell Wannier functions $|N\mathbf{R}\rangle \rightarrow |\mathbf{R}+\mathbf{r}, n(N)\rangle$, where $\mathbf{r}$ is a normal cell lattice vector within the first supercell and $n(N)$ is a normal cell Wannier orbital index must exist. In this case it can be shown (see reference [106] for details) that the factor

$$\langle n\mathbf{k}|J\mathbf{K}\rangle \propto \sum_N \delta_{[\mathbf{k}],\mathbf{K}}\delta_{n,n'(N)}e^{-i\mathbf{kr}(N)}\,\langle N\mathbf{K}|J\mathbf{K}\rangle \tag{5.36}$$

reduces to a projection of the supercell Kohn-Sham state $|J\mathbf{K}\rangle$ onto the supercell Wannier basis $|N\mathbf{K}\rangle = \sum_{\mathbf{R}} |N\mathbf{R}\rangle\, e^{i\mathbf{KR}}/\sqrt{L}$ (L is the number of supercell lattice sites) weighted with phase factors which retain the translational symmetry of the normal cell. Note that $[\mathbf{k}]$ means: translate $\mathbf{k}$ from the normal cell Brillouin zone into the super cell Brillouin zone.

The unfolding scheme becomes very straightforward in FPLO because the Kohn-Sham states are already expressed in a localized basis. Accordingly, the distribution of certain local symmetries to the unfolded spectral weight may be simply obtained by projecting the Kohn Sham states of the super cell onto the localized FPLO basis orbitals with appropriate phase factors. It is therefore not necessary to calculate the band structure of the normal cell.

5.4 Orbital texture and charge density waves in transition metal dichalcogenides

In the following section we present the key results of this chapter, namely the intimate relation between charge density wave order and orbital order in $1T$-TaS$_2$ and the implications for the electronic structure of this compound.

As explained in section 3.2 it was proposed early on that the low-temperature commensurate C-CDW, which is illustrated in Fig. 5.4 (a),(b), features many-body Mott physics [56]. Experimental evidence for the presence of Mott physics in $1T$-TaS$_2$ has indeed been obtained recently by time-resolved spectroscopies, which observed the ultra-fast closing of a charge excitation gap, which has been interpreted as a fingerprint of significant electron-electron interactions [60–62] (cf. section 3.2.2).

Even though the Mott scenario for the C-CDW is widely accepted, important experimental facts remain to be understood: the very strong suppression of the C-CDW with external pressure is puzzling (cf. section 4.3). Already above 0.6 GPa, the C-CDW is no longer stable,

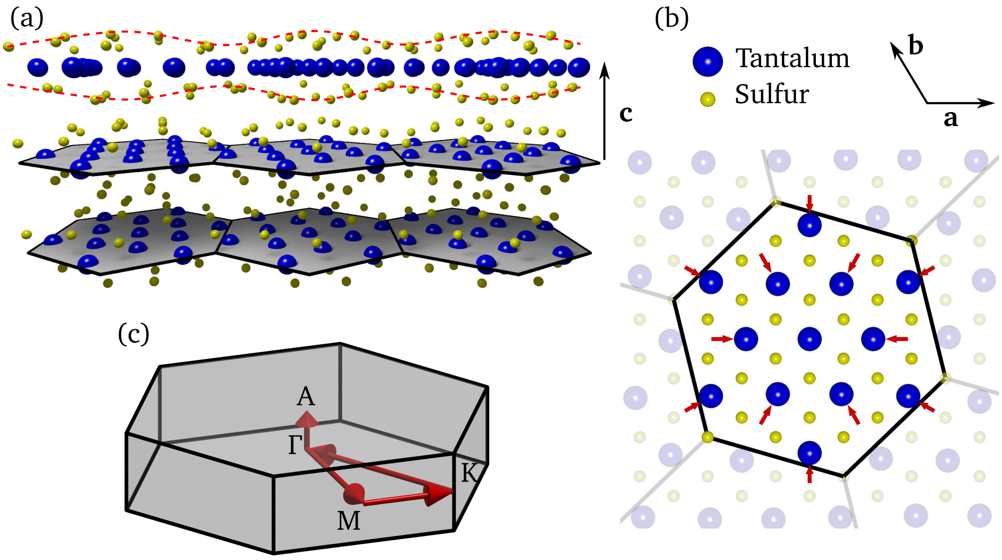

Figure 5.4: The $\sqrt{13} \times \sqrt{13}$ superstructure of $1T$-TaS$_2$. (a) and (b): View parallel to the ab-planes and along the c-axis, respectively ($\mathbf{a}, \mathbf{b}$,$\mathbf{c}$: lattice vectors of the undistorted P$\bar{3}$m1 crystal structure). The Ta-displacements indicated by red arrows in (b) are mainly parallel to the ab-planes, resulting in clusters containing 13 Ta-sites. Red dashed lines in (a) highlight the breathing of the S-sites perpendicular to the ab-plane. The Brillouin zone corresponding to the undistorted crystal structure along with high symmetry points is shown in (c).

although nesting conditions, band widths as well as the lattice structure remain essentially unchanged. It is also not clear how ordered defects (discommensurations cf. section 4.3) within the C-CDW order, which emerge in the NC-CDW upon heating [55, 65] and which do not cause significant changes in the bandwidths, can render the onsite Coulomb interaction U completely ineffective [48]. In the following we will show that all these issues are explained consistently in terms of orbital textures that are intertwined with the CDW. In addition to this, we also demonstrate that this new twist to the physics of CDWs also provides a new and powerful device concept for future applications based on TMDs.

5.4.1 Supercell calculations

As discussed at full length in section 4.5, an important feature of the C-CDW is its partially disordered stacking along the c-axis: characterizing the relative alignment of the C-CDW in adjacent ab-planes in terms of stacking vectors $\mathbf{T}_S$, which connect the central Ta-sites in successive layers (cf. Fig. 5.6 (b) and (c)), the c-axis stacking is given by an alternation of $\mathbf{T}_S = 1\mathbf{c}$ with a random choice from the three symmetry equivalent vectors $\mathbf{T}_S = 2\mathbf{a} + \mathbf{c}$, $\mathbf{T}_S = 2\mathbf{b} + \mathbf{c}$ or $\mathbf{T}_S = -2(\mathbf{a} + \mathbf{b}) + \mathbf{c}$ [85, 86].

The effect of the different $\mathbf{T}_S$ on the electronic structure has so far remained unexplored.

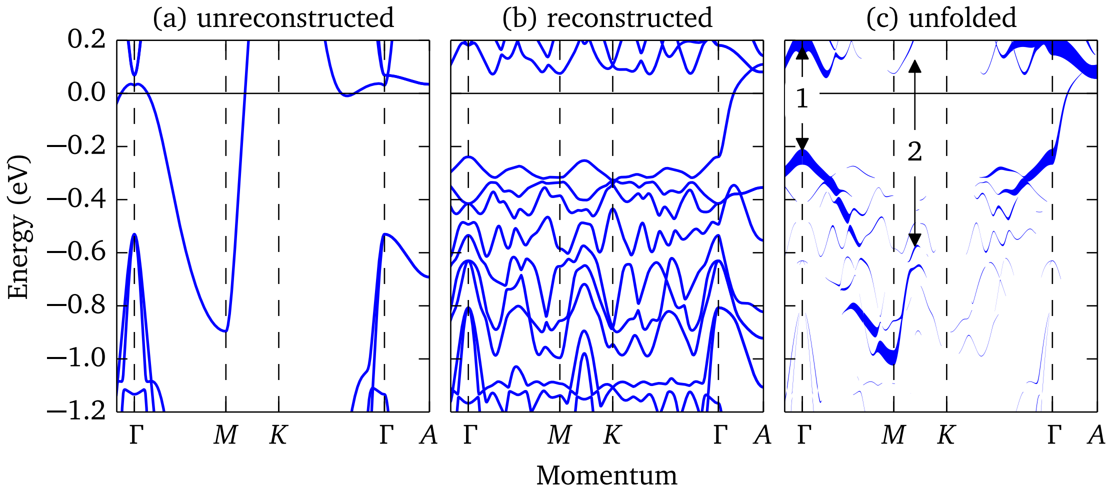

Figure 5.5: Unfolding of the supercell band structure of 1*T*-TaS_2. (a): Unreconstructed LDA band structure along the high symmetry direction in the Brillouin zone shown in Fig. 5.4 (c). (b) Reconstructed LDA supercell band structure along the same high symmetry directions as in (a). (c): The unfolded band structure. The thickness of bands measures the spectral weight at this position. Arrows indicate the gaps at Γ and between M and K which are commonly named Mott-gap (1) and CDW-gap (2), respectively.

Our highly efficient DFT approach (see section 5.1.4 for details), however, enables us to study these effects for the first time within the local density approximation (LDA).

For our *ab initio* calculations we chose two superstructures with $\mathbf{T}_S = 1\mathbf{c}$ and $\mathbf{T}_S = 2\mathbf{a} + \mathbf{c}$, respectively, which represent the two metastable types of stacking found experimentally. In section 4.5 we introduced a notation in which the symbols $\langle \mathbf{t}_0 \rangle$ and $\langle \mathbf{t}_2 \rangle$ were used to denote the periodic and infinite stacking with $\mathbf{T}_S = 1\mathbf{c}$ and $\mathbf{T}_S = 2\mathbf{a} + \mathbf{c}$, respectively. Throughout this section the same notation will be used.

For both calculations the modulation of the atomic positions within the TaS_2-layers was kept the same. In other words, only the stacking of the TaS_2-layers was changed but not the structure of these layers itself. Technical details of the calculations are summarized in section 5.4.4.

Fig. 5.5 (a) and (b) show the band structures for the undistorted lattice and the C-CDW with the stacking $\langle \mathbf{t}_0 \rangle$, respectively. The band dispersions are shown along high symmetry directions of the Brillouin zone of the unmodulated structure depicted in Fig. 5.4 (c). In good agreement with previous DFT results [107, 108], the band structure in the plane through Γ, M and K is fully gapped and only along Γ-A a Fermi level crossing occurs. This yields a one-dimensional metal, in-line with recent reports [109]. As we have discussed in section 5.3 a major disadvantage of such supercell calculations is, however, that the additional backfolded bands only indicate for which momenta $\mathbf{k}$ and energies ω electronic states exist. There is no information about the spectral weight of these states. Exactly this information is provided by the so-called spectral function $A(\mathbf{k}, \omega)$ [96], which is the physically relevant quantity that can be accessed experimentally by ARPES (cf. section 5.2). As described in section 5.3 an approximation for $A(\mathbf{k}, \omega)$ within DFT can be obtained using the so-called unfolding procedure [106]. The result of this unfolding procedure for the band structure shown in Fig. 5.5 (b) is presented in Fig. 5.5 (c), where the thickness of the individual bands reflects $A(\mathbf{k}, \omega)$. It is clearly visible that only a small fraction of the reconstructed band structure carries substantial spectral weight. Unlike the bands in Fig. 5.5 (b), the unfolded band structure allows to clearly identify dispersing bands and, correspondingly, the size and location of energy gaps. Specifically, our calculation yields two gaps around the Fermi level E_F, indicated by arrows in Fig. 5.5 (c). As outlined in section 3.2.2 the gap at Γ is usually interpreted as a Mott-gap due to the electron-electron interaction U [28, 60]. Between M and K a second gap is formed, which fits well to the Fermi surface nesting vector and is therefore commonly assigned to a CDW-gap due to the electron-phonon coupling. It is very important to note here that our calculations do not include any onsite interactions U. The fact that the gap at Γ occurs already without including U is therefore remarkable, as it already shows that the gap at Γ is not mainly caused by Mott physics.

5.4.2 Impact of the CDW-layer stacking

In Fig. 5.6 we compare the unfolded LDA band structures for $\langle \mathbf{t}_0 \rangle$ and $\langle \mathbf{t}_2 \rangle$, which yields the first major result of this study: the dramatic dependence of the electronic structure on the CDW-stacking. As can be observed in Fig. 5.6 (d) and (e), essential features of the low-energy electronic structure depend critically on the stacking. Most notably the bands around the Γ-point are strongly affected. While for $\langle \mathbf{t}_2 \rangle$ the in-plane dispersions show E_F-crossings along Γ-K and Γ-M, both crossings are completely absent for $\langle \mathbf{t}_0 \rangle$. Even the size of the so-called CDW-gap between M-K depends on the stacking, although it prevails for both stackings. Therefore, a transition from an in-plane metal to an in-plane semiconductor occurs as a function of $\mathbf{T}_S$. Considering that the ab-planes of 1*T*-TaS_2 are usually thought to realize strongly two-dimensional metallic systems, these are most surprising results.

The comparison of the two DFT models to the ARPES data in Fig. 5.6 (a) shows that the calculation for $\langle \mathbf{t}_2 \rangle$ describes the experiment very well for binding energies below -0.3 eV. Note that the $\mathbf{k}$-direction along which the ARPES data are measured is tilted with respect to the Γ-*M* direction by about 10 degree which explains the small deviations from the data of Hellmann *et al.* [36] shown in Fig. 3.5 (a) on page 20. However, it is also obvious that both DFT models fail to describe the electronic states close to E_F and, in particular, the pseudogap observed experimentally [110]. Including an onsite U at Ta does not cure this discrepancy, implying that these effects are beyond LDA+U. Indeed, the strong $\mathbf{T}_S$-dependence of the electronic structure

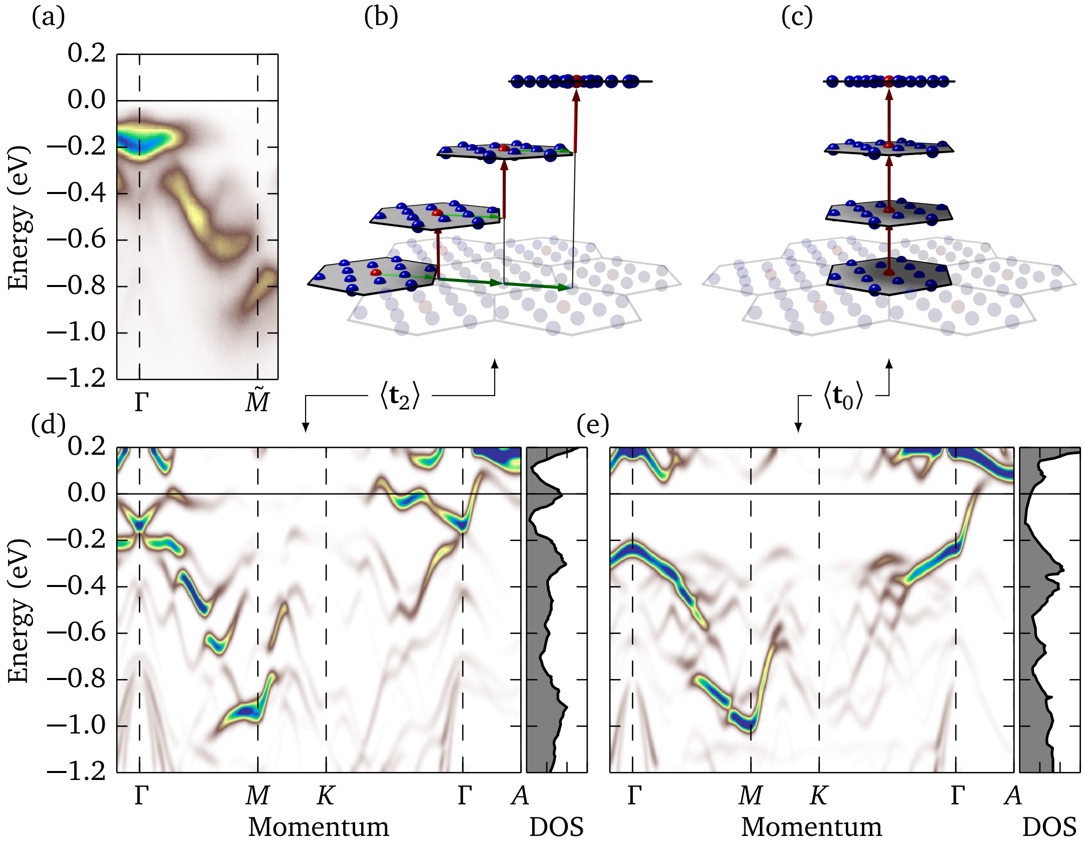

Figure 5.6: Different layer stackings and their impact on the band structure. (d) and (e): Calculated band structure for the stacking ⟨$\mathbf{t}_2$⟩ and the stacking ⟨$\mathbf{t}_0$⟩, respectively. To facilitate the comparison with ARPES data shown in (a) the bandweights have been convoluted with a Lorentzian-shaped resolution function. Note that the ARPES data are measured along a $\mathbf{k}$ direction which is tilted by about 10 degrees with respect to the Γ-M direction, hence the small deviation to previous reports (cf. Fig. 3.5 on page 20). (b) and (c): Visualization of the stacking ⟨$\mathbf{t}_2$⟩ and ⟨$\mathbf{t}_0$⟩, respectively.

suggests that these deviations are related to the stacking disorder in the real material [85], which cannot be taken into account by our DFT-models. While this issue certainly deserves scrutiny in future work, here we focus on determining the origin of the dramatic effects of $\mathbf{T}_S$. A first effort to refine the DFT-model in order to better account for the actual stacking is made in section 5.6.

5.4.3 Orbital textures

In order to determine the origin of the dramatic effects of $\mathbf{T}_S$, we calculated the charge density distribution of the uppermost occupied states in real space. As can be seen in Fig. 5.7, for both types of stacking a complex orbital texture within the ab-plane emerges. This is the second

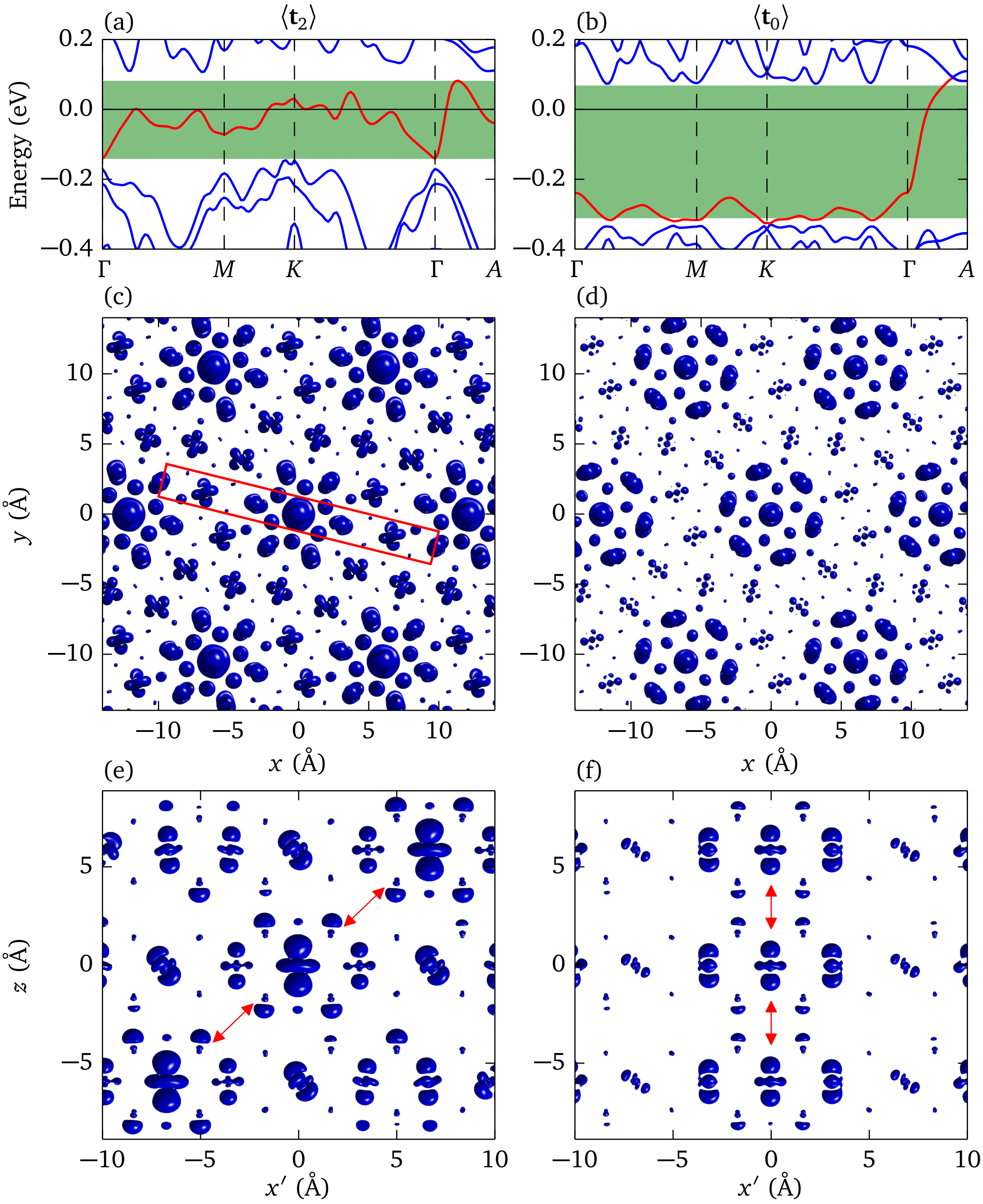

Figure 5.7: Real space illustration of the electron density corresponding the highest occupied band. (a) and (b): The band structure near E_F with the highest occupied band in red. The energy window used to calculate the energy-resolved electron density is indicated by the green area. (c) and (d): A complex orbital texture emerges within the *ab*-plane. (e) and (f): View of the *ac*-plane corresponding to the area indicated by the red rectangle in (c). (f): For $\langle \mathbf{t}_0 \rangle$ significant hopping is only allowed along the *c*-direction. (e): A substantial *ab*-component of the hopping appears for $\langle \mathbf{t}_2 \rangle$.

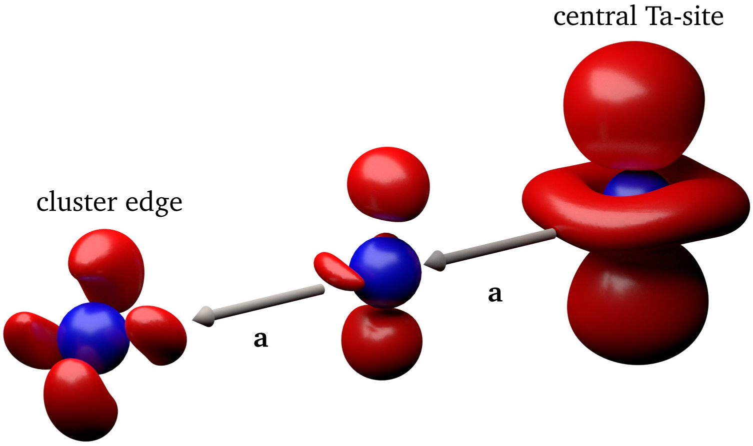

Figure 5.8: Magnification of the orbital texture for $\langle \mathbf{t}_2 \rangle$. The Ta-sites are indicated by blue spheres. The symmetry of the isosurface of the electron density (red) clearly changes from site to site.

major result of this work: the discovery of an orbital texture that is intertwined with a CDW. Note that not only the occupancy of a certain type of orbital changes spatially. Instead also the symmetry of the orbitals clearly changes from site to site, resulting in a complex orbital ordering pattern. For instance, whereas the orbital is oriented perpendicular to the ab-plane at the center of the Ta-cluster, a significant in-plane component exists at the cluster edges, as can be readily observed in the magnification of the orbital texture presented in Fig. 5.8. It is also worth mentioning that the in-plane orientation of some orbitals changes with $\mathbf{T}_S$ and that the Sulfur $3p$-states also take part in the orbital texture.

The orbital structure for $\langle \mathbf{t}_0 \rangle$ permits significant charge hopping only along c, as illustrated in Fig. 5.7 (f). In other words, the charges flow along orbital stripes along c, corresponding to the quasi one-dimensional character of the uppermost band in Fig. 5.7 (b) and Fig. 5.6 (e). This drastically changes in the case of $\langle \mathbf{t}_2 \rangle$. Now there is a significant ab-component of the hopping as illustrated in Fig. 5.7 (e), so that the uppermost band attains a larger in-plane dispersion and crosses E_F along Γ-M and Γ-K (Fig. 5.7 (a) and Fig. 5.6 (e)).

These results have important consequences: Firstly, the comparison of the ARPES data and the DFT results shows that the Γ-gap is obtained on a quantitative level without an onsite repulsion U on Ta. Although this result does not exclude the presence of electron-electron interactions, it strongly argues against U being the main cause for the Γ-gap. Instead, the band structure calculations reveal that this gap is for a large part due to the interlayer hybridization. This becomes even clearer when we consider the Γ-gap size as a function of the interlayer spacing. To this end we calculated the electronic structure for the stacking $\langle \mathbf{t}_0 \rangle$ with an enlarged c-axis parameter. As shown in Fig. 5.9 the Γ-gap size rapidly decreases with increasing c-axis

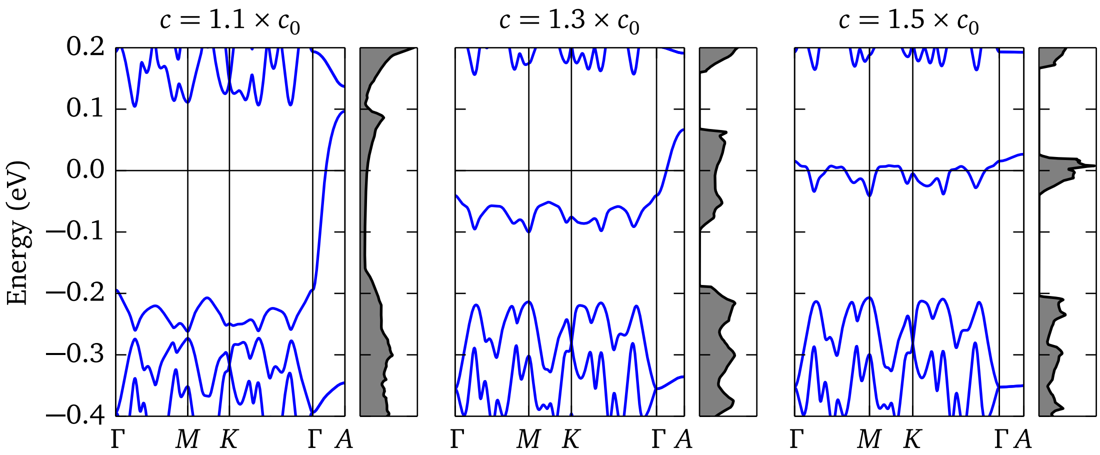

Figure 5.9: The in-plane gap as a function of the interlayer spacing for $\langle \mathbf{t}_0 \rangle$. $c_0 = 5.9$ Å denotes the c-axis parameter found experimentally.

parameter which identifies the interlayer hybridization as the crucial mechanism that causes the Γ-gap. The interlayer hybridization is in turn mostly caused by the $3z^2 - r^2$-type orbitals pointing along c, i. e., the Γ-gap is directly coupled to the orbital texture. This result naturally explains the ultra-fast response of this gap observed in time-resolved ARPES experiments (see section 3.2.2), since the disruption and reordering of the electronic orbitals can evolve on much faster timescales than the lattice.

Secondly, the presence of orbital textures explains the strong pressure dependence of the CDW-order in 1*T*-TaS$_2$, because through the orbital texture pressure has a large effect on the stability of CDW-phases with different stackings in a way that goes well beyond traditional nesting scenarios. We also stress that the crucial role of the interlayer interactions is verified experimentally by the XRD data presented in chapter 4.5 (Fig. 4.16 on page 50), which shows that the stacking changes completely across the C-CDW/NC-CDW transition. This change in stacking together with our DFT-results also rationalizes the collapse of the gap at Γ upon entering the NC-CDW with warming.

Thirdly and most importantly, the relative orientation of the orbitals in adjacent ab-planes has a spectacular effect on the band dispersions. This can be readily understood in terms of the overlap integrals, which depend critically on the relative orientation of the orbitals in adjacent layers along c (cf. Fig. 5.7 (e) and (f)). This immediately yields a new device concept, which employs metastable orbital orders for controlling the electronic structure of nanostructures: As illustrated in Fig. 5.10 for a bilayer of 1*T*-TaS$_2$, switching between the metastable orbital configurations causes a complete semiconductor-to-metal transition. In other words, by changing the orbital order in the direction *perpendicular* to the layers, one can control the conductivity *parallel* to the layers. At this point it is worth noting that the two stackings $\langle \mathbf{t}_2 \rangle$

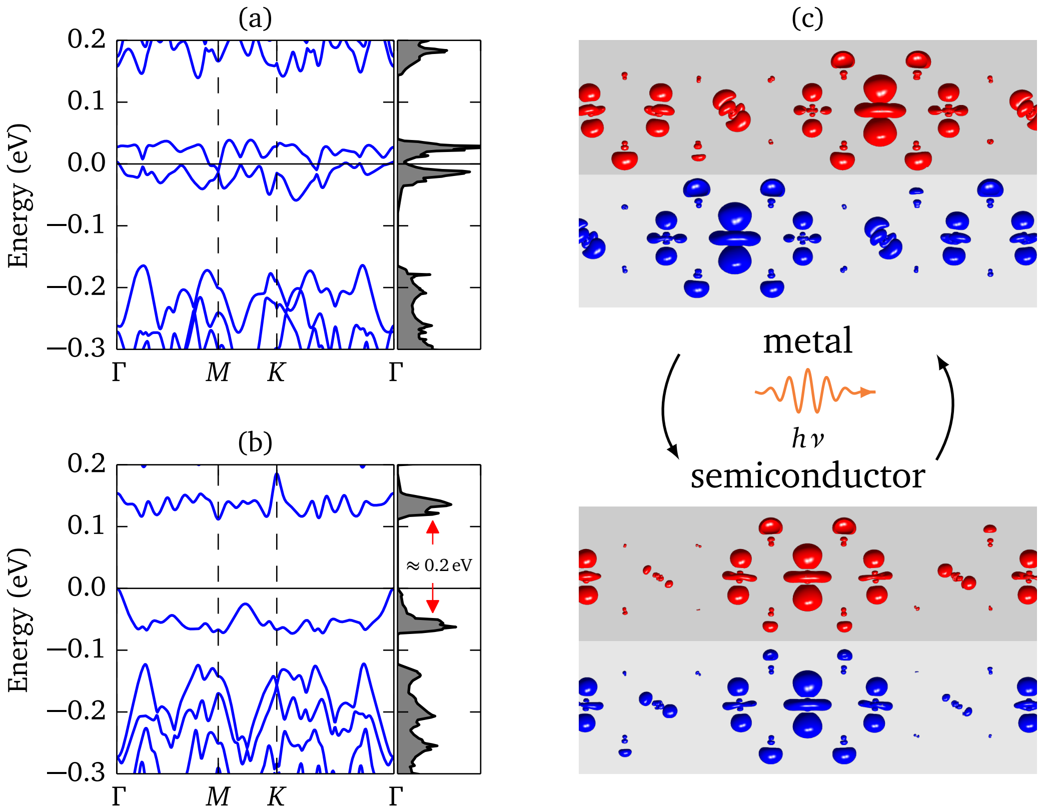

Figure 5.10: Device concept based on the switching between metastable orbital orders. Calculated band structure for a bilayer of 1*T*-TaS$_2$ with $\mathbf{T}_S = 1\mathbf{c}$ (a) and $\mathbf{T}_S = 2\mathbf{a} + \mathbf{c}$ (b). A semiconductor-to-metal transition takes place upon changing the stacking of the two layers. (c): Orbital order corresponding to the semiconducting (top) and metallic state (bottom).

and $\langle \mathbf{t}_0 \rangle$ are indeed metastable within DFT, since their calculated total energies differ only by about 10 meV (see table 5.3 on page 87)[5]. Even though the switching between orbital configurations has not yet been observed directly, a very recent experiment provides first evidence that this can be achieved reversibly and on ultra-fast timescales using optical laser pulses [63] (cf. section 3.2.2).

Orbital textures hence enable one to manipulate the band dispersion and gap structure of 1*T*-TaS$_2$ in a very effective way. They therefore provide a new route to tailor and switch the electronic properties of TMDs, possibly on the femtosecond time scale. This concept of orbitronics may hence enable to create novel, small and ultra-fast electronics, which adds to the large potential of TMDs for future device applications.

---

[5] For the bilayer systems the calculations yield a somewhat larger energy difference of about 90 meV, where the configuration with $\mathbf{t}_0$ is more stable.

5.4.4 Details of the DFT calculations

The DFT calculations were realized using the FPLO14 package [93] (cf. section 5.1.4), which has been developed at the IFW Dresden and supports unfolding of the band structure as outlined in reference 106. Due to its small basis size it allows for calculations of large supercells extremely efficiently, which makes the presented calculations numerically affordable. The supercell structure for $\langle \mathbf{t}_0 \rangle$ was derived from references 111 and 55. In order to simulate different layer stackings we transformed the hexagonal supercell into a triclinic supercell without changing the atomic displacements. The resulting structural parameters are summarized in Tab. 5.1. It is important to note that a structural relaxation, which starts from the undistorted lattice, rapidly converges against the experimentally observed superstructure. In addition, the present DFT calculations reproduce the so-called Mott- and CDW-gap on a quantitative level. This verifies our approach and shows that the present DFT-models capture the important interactions present in the real material.

5.5 Comparison to tight-binding approaches

The electronic band structure of the commensurate charge density wave phase of 1T-TaS$_2$ has previously been studied by means of tight-binding models [57, 112, 113]. In the following section these approaches will be revisited and extended. Furthermore, the comparison to the results presented in 5.4 will disclose the limitations of such tight-binding models for the simulation of complex charge density wave phases.

5.5.1 Supercell approach for tight-binding models

The usual starting point for a supercell tight-binding calculation is an effective tight-binding Hamiltonian that reproduces the DFT band structure of the normal cell within a certain energy window:

$$H = \sum_{\mathbf{r}\mathbf{r}'} \sum_{nn'} t_{\mathbf{r}n,\mathbf{r}'n'} a^{\dagger}_{\mathbf{r}n} a_{\mathbf{r}'n'}, \tag{5.37}$$

where $a^{\dagger}_{\mathbf{r}n}$ denotes a creation operator of a localized state $|\mathbf{r}n\rangle$ at the lattice vector $\mathbf{r}$ with orbital index n and $a_{\mathbf{r}'n'}$ is a corresponding annihilation operator. The hopping parameters $t_{\mathbf{r}n,\mathbf{r}'n'}$ may either be deduced by fitting the Slater-Koster hopping integrals [114] or by a Wannier analysis based on a DFT calculation.[6] However, as soon as the hopping parameters are known the Hamilton in Eq. 5.37 may be Fourier-transformed and diagonalized yielding the tight-binding band structure $\epsilon_{n\mathbf{k}}$.

---

[6] For details how the Wannier analysis is performed in FPLO see: Wannier manual of FPLO `http://www.fplo.de/download/wan_user.pdf`.

$\langle \mathbf{t}_0 \rangle$-stacking				$\langle \mathbf{t}_2 \rangle$-stacking			
cell:				cell:			
spacegroup			P$\bar{3}$ (143)	spacegroup			P$\bar{1}$ (2)
a (Å)			12.11	a (Å)			12.11
b (Å)			12.11	b (Å)			12.11
c (Å)			5.917	c (Å)			8.951
α (Deg)			90	α (Deg)			121.353
β (Deg)			90	β (Deg)			43.244
γ (Deg)			120	γ (Deg)			120
Wyckoff positions:				Wyckoff positions:			
Ta	0	0	0	Ta	0	0	0
Ta	0.288	0.216	0	Ta	0.288	0.216	0
Ta	0.521	0.148	0	Ta	-0.072	-0.288	0
S	0.179	0.051	0.275	Ta	-0.216	0.072	0
S	0.358	0.102	-0.267	Ta	0.521	0.148	0
S	0.435	0.410	-0.241	Ta	-0.372	-0.521	0
S	0.487	0.282	0.241	Ta	-0.148	0.372	0
S	2/3	1/3	-0.246	S	0.052	0.093	0.275
				S	-0.255	-0.137	0.275
				S	-0.178	0.170	0.275
				S	0.482	0.061	-0.267
				S	-0.133	-0.400	-0.267
				S	0.020	0.215	-0.267
				S	0.547	0.373	-0.241
				S	0.085	-0.473	-0.241
				S	-0.298	-0.011	-0.241
				S	0.375	0.319	0.241
				S	-0.316	-0.450	0.241
				S	-0.393	0.242	0.241
				S	0.780	0.295	-0.246

Table 5.1: Structural paramters for the supercell calculations corresponding to $\langle \mathbf{t}_0 \rangle$ and $\langle \mathbf{t}_2 \rangle$ for 1*T*-TaS_2.

In order to study the effects of a superstructure the Hamiltonian in Eq. 5.37 is transformed into the supercell. This is done by defining local orbitals $|\mathbf{R}N\rangle$ of the supercell, where N denotes the orbital index. The definition of the $|\mathbf{R}N\rangle$ has to obey a unique mapping $|\mathbf{R}N\rangle \rightarrow |\mathbf{R}+\mathbf{r}(N), n(N)\rangle$ which associates every orbital of the supercell to an orbital of the normal cell. Note that $\mathbf{R}$ is a supercell lattice vector and $\mathbf{r}$ is a normal cell lattice vector within the first supercell. Apparently, such a mapping also connects the hopping parameters of the supercell $T_{\mathbf{R}N,\mathbf{R}'N'}$ with the hopping parameters of the normal cell $t_{\mathbf{r}n,\mathbf{r}'n'}$. The supercell hopping parameters have to be scaled according to the lattice modulation which is introduced by the superstructure:

$$T_{\mathbf{R}N,\mathbf{R}'N'} = f(D) \cdot t_{\mathbf{r}(\mathbf{R},N)n(N),\mathbf{r}(\mathbf{R}',N')n(N')}, \tag{5.38}$$

where $D = D(\mathbf{R}N, \mathbf{R}'N')$ denotes the ratio between the inter-atomic distance according to the superstructure and the inter-atomic distance realized in the normal structure. The function $f(D)$ depends on the kind of hopping and is commonly approximated by D^{-5}, D^{-4} and D^{-3} for d-d, d-p and p-p-like hoppings, respectively [115]. In other words, due to the lattice distortion some bonds are strengthened and other bonds are weakened. Thus, the problem is reduced to the solution of the resulting supercell Hamiltonian:

$$H = \sum_{\mathbf{R}\mathbf{R}'} \sum_{NN'} T_{\mathbf{R}N,\mathbf{R}'N'} a^{\dagger}_{\mathbf{R}N} a_{\mathbf{R}'N'}. \tag{5.39}$$

In order to automatically derive supercell tight-binding models from DFT calculations performed with the FPLO package (see section 5.1.4), we implemented a numerical routine in the programming language Python[7]. This program uses the hopping parameters determined by the Wannier module of FPLO[8] to build the supercell Hamiltonian 5.39. The user has to supply the supercell structure and the mapping of the basis orbitals in the supercell onto the basis orbitals in the normal cell. According to this input, the hopping parameters are automatically scaled in compliance with Eq. 5.38 and the supercell Hamiltonian is diagonalized using the NumPy module [116]. In addition, unfolding of the supercell band structure as explained in section 5.3 was implemented. This program provides a convenient way to deduce supercell tight-binding models from FPLO calculations for arbitrary supercells.

---

[7] Python Software Foundation. Python Language Reference, version 2.7. Available at `http://www.python.org`.

[8] Wannier manual of FPLO `http://www.fplo.de/download/wan_user.pdf`

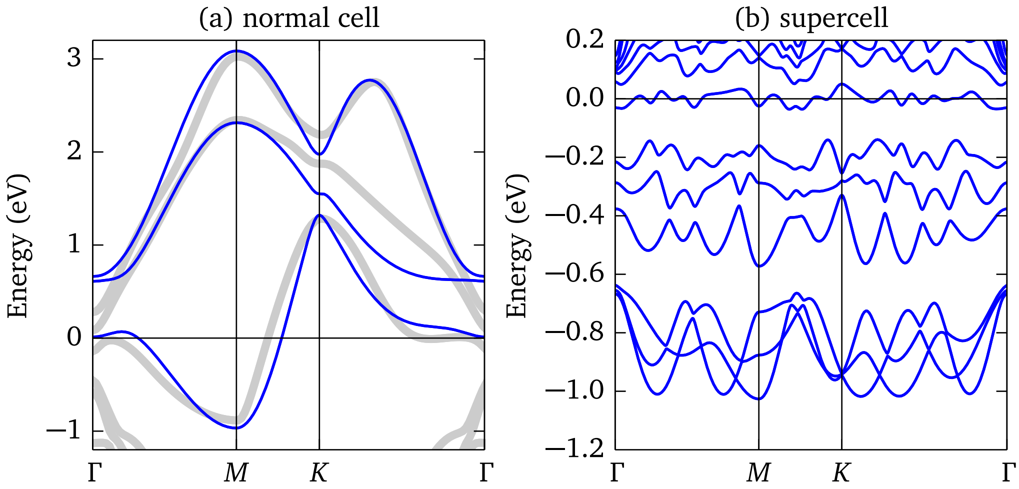

Figure 5.11: 2D tight-binding model of the commensurate charge density wave phase of 1*T*-TaS$_2$. (a) shows the three Ta 5*d*-bands near E$_F$ for the unreconstructed structure. Light gray lines correspond to the (full relativistic) LDA band structure and blue lines are the tight-binding bands for the hopping parameters from reference 117. The reconstructed band structure is shown in (b).

5.5.2 Tight-binding model for the commensurate charge density wave phase of 1*T*-TaS$_2$

Roßnagel *et al.* [117] deduced a tight-binding model for the commensurate charge density wave phase of 1*T*-TaS$_2$ including only Ta 5*d*-orbitals and effective nearest neighbor hopping. Spin-orbit coupling was added as explained in reference 118. The hopping parameters for this model were derived by fitting the appropriate Slater-Koster integrals to early LDA band structure calculations [119]. In Fig. 5.11 we reproduce the results from reference 117 using our own, aforementioned numerical routine supplied with the same hopping-parameters as used in reference 117. The first problem that arises is that the tight-binding band structure of the normal cell only roughly reproduces the LDA band structure[9] (cf. Fig. 5.11 (a)). Another apparent problem is that the present tight-binding model is strictly two-dimensional and, hence, cannot account for interlayer hybridization effects which have been shown to play an essential role in section 5.4. However, as shown in Fig. 5.11 this model yields a narrow band at the Fermi energy which was interpreted as susceptible to a Mott-Hubbard transition.

We will now show that even an improved tight-binding model – in the sense that it accurately reproduces the LDA band structure of the normal cell – does not necessarily yield correct results for the reconstructed supercell band structure. For this purpose we extended the afore-

---

[9] Note that since the present tight-binding model contains spin-orbit coupling we compare the corresponding band structure to a full relativistic LDA calculation. In contrast, all calculations presented in section 5.4 were scalar relativistic.

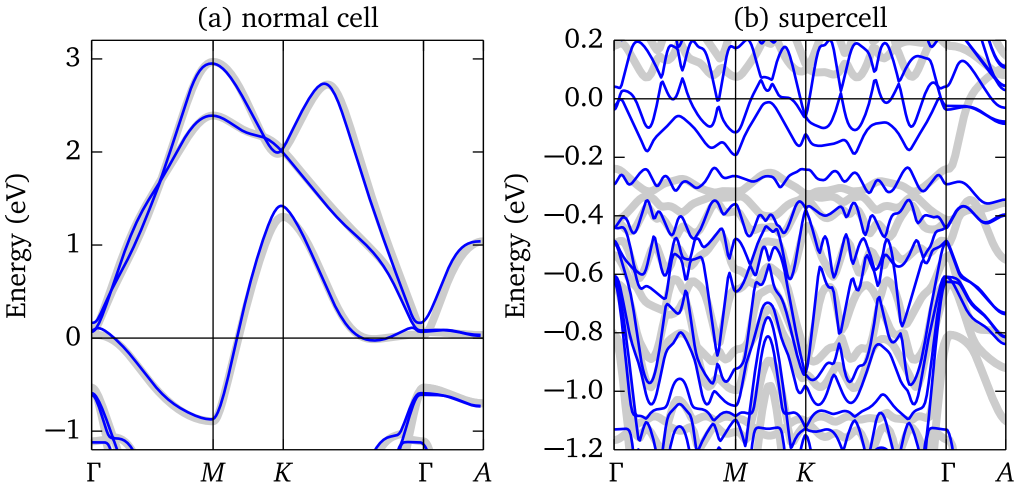

Figure 5.12: Extended 3D tight-binding model for the commensurate charge density wave phase of 1*T*-TaS$_2$. The LDA band structure (light gray) along with the tight-binding band structure (blue) is shown for the normal cell (a) and the supercell (b).

mentioned two-dimensional tight-binding model to three dimensions by including hopping integrals up to a distance of ≈ 5 normal cell lattice sites. The Sulfur p orbitals were added to the basis which results in a 143 × 143 supercell tight-binding Hamiltonian. The hopping parameters were determined by a Wannier analysis of the LDA band structure for the normal cell. In contrast to the previous model, spin-orbit coupling was not added. The scaling of the hopping parameters was performed in the same manner as for the previous model.

In Fig. 5.12 (a) it is clearly visible that this extended tight-binding model is indeed capable to reproduce the LDA band structure of the normal cell accurately. However, the derived supercell tight-binding band structure is dramatically different from the LDA supercell band structure as illustrated in Fig. 5.12 (b). While below ≈ -0.4 eV the LDA band structure and the tight-binding band structure coincide to some extent, the dispersions close to the Fermi level are completely different. In particular the strong dispersion along Γ-*A* observed in the LDA band structure does not at all occur in the tight-binding band structure. Consequently, the in-plane hybridization gap discussed in section 5.4 does not open in the tight-binding model.

These discrepancies may be attributed to the fact that the lattice modulation is intertwined with the formation of orbital textures as explained in section 5.4. As a result, the change of symmetry of the local orbitals alters the hopping parameters in a nontrivial way. The simple scaling approach based on the inter-atomic distance used in the tight-binding model can certainly not account for these complex orbital texture related effects. It is therefore in general not possible to replace the self-consistent solution of the supercell DFT problem by a tight-binding supercell approach. In particular the complex effects associated with different layer stackings as discussed in section 5.4 cannot be addressed by a simple tight-binding approach.

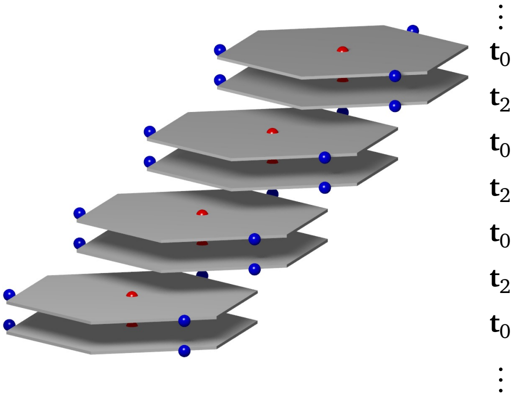

Figure 5.13: Visualization of the stacking $\langle \mathbf{t}_0\mathbf{t}_2 \rangle$. The gray hexagons indicate the $\sqrt{13}\times\sqrt{13}$-supercell. Red spheres correspond to the central Ta-site within the $\sqrt{13}\times\sqrt{13}$-supercell. Blue spheres denote the Ta-sites at $2\mathbf{a}$, $2\mathbf{b}$ and $-2(\mathbf{a}+\mathbf{b})$. The stacking is given by on-top stacked bilayers which are stacked with $\mathbf{t}_2$.

5.6 Improved stacking model and direct comparison to angle-resolved photoemission data

In section 5.4.2 it was pointed out that none of the prototypical stacking types $\langle \mathbf{t}_0 \rangle$ and $\langle \mathbf{t}_2 \rangle$ is capable to describe the experimental band structure very close to the Fermi level. We attributed this discrepancy to the fact that the actual stacking in the real material is neither given by $\langle \mathbf{t}_0 \rangle$ nor $\langle \mathbf{t}_2 \rangle$ but by a partially disordered alternation $\left\langle \mathbf{t}_0\mathbf{t}_{\{256\}} \right\rangle$ of the two (see section 4.5.2). Unfortunately, such disordered structures cannot be treated in terms of DFT since they are not periodic. However, in this section a refined DFT model which is an approximation for $\left\langle \mathbf{t}_0\mathbf{t}_{\{256\}} \right\rangle$ is presented along with an in-depth comparision to ARPES data.

5.6.1 Approximation for the disordered alternating stacking

The simplest approximation for the partially disordered alternating stacking $\left\langle \mathbf{t}_0\mathbf{t}_{\{256\}} \right\rangle$ is given by the periodic stacking $\langle \mathbf{t}_0\mathbf{t}_2 \rangle$. In other words, the partial disorder among the group of stacking vectors $\mathbf{t}_2, \mathbf{t}_5$ and $\mathbf{t}_6$ is neglected and instead a single fixed vector $\mathbf{t}_2$ is chosen. A visualization of $\langle \mathbf{t}_0\mathbf{t}_2 \rangle$ is shown in Fig. 5.13. This stacking can be viewed as on-top stacked bilayers (with stacking vector $\mathbf{t}_0$) which are for their part stacked with $\mathbf{t}_2$. The resulting supercell is again triclinic and contains 39 independent atoms as given in table 5.2.

In Fig. 5.14 the calculated band structure for $\langle \mathbf{t}_0\mathbf{t}_2 \rangle$ is presented along with the same ARPES data as shown in Fig. 5.6. Interestingly, this calculation yields a very small gap at the Fermi level. In section 5.4.3 it was pointed out that a bilayer of $1T$-TaS$_2$ stacked with $\mathbf{t}_0$ develops a band gap of ~ 0.2 eV. The result in Fig. 5.14 suggest that this gap still exists when the bilayers

spacegroup: P$\bar{1}$
lattice parameters: $a = 12.11\,\text{Å}$, $b = 12.11\,\text{Å}$, $c = 13.608\,\text{Å}$
axis angles: $\alpha = 110.016°$, $\beta = 61.366°$, $\gamma = 120°$

Wyckoff positions:

Ta	-0.115	0.038	0.25	Ta	0.172	0.254	0.25
Ta	-0.187	-0.249	0.25	Ta	-0.331	0.110	0.25
Ta	0.405	0.187	0.25	Ta	-0.487	-0.482	0.25
Ta	-0.264	0.410	0.25	S	0.000	0.110	0.387
S	-0.307	-0.119	0.387	S	-0.230	0.187	0.387
S	0.305	0.120	0.116	S	-0.310	-0.341	0.116
S	-0.156	0.274	0.116	S	0.376	0.430	0.129
S	-0.085	-0.416	0.129	S	-0.469	0.045	0.129
S	0.316	0.339	0.370	S	-0.376	-0.430	0.370
S	-0.453	0.262	0.370	S	0.608	0.352	0.126
Ta	0.403	0.177	-0.25	Ta	0.043	-0.326	-0.25
Ta	-0.100	0.033	-0.25	Ta	0.636	0.110	-0.25
Ta	-0.256	-0.559	-0.25	Ta	-0.033	0.333	-0.25
S	0.231	0.034	-0.112	S	-0.076	-0.196	-0.112
S	0.000	0.110	-0.112	S	0.535	0.043	-0.383
S	-0.079	-0.417	-0.383	S	0.074	0.197	-0.383
S	0.607	0.353	-0.370	S	0.145	-0.492	-0.370
S	-0.239	-0.031	-0.370	S	0.546	0.262	-0.129
S	-0.145	-0.507	-0.129	S	-0.222	0.185	-0.129
S	0.838	0.275	-0.373				

Table 5.2: Structural parameters of the supercell for the stacking $\langle \mathbf{t}_0\mathbf{t}_2 \rangle$.

are stacked with $\mathbf{t}_2$. In fact, the gap in Fig. 5.14 resembles the properties of a pseudogap, because it is rather a minimum in the density of states directly at the Fermi level instead of an extended band gap. It is also obvious that the present calculation describes the ARPES data better than the pure stackings $\langle \mathbf{t}_0 \rangle$ or $\langle \mathbf{t}_2 \rangle$. As already pointed out in section 5.4 the ARPES data are measured along a **k** direction which is tilted with respect to the Γ-M direction by about 10 degrees. However, the comparison to the data of Hellmann *et al.* (cf. Fig. 3.5 on page 20) reveals an even better agreement. The electron-like pocket observed at the Γ-point at about -0.2 eV is not only reproduced at the quantitatively correct position but also the form of this feature fits with the experiment. Nevertheless, this feature is strongly smeared in the ARPES data which might be attributed to the partial disorder which is neglected in the current DFT model. Furthermore, the comparison of the total energy for the different calculations reveals that the alternating stacking $\langle \mathbf{t}_0\mathbf{t}_2 \rangle$ is indeed more stable compared to the pure stackings $\langle \mathbf{t}_0 \rangle$ and $\langle \mathbf{t}_2 \rangle$. As can be seen from Tab. 5.3 the total energy for $\langle \mathbf{t}_0\mathbf{t}_2 \rangle$ is about 10 meV smaller than

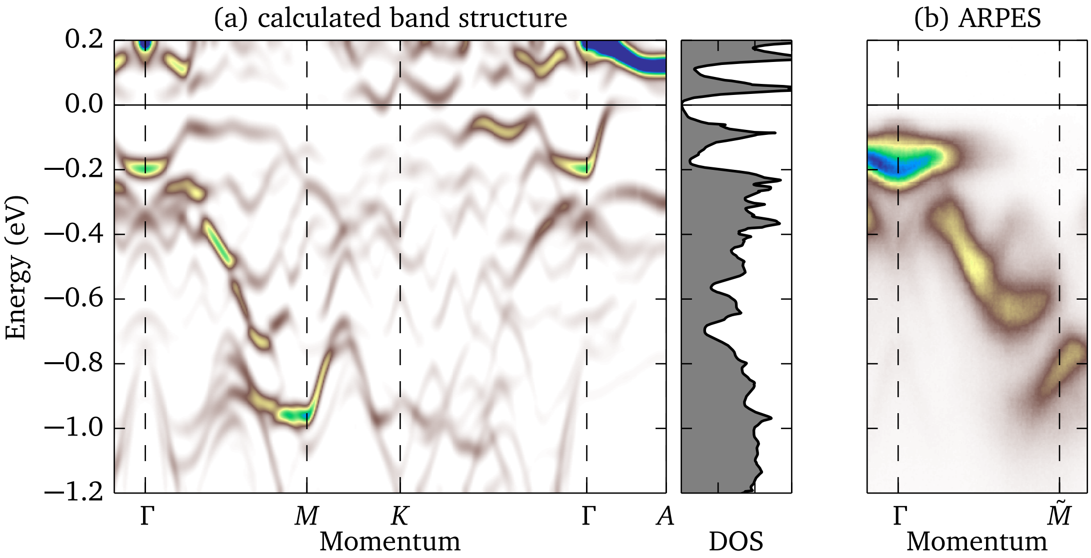

Figure 5.14: Calculated band structure for the stacking $\langle \mathbf{t}_0\mathbf{t}_2 \rangle$ along the high-symmetry directions of the Brillouin zone corresponding to the undistorted structure. ARPES data are shown for comparison.

stacking	energy relative to $\langle \mathbf{t}_0 \rangle$ (meV)	DOS at E_F (states/eV).
$\langle \mathbf{t}_0 \rangle$	0.0	5.49
$\langle \mathbf{t}_2 \rangle$	9.57	16.75
$\langle \mathbf{t}_0\mathbf{t}_2 \rangle$	-9.69	0

Table 5.3: Total energies for different stackings as calculated by LDA.

that for $\langle \mathbf{t}_0 \rangle$.

However, the total energy differences are close to the accuracy limit of DFT and the good agreement between calculation and APRES data shown in Fig. 5.14 is a case in point. For this reason we want to extent the comparison to a larger reciprocal space region. This will be done in the following section.

5.6.2 In-depth comparison to ARPES data

We have measured the valence band structure of 1T-TaS$_2$ as a function of k_x and k_y which, together with the energy axis, yields a 3D dataset[10]. Below we will compare constant-energy cuts of this dataset with corresponding calculations.

Since the three vectors $\mathbf{t}_2, \mathbf{t}_5$ and $\mathbf{t}_6$ occur randomly in the partially disordered stacking $\left\langle \mathbf{t}_0\mathbf{t}_{\{256\}} \right\rangle$ the whole structure has, on average, threefold rotational symmetry. This symmetry

---

[10] k_x, k_y and k_z refer to Cartesian coordinates in reciprocal space where the k_x-k_y-plane is identical to the ab-plane in the crystal coordinate system of the unreconstructed structure.

is broken by the approximation $\langle \mathbf{t}_0\mathbf{t}_2\rangle$, where only $\mathbf{t}_2$ occurs. For a comparison to ARPES data we have therefore symmetrized the calculated spectra for $\langle \mathbf{t}_0\mathbf{t}_2\rangle$ in order to restore the threefold symmetry:

$$I'(k_x,k_y,E) = \frac{1}{3}\Bigg[I(k_x,k_y,E) + I(-\frac{k_x}{2}+\sqrt{\frac{3}{4}}k_y, -\frac{k_y}{2}-\sqrt{\frac{3}{4}}k_y, E) + I(-\frac{k_x}{2}-\sqrt{\frac{3}{4}}k_y, -\frac{k_y}{2}+\sqrt{\frac{3}{4}}k_y, E)\Bigg], \quad (5.40)$$

where $I(k_x,k_y,E)$ denotes the unfolded band weights as explained in section 5.3. The assumption which leads to Eq. 5.40 is that, on average, the effect of the disorder in $\left\langle \mathbf{t}_0\mathbf{t}_{\{256\}}\right\rangle$ for the electronic structure can be approximated with a linear superposition of $\langle \mathbf{t}_0\mathbf{t}_2\rangle$, $\langle \mathbf{t}_0\mathbf{t}_5\rangle$ and $\langle \mathbf{t}_0\mathbf{t}_6\rangle$. However, it should be emphasized that this assumption is purely heuristic and at this point it is not clear whether this approach is valid.

In addition, it is known that measured ARPES spectra often represent an inherent k_z integration of the electronic structure [120]. In other words, the k_z value corresponding to Eq. 5.29 is not sharp but also features from somewhat different k_z values contribute to the photocurrent. This might be even more relevant for partially disordered structures like $\left\langle \mathbf{t}_0\mathbf{t}_{\{256\}}\right\rangle$ since, strictly speaking, k_z does not represent a valid quantum number in such a system anymore. In order to account for the k_z-integration we consider the linear combination:

$$I''(k_x,k_y,E) = \alpha I'_{k_z=0}(k_x,k_y,E) + (1-\alpha)I'_{k_z=0.3\cdot 2\pi/c_0}(k_x,k_y,E), \quad (5.41)$$

of the in-plane band structure at $k_z = 0$ and $k_z = 0.3\cdot 2\pi/c_0$ where $c_0 = 5.9\,\text{Å}$ is the c-axis lattice parameter of the undistorted structure. The second k_z value was intentionally chosen because this is the point along the Γ-A-direction where the band dispersion touches the Fermi level (cf. Fig. 5.13). For the mixing parameter α we chose $\alpha = 0.8$. As before, the band weights I'' have then been convoluted with a resolution function in order to simulate the measured ARPES spectra.

In Fig. 5.15 and Fig. 5.16 we compare these simulated ARPES spectra with the measured ARPES data for different energy levels E. First of all, the accordance between measurement and calculation is remarkable considering that the data are raw data. This means that the data have been solely normalized to the background. The top panel of Fig. 5.15 shows energy cuts at the Fermi level (Fermi surface maps). The weak signal observed in ARPES was previously referred to as a remnant or pseudo-gapped Fermi surface [59, 108, 110, 121]. Surprisingly, similar features occur in our LDA calculations (top left panel in Fig. 5.15). Note that the finite intensity at the Fermi level in the calculation is a result of the k_z integration (Eq. 5.41). In fact the value $k_z = 0.3 \cdot \frac{2\pi}{c_0}$ for the k_z integration has been chosen intentionally in order to reproduce these features. Accordingly, it could be argued that when the partial disorder gives rise to a pronounced k_z integration then the pseudogap features could be related to this disorder. However, the intensities of the features are not properly reproduced by the LDA calculations, which, on the one hand, might be attributed to matrix element effects (see section 5.2.2). On the other hand, this discrepancy could also indicate that the symmetrization process and the k_z integration do not properly account for the partial disorder.

Nevertheless, for energies below the Fermi level the LDA calculation agrees also very well with the corresponding measurement as can be observed in Fig. 5.15 and Fig. 5.16. The intensity distribution of the ARPES spectra below -0.6 eV shows a pronounced threefold symmetry whereas the calculations retain a sixfold symmetry. Whether this discrepancy may be again attributed to matrix element effects or whether it is related to flaws of the present LDA model remains to be clarified.

Nonetheless, the excellent overall agreement between simulated and measured ARPES data reveals that the present LDA model captures the relevant features of the C-CDW phase of 1*T*-TaS_2. However, it should be stressed again that the stacking $\langle \mathbf{t}_0\mathbf{t}_2 \rangle$ with the symmetrization and the k_z integration is still an approximation which only indirectly accounts for the partially disordered nature of the C-CDW phase. Studying the effects on the electronic structure induced by such disorder will be a challenging task for future investigations especially since tight-binding approaches are likely to fail as shown in section 5.5.

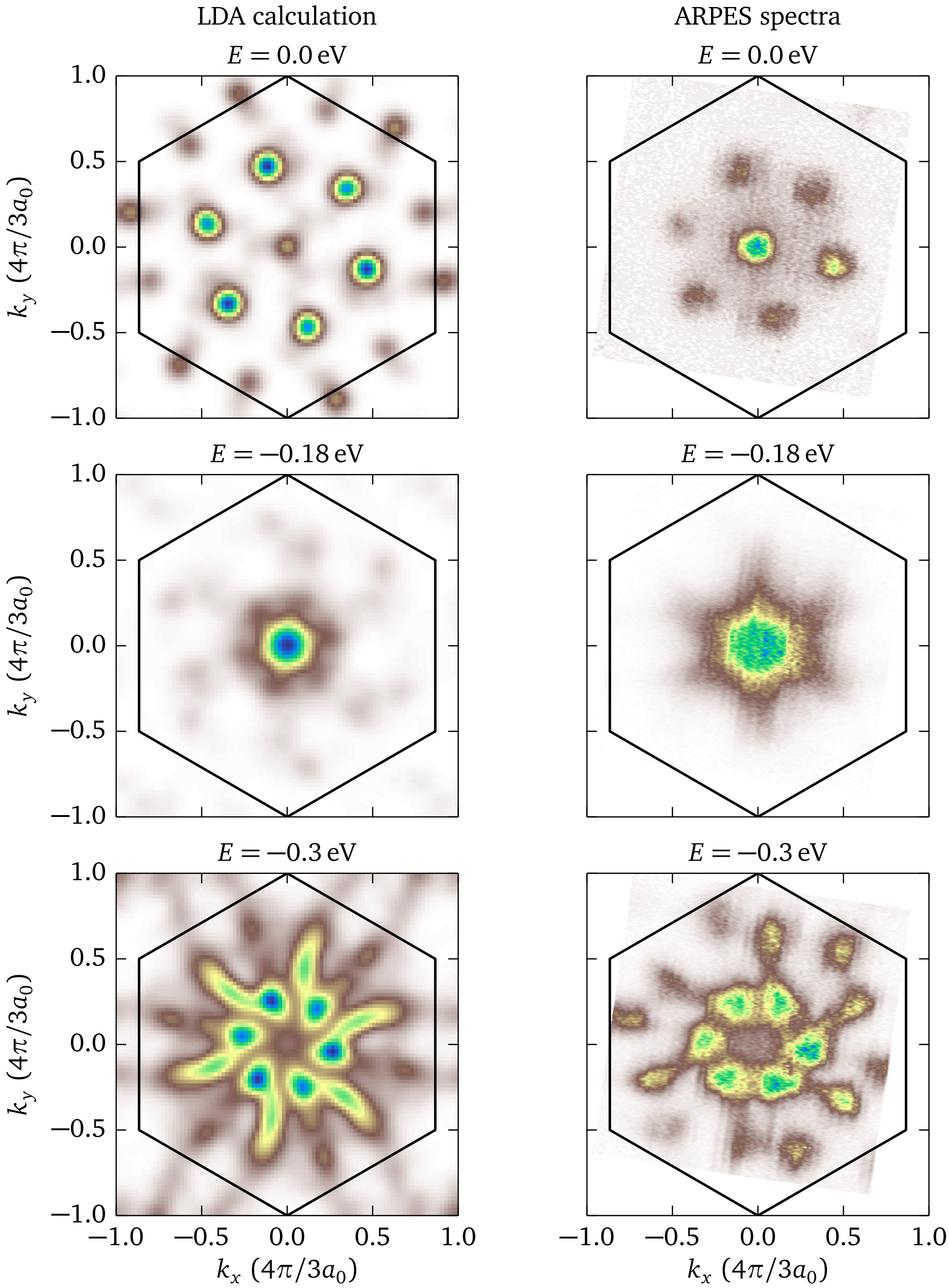

Figure 5.15: Comparison of the simulated spectral function for $\langle \mathbf{t}_0\mathbf{t}_2 \rangle$ with ARPES data within the $k_x k_y$-plane at different energies. The right panel shows the ARPES data taken at 1 K while the left panel presents the corresponding calculation. Black lines indicate the Brillouin zone boundaries. $E = 0$ eV corresponds to the Fermi level and $a_0 = 3.36$ Å is the a-axis lattice parameter of the unreconstructed structure.

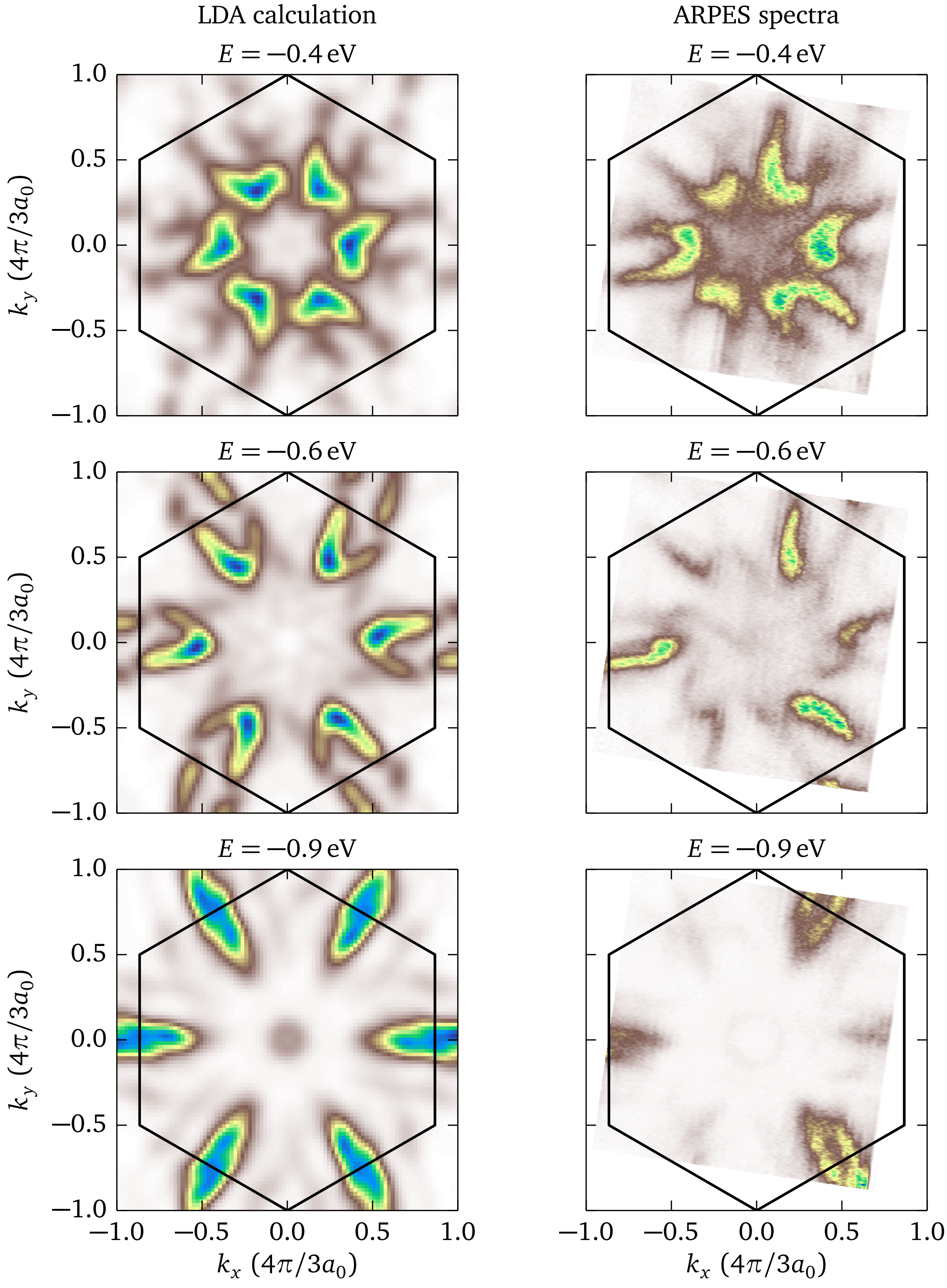

Figure 5.16: Comparison of the simulated spectral function for $\langle \mathbf{t}_0\mathbf{t}_2 \rangle$ with ARPES data within the $k_x k_y$-plane at different energies. (continued)

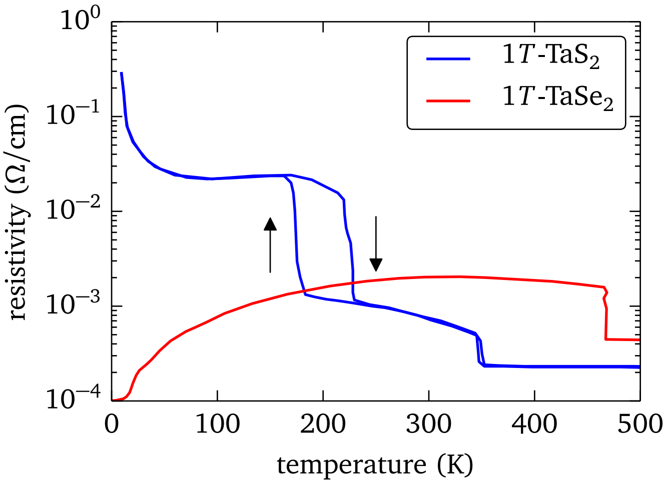

Figure 5.17: In-plane resistivity ($\rho^{\|}$) of 1*T*-TaS$_2$ and 1*T*-TaSe$_2$ as a function of temperature. Graph reproduced from references 24 and 45.

5.7 Relation to other transition metal dichalcogenides

We now compare 1*T*-TaS$_2$ to the material 1*T*-TaSe$_2$ because both compounds develop different properties despite their striking similarities. Below 473 K, the isostructural compound 1*T*-TaSe$_2$ develops the same in-plane $\sqrt{13} \times \sqrt{13}$-superstructure as 1*T*-TaS$_2$. But in contrast to the latter the C-CDW phase of 1*T*-TaSe$_2$ does not exhibit semiconducting electronic properties but behaves rather metallic as illustrated in Fig. 5.17. It has further been shown that the CDW-layer stacking of the C-CDW in 1*T*-TaSe$_2$ is given by the $\langle \mathbf{t}_2 \rangle$ polytype [54, 87, 122]. The dramatic effect of the CDW-layer stacking revealed in section 5.4 consequently suggests that the difference in the transport properties may be related to the different stacking orders in the two materials.

We looked into the relevance of the CDW-layer stacking in 1*T*-TaSe$_2$ by calculating the electronic structure for the stacking $\langle \mathbf{t}_2 \rangle$ which occurs in the real material and the hypothetical on-top stacking $\langle \mathbf{t}_0 \rangle$. In Fig. 5.18 one can clearly observe that for $\langle \mathbf{t}_2 \rangle$ significant Fermi level crossings occur within the Γ-M-K-plane and in the out-of-plane direction Γ-A – very similar to the case of 1*T*-TaS$_2$ (compare Fig. 5.6 (d) on page 75). For the on-top stacking $\langle \mathbf{t}_0 \rangle$ an in-plane hybridization gap opens in line with the results presented for 1*T*-TaS$_2$ in Fig. 5.6 (e). As can be seen in Tab. 5.3 the density of states at E_F for 1*T*-TaS$_2$ with $\langle \mathbf{t}_0 \mathbf{t}_2 \rangle$ is zero, which suggests rather semiconducting transport properties. In contrast, the density of states at E_F for 1*T*-TaSe$_2$ with $\langle \mathbf{t}_2 \rangle$ is about 11 states/eV giving rise to metallic behavior.

It is likewise worth noting that also in 1*T*-TaSe$_2$ the CDW is accompanied by the formation of an orbital texture analogous to 1*T*-TaS$_2$ which is shown in Fig. 5.7 on page 76. In Fig. 5.19 we show these orbital textures for $\langle \mathbf{t}_2 \rangle$ and the hypothetical stacking $\langle \mathbf{t}_0 \rangle$. It turns out that

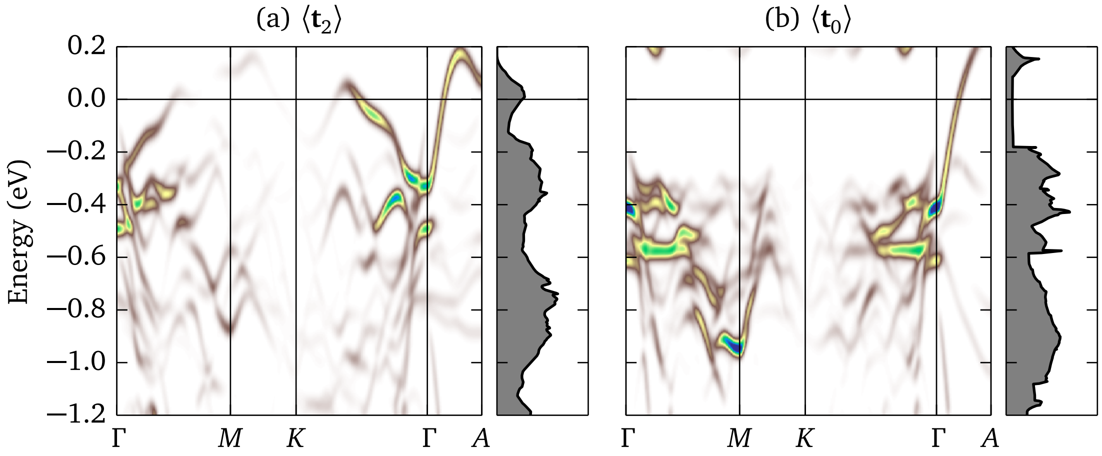

Figure 5.18: Unfolded LDA band structure of $1T$-TaSe$_2$ for the experimentally found stacking $\langle \mathbf{t}_2 \rangle$ (a) and the hypothetical on-top stacking $\langle \mathbf{t}_0 \rangle$ (b).

for the case of $1T$-TaSe$_2$ it is not straightforward to define an energy window for the highest occupied band since they are not as well separated as it is the case of $1T$-TaS$_2$. However, the resulting orbital structure is similar to the one found in $1T$-TaS$_2$ (cf. Fig. 5.7 and Fig. 5.19). Note that the orbital textures shown in Fig. 5.19 (c) and (d) do not have threefold symmetry. This is due to the fact that the crystal structure refinement, on which the present calculations are based, was done in $\mathrm{P}\bar{1}$ symmetry [122]. Accordingly, the atomic positions differ slightly from the positions which would correspond to an in-plane threefold symmetry.

We now turn the discussion towards the difference between $1T$-TaS$_2$ and $1T$-TaSe$_2$ which could lead to the stabilization of the respective stackings in these materials. The orbital texture which arises from the $\sqrt{13} \times \sqrt{13}$ superstructure leads to the formation of charge clouds centered on the $\sqrt{13} \times \sqrt{13}$ clusters (see Fig. 5.7 (e) and (f)). This is plausible because the superstructure causes a breathing-type distortion of the chalcogenide sites as illustrated in Fig. 5.4 on page 72. On the one hand the Coulomb interaction between these charge clouds favors a sphere packing which is best realized by the stacking $\langle \mathbf{t}_2 \rangle$ and its symmetry equivalents. On the other hand the in-plane hybridization gap and, hence, some energy gain is maximized by $\langle \mathbf{t}_0 \rangle$. The long-range Coulomb interaction couples distant layers (not only nearest neighbor layers) which gives rise to more complex stackings like $\left\langle \mathbf{t}_0 \mathbf{t}_{\{256\}} \right\rangle$ [85]. Accordingly, one could argue that the CDW layer stacking is widely governed by a subtle balance between Coulomb interactions and hybridization effects.

The present study indicates that the balance between these mechanisms is evidently different for the two materials $1T$-TaSe$_2$ and $1T$-TaS$_2$. This discrepancy could be related to the atomic radii of the chalcogenide atoms. The larger Selenium atoms are more susceptible to polarization effects than the smaller Sulfur atoms which could effect the inter-layer Coulomb

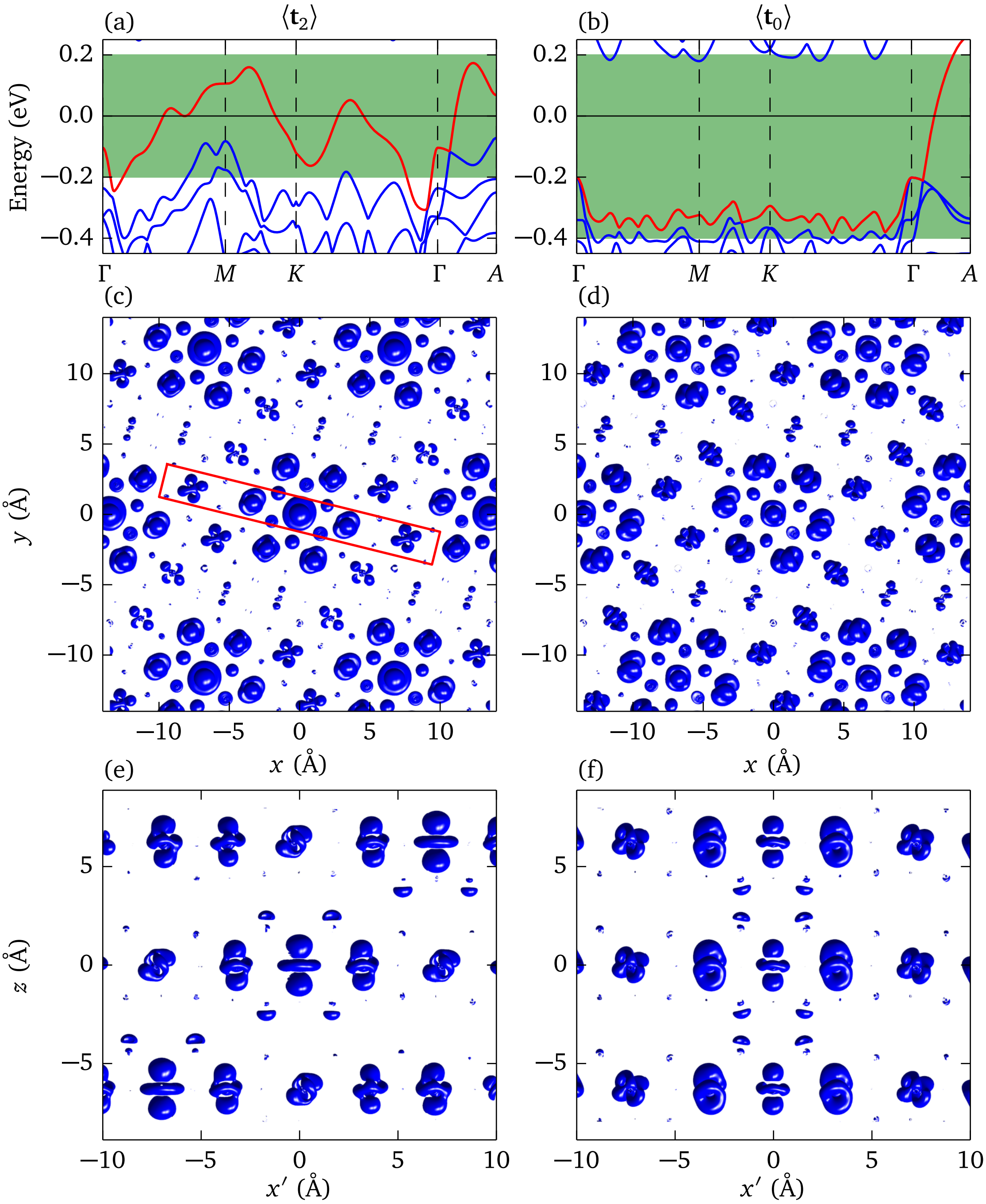

Figure 5.19: Real space illustration of the orbital texture in 1*T*-TaSe$_2$ for $\langle \mathbf{t}_2 \rangle$ (left) and the hypothetical stacking $\langle \mathbf{t}_0 \rangle$ (right). As in Fig. 5.7 on page 76 (a) and (b) show the band structure near E_F with the highest occupied band in red. The energy windows used to calculate the energy-resolved electron density shown in (c) - (f) is highlighted in green. (c) and (f): Similar to 1*T*-TaS$_2$ a complex orbital texture emerges within the *ab*-plane of 1*T*-TaSe$_2$. (e) and (f): Views of the *ac*-plane corresponding to the area indicated with the red rectangle in (c).

interaction. In addition, the valence states of Selenium are more extended than in the case of Sulfur, which should lead to stronger hybridization effects and, hence, larger band widths as can indeed be observed in Fig. 5.18. At this point it should be noted that within DFT the stacking $\langle \mathbf{t}_2 \rangle$ is energetically more favorable than $\langle \mathbf{t}_0 \rangle$ for $1T$-TaSe$_2$. The calculated total energy per unit cell for $\langle \mathbf{t}_2 \rangle$ is about 40 meV lower than for $\langle \mathbf{t}_0 \rangle$. However, so far it is not clear which mechanisms are crucial for the realization of the different stacking orders found in $1T$-TaS$_2$ and $1T$-TaSe$_2$ and we leave the thorough examination of this issue for future work.

In summary, it seems very likely that the semiconducting properties of the C-CDW in $1T$-TaS$_2$ is a direct result of the CDW-layer stacking rather than related to Mott-type electron-electron correlations. The absence of semiconducting properties in isostructural materials sharing the same $\sqrt{13} \times \sqrt{13}$ superstructure is, hence, rooted in the realization of different stacking orders.

The manipulation of the balance between inter-layer Coulomb interaction and inter-layer hybridization – for instance by intercalation experiments – may provide interesting routes to tune the electronic properties of these layered materials. In addition, such experiments could also shed light on the mechanisms which stabilize the different stacking orders.

6 Summary and Outlook

In this thesis the layered transition metal dichalcogenide $1T$-TaS$_2$ has been comprehensively studied by means of experimental and theoretical methods. State-of-the-art X-ray diffraction was used to shed light on the charge density wave structure as a function of pressure and temperature. This microscopic structural information supplemented with angle-resolved photoemission spectroscopy data was then used to develop realistic density functional theory models which describe the electronic structure of $1T$-TaS$_2$ in the presence of charge density waves. The following paragraphs briefly summarize the key results of these two subtopics along with their implications.

After the brief review of some theoretical aspects of charge density wave physics and an introduction into the material class of layered transition metal dichalcogenides the discussion was turned to the static charge density wave structure of $1T$-TaS$_2$ as a function of pressure and temperature. The detailed analysis of the temperature- and pressure-dependent X-ray diffraction data in chapter 4 revealed three key results:

The first major result was that the defect lattice which characterizes the nearly commensurate charge density wave in $1T$-TaS$_2$ essentially shrinks with increasing pressure. Accordingly, it was concluded that the whole nearly commensurate charge density wave structure becomes superconducting, i. e. forms a coherent macroscopic superconducting state. This situation is fundamentally different from a previously suggested real space phase separation scenario in which only the defects support superconductivity.

Secondly, it was found that several distinct incommensurate charge density waves emerge at high pressure which share the same characteristics of the presence of defect lattices as the nearly commensurate charge density wave. Consequently, it was concluded that such defect lattices might also play a crucial role for these incommensurate charge density waves. The notion that the phase transitions between the different incommensurate phases in $1T$-TaS$_2$ may be related to structural phase transitions of the defect lattices certainly poses an exciting possibility which deserves further investigations in future work.

Thirdly, the charge density wave layer stacking of the commensurate charge density wave was also investigated by comparing the X-ray diffraction data to numerical simulations. This analysis extended previous approaches and established the presence of a partially disordered charge density wave layer stacking within the commensurate charge density wave of $1T$-TaS$_2$.

Such a state of matter is particularly interesting because the disorder only effects the charge density wave and not the average crystal structure. Thus, it can be regarded as a disorder in an electronic crystal which furthermore occurs only along one direction. This unconventional property was discussed with respect to the pseudogap observed in $1T$-TaS_2.

In chapter 5 the discussion was turned to the examination of the electronic structure of $1T$-TaS_2 by means of density functional theory complemented with angle-resolved photoemission spectroscopy. Previous density functional theory studies usually neglected the 3D character of the charge density wave in $1T$-TaS_2. Triggered by the X-ray diffraction analysis which revealed the important role of the interlayer correlations, the influence of different charge density wave layer stackings was considered in density functional theory model calculations which led to the following key results:

The first key result was the discovery of a complex orbital texture which is interwoven with the charge density wave. Moreover, it turned out that due to this orbital texture the charge density wave layer stacking has dramatic effects on the electronic structure. Apparently, all these orbital-related effects are well beyond traditional weak coupling charge density wave physics. Indeed it was shown that the orbital-mediated interactions may enable one to drive semiconductor-to-metal transitions with technologically pertinent gaps and on ultrafast timescales in bilayer systems of $1T$-TaS_2. This opens up new routes to fabricate optically switchable devices based on orbitally textured charge density wave compounds, a new technology that could be called “orbitronics”. These discoveries are hence of special relevance for the ongoing development of novel, miniaturized and ultrafast devices for electronic and sensing applications.

Secondly, the discovery of orbital textures allows to explain a number of long-standing puzzles associated with the electronic self-organization in $1T$-TaS_2: The strong pressure dependence of the charge density wave and the ultrafast response to optical excitations can be directly related to the orbital texture. By means of an improved stacking model for the commensurate charge density wave it was further shown that the semiconducting properties of this phase are related rather to its particular stacking order than to Mott-Hubbard type electron correlations. This also explains the absence of a semiconducting phase in other systems which share the same in-plane charge density wave structure but exhibit a different charge density wave layer stacking. A detailed comparison to angle-resolved photoemission spectroscopy further validated our approach and showed that it is capable to capture the essential features of the commensurate charge density wave in $1T$-TaS_2.

As a result, this thesis gave important new insights into the physics of layered transition metal dichalcogenides. However, it also raises a number of important questions. Most importantly the optically driven semiconductor-to-metal transition needs to be further scrutinized experimentally. To this end we plan to conduct X-ray diffraction experiments in combination with ultrafast optical excitation. The numerical structure factor analysis for the charge density wave layer stacking derived in this thesis will allow for the identification of crucial optically induced changes. Furthermore, it will be exciting to study the effects of manipulating the partially disordered stacking of the commensurate charge density wave in $1T$-TaS$_2$ for instance by intercalation experiments. In order to elucidate whether similar disordered charge density wave states may be induced in related materials we will also extend these investigations to other layered transition metal dichalcogenides. Another issue which deserves thorough examination is the role of the defect lattices observed in the incommensurate charge density waves. It is known that many other transition metal dichalcogenides also exhibit incommensurate phases, hence the quest for similar defect lattice effects appears promising. Even experiments which target the dynamics of such defect lattices are conceivable. In conclusion, it becomes evident that – despite its simple composition and host structure – $1T$-TaS$_2$ features extremely rich physics and is certainly more than just a model system. Most notably, the emerging possibilities for device applications not only for $1T$-TaS$_2$ but for the whole material class of layered transition metal dichalcogenides will assuredly attract increasing attention in the near future.

Eventually, this study has proven that – once again – Aristotle was right: All the fascinating self-organized phenomena which can be observed in materials such as $1T$-TaS$_2$ emerge from the very interaction between rather simple constituents like electrons and nuclei so that, indeed, *the whole is more than the sum of its parts*.

Bibliography

[1] V. Hinkov, D. Haug, B. Fauqué, P. Bourges, Y. Sidis, A. Ivanov, C. Bernhard, C. T. Lin and B. Keimer, “Electronic liquid crystal state in the high-temperature superconductor $\mathrm{YBa_2Cu_3O_{6.45}}$”, Science **319**, 597–600 (2008).

[2] M. v. Zimmermann, A. Vigliante, T. Niemöller, N. Ichikawa, T. Frello, J. Madsen, P. Wochner, S. Uchida, N. H. Andersen, J. M. Tranquada, D. Gibbs and J. R. Schneider, “Hard-x-ray diffraction study of charge stripe order in $\mathrm{La_{1.48}Nd_{0.4}Sr_{0.12}CuO_4}$”, EPL (Europhysics Letters) **41**, 629 (1998).

[3] G. Ghiringhelli, M. Le Tacon, M. Minola, S. Blanco-Canosa, C. Mazzoli, N. B. Brookes, G. M. De Luca, A. Frano, D. G. Hawthorn, F. He, T. Loew, M. M. Sala, D. C. Peets, M. Salluzzo, E. Schierle, R. Sutarto, G. A. Sawatzky, E. Weschke, B. Keimer and L. Braicovich, “Long-range incommensurate charge fluctuations in $\mathrm{(Y,Nd)Ba_2Cu_3O_{6+x}}$”, Science **337**, 821–825 (2012).

[4] J. Chang, E. Blackburn, A. T. Holmes, N. B. Christensen, J. Larsen, J. Mesot, R. Liang, D. A. Bonn, W. N. Hardy, A. Watenphul, M. v. Zimmermann, E. M. Forgan and S. M. Hayden, “Direct observation of competition between superconductivity and charge density wave order in $\mathrm{YBa_2Cu_3O_{6.67}}$”, Nat Phys **8**, 871–876 (2012).

[5] Y. Zhang, J. Wei, H. W. Ou, J. F. Zhao, B. Zhou, F. Chen, M. Xu, C. He, G. Wu, H. Chen, M. Arita, K. Shimada, H. Namatame, M. Taniguchi, X. H. Chen and D. L. Feng, “Unusual doping dependence of the electronic structure and coexistence of spin-density-wave and superconductor phases in single crystalline $\mathrm{Sr_{1-x}K_xFe_2As_2}$”, Phys. Rev. Lett. **102**, 127003 (2009).

[6] C. de la Cruz, Q. Huang, J. W. Lynn, J. Li, W. R. II, J. L. Zarestky, H. A. Mook, G. F. Chen, J. L. Luo, N. L. Wang and P. Dai, “Magnetic order close to superconductivity in the iron-based layered $\mathrm{LaO_{1-x}F_xFeAs}$ systems”, Nature **453**, 899–902 (2008).

[7] P. Gegenwart, Q. Si and F. Steglich, “Quantum criticality in heavy-fermion metals”, Nat Phys **4**, 186–197 (2008).

[8] A. M. Gabovich, A. I. Voitenko and M. Ausloos, “Charge- and spin-density waves in existing superconductors: competition between cooper pairing and peierls or excitonic instabilities”, Phys. Rep. **367**, 583–709 (2002).

[9] C. Du, W. Lin, Y. Su, B. Tanner, P. Hatton, D. Casa, B. Keimer, J. Hill, C. Oglesby and H. Hohl, “X-ray scattering studies of $2H$-NbSe$_2$, a superconductor and charge density wave material, under high external magnetic fields”, J. Phys.: Condens. Matter **12**, 5361 (2000).

[10] Y. Zhang, Y.-W. Tan, H. L. Stormer and P. Kim, “Experimental observation of the quantum hall effect and berry’s phase in graphene”, Nature **438**, 201–204 (2005).

[11] A. Ohtomo and H. Y. Hwang, “A high-mobility electron gas at the LaAlO$_3$/SrTiO$_3$ heterointerface”, Nature **427**, 423–426 (2004).

[12] A. Ayari, E. Cobas, O. Ogundadegbe and M. S. Fuhrer, “Realization and electrical characterization of ultrathin crystals of layered transition-metal dichalcogenides”, Journal of Applied Physics **101**, 014507, (2007).

[13] B. Radisavljevic, A. Radenovic, J. Brivio, V. Giacometti and A. Kis, “Single-layer MoS$_2$ transistors”, Nat Nano **6**, 147–150 (2011).

[14] Q. H. Wang, K. Kalantar-Zadeh, A. Kis, J. N. Coleman and M. S. Strano, “Electronics and optoelectronics of two-dimensional transition metal dichalcogenides”, Nature nanotechnology **7**, 699–712 (2012).

[15] M. Chhowalla, H. S. Shin, G. Eda, L.-J. Li, K. P. Loh and H. Zhang, “The chemistry of two-dimensional layered transition metal dichalcogenide nanosheets”, Nature chemistry **5**, 263–275 (2013).

[16] D. Jariwala, V. K. Sangwan, L. J. Lauhon, T. J. Marks and M. C. Hersam, “Emerging device applications for semiconducting two-dimensional transition metal dichalcogenides”, ACS Nano **8**, 1102–1120 (2014).

[17] Y. Yu, F. Yang, X. F. Lu, Y. J. Yan, ChoYong-Heum, L. Ma, X. Niu, S. Kim, Y.-W. Son, D. Feng, S. Li, S.-W. Cheong, X. H. Chen and Y. Zhang, “Gate-tunable phase transitions in thin flakes of $1T$-TaS$_2$”, Nat Nano **10**, 270–276 (2015).

[18] S. Mühlbauer, B. Binz, F. Jonietz, C. Pfleiderer, A. Rosch, A. Neubauer, R. Georgii and P. Böni, “Skyrmion lattice in a chiral magnet”, Science **323**, 915–919 (2009).

[19] G. Grüner, *Density waves in solids*, Vol. 89 (Addison-Wesley Reading, MA, 1994).

[20] H. Fröhlich, “On the theory of superconductivity: the one-dimensional case”, Proceedings of the Royal Society of London. Series A. Mathematical and Physical Sciences **223**, 296–305 (1954).

[21] R. E. Peierls, *Quantum theory of solids* (Clarendon, 1955).

[22] L. Coleman, M. Cohen, D. Sandman, F. Yamagishi, A. Garito and A. Heeger, "Superconducting fluctuations and the peierls instability in an organic solid", Solid State Communications **12**, 1125–1132 (1973).

[23] P. Anderson, P. Lee and M. Saitoh, "Remarks on giant conductivity in TTF-TCNQ", Solid State Communications **13**, 595–598 (1973).

[24] J. Wilson, F. Di Salvo and S. Mahajan, "Charge-density waves and superlattices in the metallic layered transition metal dichalcogenides", Advances in Physics **24**, 117–201 (1975).

[25] J. Bednorz and K. Müller, "Possible high T_c superconductivity in the Ba-La-Cu-O system", English, Zeitschrift für Physik B Condensed Matter **64**, 189–193 (1986).

[26] M. Le Tacon, A. Bosak, S. M. Souliou, G. Dellea, T. Loew, R. Heid, K.-P. Bohnen, G. Ghiringhelli, M. Krisch and B. Keimer, "Inelastic x-ray scattering in $YBa_2Cu_3O_{6.6}$ reveals giant phonon anomalies and elastic central peak due to charge-density-wave formation", Nat Phys **10**, 52–58 (2014).

[27] E. H. da Silva Neto, P. Aynajian, A. Frano, R. Comin, E. Schierle, E. Weschke, A. Gyenis, J. Wen, J. Schneeloch, Z. Xu, S. Ono, G. Gu, M. Le Tacon and A. Yazdani, "Ubiquitous interplay between charge ordering and high-temperature superconductivity in cuprates", Science **343**, 393–396 (2014).

[28] K. Rossnagel, "On the origin of charge-density waves in select layered transition-metal dichalcogenides", J. Phys.: Condens. Matter **23**, 213001 (2011).

[29] S. Chan and V. Heine, "Spin density wave and soft phonon mode from nesting fermi surfaces", J. Phys. F **3**, 795–809 (1973).

[30] M. D. Johannes and I. I. Mazin, "Fermi surface nesting and the origin of charge density waves in metals", Phys. Rev. B **77**, 165135, 165135 (2008).

[31] G. Grüner, "The dynamics of spin-density waves", Rev. Mod. Phys. **66**, 1–24 (1994).

[32] M. D. Johannes, I. I. Mazin and C. A. Howells, "Fermi-surface nesting and the origin of the charge-density wave in $NbSe_2$", Phys. Rev. B **73**, 205102, 205102 (2006).

[33] J. Bardeen, L. N. Cooper and J. R. Schrieffer, "Theory of superconductivity", Phys. Rev. **108**, 1175–1204 (1957).

[34] J. Sólyom, "The fermi gas model of one-dimensional conductors", Advances in Physics **28**, 201–303 (1979).

[35] D. Jérome, T. M. Rice and W. Kohn, "Excitonic insulator", Phys. Rev. **158**, 462–475 (1967).

[36] S. Hellmann, T. Rohwer, M. Kalläne, K. Hanff, C. Sohrt, A. Stange, A. Carr, M. Murnane, H. Kapteyn, L. Kipp, M. Bauer and K. Rossnagel, "Time-domain classification of charge-density-wave insulators", Nat Commun **3**, 1069– (2012).

[37] J. van Wezel, "Chirality and orbital order in charge density waves", EPL (Europhysics Letters) **96**, 67011 (2011).

[38] G. Grüner, "The dynamics of charge-density waves", Rev. Mod. Phys. **60**, 1129–1181 (1988).

[39] P. Bak and V. L. Pokrovsky, "Theory of metal-insulator transition in peierls systems with nearly half-filled bands", Phys. Rev. Lett. **47**, 958–961 (1981).

[40] H. Ehrenreich and D. Turnbull, *Solid state physics*, Bd. 41 (Elsevier Science, 1988).

[41] W. L. McMillan, "Theory of discommensurations and the commensurate-incommensurate charge-density-wave phase transition", Phys. Rev. B **14**, 1496–1502 (1976).

[42] J. A. Wilson and A. D. Yoffe, "The transition metal dichalcogenides discussion and interpretation of the observed optical, electrical and structural properties", Adv. Phys. **18**, 193–335 (1969).

[43] R. H. Friend and A. D. Yoffe, "Electronic properties of intercalation complexes of the transition metal dichalcogenides", Adv. Phys. **36**, 1–94 (1987).

[44] A. H. Castro Neto, "Charge density wave, superconductivity, and anomalous metallic behavior in 2D transition metal dichalcogenides", Phys. Rev. Lett. **86**, 4382–4385 (2001).

[45] B. Sipos, A. F. Kusmartseva, A. Akrap, H. Berger, L. Forro and E. Tutis, "From mott state to superconductivity in $1T$-TaS_2", Nat Mater **7**, 960–965 (2008).

[46] E. Morosan, H. W. Zandbergen, B. S. Dennis, J. W. G. Bos, Y. Onose, T. Klimczuk, A. P. Ramirez, N. P. Ong and R. J. Cava, "Superconductivity in cuxtise2", Nat Phys **2**, 544–550 (2006).

[47] T. Kiss, T. Yokoya, A. Chainani, S. Shin, T. Hanaguri, M. Nohara and H. Takagi, "Charge-order-maximized momentum-dependent superconductivity", Nat Phys **3**, 720–725 (2007).

[48] R. Ang, Y. Tanaka, E. Ieki, K. Nakayama, T. Sato, L. J. Li, W. J. Lu, Y. P. Sun and T. Takahashi, "Real-space coexistence of the melted mott state and superconductivity in fe-substituted $1T$-TaS_2", Phys. Rev. Lett. **109**, 176403 (2012).

[49] Y. I. Joe, X. M. Chen, P. Ghaemi, K. D. Finkelstein, G. A. de la Pena, Y. Gan, J. C. T. Lee, S. Yuan, J. Geck, G. J. MacDougall, T. C. Chiang, S. L. Cooper, E. Fradkin and P. Abbamonte, "Emergence of charge density wave domain walls above the superconducting dome in $1T$-$TiSe_2$", Nat Phys **10**, 421–425 (2014).

[50] H. Cercellier, C. Monney, F. Clerc, C. Battaglia, L. Despont, M. G. Garnier, H. Beck, P. Aebi, L. Patthey, H. Berger and L. Forró, “Evidence for an excitonic insulator phase in $1T$-TiSe$_2$”, Phys. Rev. Lett. **99**, 146403, 146403 (2007).

[51] J. Ishioka, Y. H. Liu, K. Shimatake, T. Kurosawa, K. Ichimura, Y. Toda, M. Oda and S. Tanda, “Chiral charge-density waves”, Phys. Rev. Lett. **105**, 176401 (2010).

[52] J. N. Coleman, M. Lotya, A. O’Neill, S. D. Bergin, P. J. King, U. Khan, K. Young, A. Gaucher, S. De, R. J. Smith, I. V. Shvets, S. K. Arora, G. Stanton, H.-Y. Kim, K. Lee, G. T. Kim, G. S. Duesberg, T. Hallam, J. J. Boland, J. J. Wang, J. F. Donegan, J. C. Grunlan, G. Moriarty, A. Shmeliov, R. J. Nicholls, J. M. Perkins, E. M. Grieveson, K. Theuwissen, D. W. McComb, P. D. Nellist and V. Nicolosi, “Two-dimensional nanosheets produced by liquid exfoliation of layered materials”, Science **331**, 568–571 (2011).

[53] T. Tani, T. Osada and S. Tanaka, “The pressure effect on the CDw-transition temperatures in $1T$-TaS$_2$”, Solid State Communications **22**, 269–272 (1977).

[54] R. Brouwer and F. Jellinek, “The low-temperature superstructures of $1T$-TaSe$_2$ and $2H$-TaSe$_2$”, Physica B+C **99**, 51–55 (1980).

[55] A. Spijkerman, J. L. de Boer, A. Meetsma, G. A. Wiegers and S. van Smaalen, “X-ray crystal-structure refinement of the nearly commensurate phase of $1T$-TaS$_2$ in $(3+2)$-dimensional superspace”, Phys. Rev. B **56**, 13757–13767 (1997).

[56] P. Fazekas and E. Tosatti, “Electrical, structural and magnetic properties of pure and doped $1T$-TaS$_2$”, Philos. Mag. B **39**, 229–244 (1979).

[57] K. Rossnagel, “Suppression and emergence of charge-density waves at the surfaces of layered $1T$-TiSe$_2$ and $1T$-TaS$_2$ by in situ Rb deposition”, New Journal of Physics **12**, 125018 (2010).

[58] B. Dardel, M. Grioni, D. Malterre, P. Weibel, Y. Baer and F. Lévy, “Spectroscopic signatures of phase transitions in a charge-density-wave system: $1T$-TaS$_2$”, Phys. Rev. B **46**, 7407–7412 (1992).

[59] B. Dardel, M. Grioni, D. Malterre, P. Weibel, Y. Baer and F. Levy, “Temperature-dependent pseudogap and electron localization in $1T$-TaS$_2$”, Phys. Rev. B. **45**, 1462 (1992).

[60] L. Perfetti, P. A. Loukakos, M. Lisowski, U. Bovensiepen, H. Berger, S. Biermann, P. S. Cornaglia, A. Georges and M. Wolf, “Time evolution of the electronic structure of $1T$-TaS$_2$ through the insulator-metal transition”, Phys. Rev. Lett. **97**, 067402, 067402 (2006).

[61] S. Hellmann, M. Beye, C. Sohrt, T. Rohwer, F. Sorgenfrei, H. Redlin, M. Kalläne, M. Marczynski-Bühlow, F. Hennies, M. Bauer, A. Föhlisch, L. Kipp, W. Wurth and K. Rossnagel, “Ultrafast melting of a charge-density wave in the mott insulator $1T$-TaS$_2$”, Phys. Rev. Lett. **105**, 187401 (2010).

[62] J. C. Petersen, S. Kaiser, N. Dean, A. Simoncig, H. Y. Liu, A. L. Cavalieri, C. Cacho, I. C. E. Turcu, E. Springate, F. Frassetto, L. Poletto, S. S. Dhesi, H. Berger and A. Cavalleri, “Clocking the melting transition of charge and lattice order in $1T$-TaS$_2$ with ultrafast extreme-ultraviolet angle-resolved photoemission spectroscopy”, Phys. Rev. Lett. **107**, 177402 (2011).

[63] L. Stojchevska, I. Vaskivskyi, T. Mertelj, P. Kusar, D. Svetin, S. Brazovskii and D. Mihailovic, “Ultrafast switching to a stable hidden quantum state in an electronic crystal”, Science **344**, 177–180 (2014).

[64] H. Ohta, T. Takase, Y. Komiya, H. Miyamoto, S. mishima, T. okada and K. nomura, “Direct observation of the discommensuration in the nearly commensurate charge-density wave phase in $1T$-TaS$_2$ by scanning tunneling microscopy”, physica status solidi b-basic research **169**, 313–322 (1992).

[65] X. L. Wu and C. M. Lieber, “Hexagonal domain-like charge density wave phase of $1T$-TaS$_2$ determined by scanning tunneling microscopy”, Science **243**, 4899 (1989).

[66] R. E. Thomson, B. Burk, A. Zettl and J. Clarke, “Scanning tunneling microscopy of the charge-density-wave structure in $1T$-TaS$_2$”, Phys. Rev. B **49**, 16899–16916 (1994).

[67] Als-Nielsen, *Elements of modern x-ray physics* (Wiley, 2001).

[68] A. W. Overhauser, “Observability of charge-density waves by neutron diffraction”, Phys. Rev. B **3**, 3173–3182 (1971).

[69] J. D. Axe, “Debye-waller factors for incommensurate structures”, Phys. Rev. B **21**, 4181–4190 (1980).

[70] P. M. de Wolff, “The pseudo-symmetry of modulated crystal structures”, Acta Crystallographica Section A **30**, 777–785 (1974).

[71] S. van Smaalen, “The peierls transition in low-dimensional electronic crystals”, Acta Crystallographica Section A **61**, 51–61 (2005).

[72] F. Zwick, H. Berger, I. Vobornik, G. Margaritondo, L. Forró, C. Beeli, M. Onellion, G. Panaccione, A. Taleb-Ibrahimi and M. Grioni, “Spectral consequences of broken phase coherence in $1T$-TaS$_2$”, Phys. Rev. Lett. **81**, 1058–1061 (1998).

[73] O. D. /. T. U. L. Y. England, *Crysalispro*.

[74] R. A. Forman, G. J. Piermarini, J. D. Barnett and S. Block, "Pressure measurement made by the utilization of ruby sharp-line luminescence", Science **176**, 284–285 (1972).

[75] G. J. Piermarini, S. Block, J. D. Barnett and R. A. Forman, "Calibration of the pressure dependence of the R_1 ruby fluorescence line to 195 kbar", Journal of Applied Physics **46**, 2774–2780 (1975).

[76] U. Rütt, H.-B. Neumann, H. F. Poulsen and J. R. Schneider, "The resolution function of a triple-crystal diffractometer for high-energy synchrotron radiation. ii. dispersive laue geometry", Journal of Applied Crystallography **28**, 729–737 (1995).

[77] M. v. Zimmermann, R. Nowak, G. D. Gu, C. Mennerich, H.-H. Klauss and M. Hucker, "A clamp-type pressure cell for high energy x-ray diffraction", Review of Scientific Instruments **79**, 033906, 033906 (2008).

[78] S. Ravy, C. Laulhé, J.-P. Itié, P. Fertey, B. Corraze, S. Salmon and L. Cario, "High-pressure x-ray diffraction study of $1T$-TaS_2", Physica B: Condensed Matter **407**, 1704–1706 (2012).

[79] W. L. McMillan, "Landau theory of charge-density waves in transition-metal dichalcogenides", Phys. Rev. B **12**, 1187–1196 (1975).

[80] K. Nakanishi, H. Takatera, Y. Yamada and H. Shiba, "The nearly commensurate phase and effect of harmonics on the successive phase transition in $1T$-TaS_2", Journal of the Physical Society of Japan **43**, 1509–1517 (1977).

[81] F. D. Murnaghan, "The compressibility of media under extreme pressures", Proceedings of the National Academy of Sciences of the United States of America **30**, 244–247 (1944).

[82] D. R. Allan, A. A. Kelsey, S. J. Clark, R. J. Angel and G. J. Ackland, "High-pressure semiconductor-semimetal transition in TiS_2", Phys. Rev. B **57**, 5106–5110 (1998).

[83] R. Andrae, T. Schulze-Hartung and P. Melchior, "Dos and don'ts of reduced chi-squared", arXiv preprint arXiv:1012.3754 (2010).

[84] M. B. Walker and R. L. Withers, "Stacking of charge-density waves in $1T$ transition-metal dichalcogenides", Phys. Rev. B **28**, 2766–2774 (1983).

[85] K. Nakanishi and H. Shiba, "Theory of three-dimensional orderings of charge-density waves in $1T$-TaX_2 (X: S, Se)", Journal of the Physical Society of Japan **53**, 1103–1113 (1984).

[86] S. Tanda, T. Sambongi, T. Tani and S. Tanaka, "X-ray study of charge density wave structure in $1T$-TaS_2", Journal of the Physical Society of Japan **53**, 476–479 (1984).

[87] D. E. Moncton, F. J. DiSalvo, J. D. Axe, L. J. Sham and B. R. Patton, “Charge-density wave stacking order in $1T$-$Ta_{1-x}Zr_xSe_2$: interlayer interactions and impurity (Zr) effects”, Phys. Rev. B **14**, 3432–3437 (1976).

[88] W. Kohn and L. J. Sham, “Self-consistent equations including exchange and correlation effects”, Phys. Rev. **140**, A1133–A1138 (1965).

[89] W. Koch, M. C. Holthausen and M. C. Holthausen, *A chemist’s guide to density functional theory*, Vol. 2 (Wiley-Vch Weinheim, 2001).

[90] P. Hohenberg and W. Kohn, “Inhomogeneous electron gas”, Phys. Rev. **136**, B864–B871 (1964).

[91] D. M. Ceperley and B. J. Alder, “Ground state of the electron gas by a stochastic method”, Phys. Rev. Lett. **45**, 566–569 (1980).

[92] J. P. Perdew, K. Burke and M. Ernzerhof, “Generalized gradient approximation made simple”, Phys. Rev. Lett. **77**, 3865–3868 (1996).

[93] K. Koepernik and H. Eschrig, “Full-potential nonorthogonal local-orbital minimum-basis band-structure scheme”, Phys. Rev. B **59**, 1743–1757 (1999).

[94] A. Ernst, “Full-potential-verfahren mit einer kombinierten basis für die elektronische struktur”, PhD thesis (Technische Universität Dresden, 1997).

[95] A. Einstein, “Über einen die Erzeugung und Verwandlung des Lichtes betreffenden heuristischen Gesichtspunkt”, Annalen der Physik **322**, 132–148 (1905).

[96] A. Damascelli, Z. Hussain and Z.-X. Shen, “Angle-resolved photoemission studies of the cuprate superconductors”, Rev. Mod. Phys. **75**, 473–541 (2003).

[97] A. Damascelli, “Probing the electronic structure of complex systems by arpes”, Physica Scripta **2004**, 61 (2004).

[98] G. Borstel, “Theoretical aspects of photoemission”, English, Applied Physics A **38**, 193–204 (1985).

[99] S. Hüfner, *Photoelectron spectroscopy: principles and applications* (Springer Science & Business Media, 2003).

[100] C. Caroli, D. Lederer-Rozenblatt, B. Roulet and D. Saint-James, “Inelastic effects in photoemission: microscopic formulation and qualitative discussion”, Phys. Rev. B **8**, 4552–4569 (1973).

[101] J. D. Koralek, J. F. Douglas, N. C. Plumb, Z. Sun, A. V. Fedorov, M. M. Murnane, H. C. Kapteyn, S. T. Cundiff, Y. Aiura, K. Oka, H. Eisaki and D. S. Dessau, “Laser based angle-resolved photoemission, the sudden approximation, and quasiparticle-like spectral peaks in $Bi_2Sr_2CaCu_2O_{8+\delta}$”, Phys. Rev. Lett. **96**, 017005 (2006).

[102] M. Lindroos, S. Sahrakorpi and A. Bansil, “Matrix element effects in angle-resolved photoemission from $Bi_2Sr_2CaCu_2O_8$: energy and polarization dependencies, final state spectrum, spectral signatures of specific transitions, and related issues”, Phys. Rev. B **65**, 054514 (2002).

[103] G. Margaritondo, *Introduction to synchrotron radiation.* (Oxford University Press, 1988).

[104] K. Rossnagel, E. Rotenberg, H. Koh, N. V. Smith and L. Kipp, “Continuous tuning of electronic correlations by alkali adsorption on layered $1T$-TaS_2”, Phys. Rev. Lett. **95**, 126403 (2005).

[105] J. Voit, L. Perfetti, F. Zwick, H. Berger, G. Margaritondo, G. Grüner, H. Höchst and M. Grioni, “Electronic structure of solids with competing periodic potentials”, Science **290**, 501–503 (2000).

[106] W. Ku, T. Berlijn and C.-C. Lee, “Unfolding first-principles band structures”, Phys. Rev. Lett. **104**, 216401 (2010).

[107] M. Bovet, S. van Smaalen, H. Berger, R. Gaal, L. Forró, L. Schlapbach and P. Aebi, “Interplane coupling in the quasi-two-dimensional $1T$-TaS_2”, Phys. Rev. B **67**, 125105 (2003).

[108] M. Bovet, D. Popovic, F. Clerc, C. Koitzsch, U. Probst, E. Bucher, H. Berger, D. Naumovic and P. Aebi, “Pseudogapped fermi surfaces of $1T$-TaS_2 and $1T$-$TaSe_2$: a charge density wave effect”, Phys. Rev. B. **69**, 125117 (2004).

[109] P. Darancet, A. J. Millis and C. A. Marianetti, “Three-dimensional metallic and two-dimensional insulating behavior in octahedral tantalum dichalcogenides”, Phys. Rev. B **90**, 045134 (2014).

[110] T. Pillo, J. Hayoz, H. Berger, M. Grioni, L. Schlapbach and P. Aebi, “Remnant fermi surface in the presence of an underlying instability in layered $1T$-TaS_2”, Phys. Rev. Lett. **83**, 3494–3497 (1999).

[111] R. Brouwer, “Incommensurability in crystal structures”, PhD thesis (Rijksuniversiteit Groningen (Netherlands), 1978).

[112] N. V. Smith, S. D. Kevan and F. J. DiSalvo, “Band structures of the layer compounds $1T$-TaS_2 and $2H$-$TaSe_2$ in the presence of commensurate charge-density waves”, J. Phys. C. **18**, 3175–3189 (1985).

[113] K. Rossnagel and N. V. Smith, “Spin-orbit coupling in the band structure of reconstructed $1T$-TaS_2”, Phys. Rev. B **73**, 073106 (2006).

[114] J. C. Slater and G. F. Koster, “Simplified LCAO method for the periodic potential problem”, Phys. Rev. **94**, 1498–1524 (1954).

[115] W. A. Harrison, *Elementary electronic structure* (World Scientific Singapore, 2004).

[116] S. v. d. Walt, S. C. Colbert and G. Varoquaux, “The numpy array: a structure for efficient numerical computation”, Computing in Science & Engineering **13**, 22–30 (2011).

[117] K. Rossnagel and N. V. Smith, “Spin-orbit splitting, fermi surface topology, and charge-density-wave gapping in $2H$-TaSe$_2$”, Phys. Rev. B. **76**, 073102 (2007).

[118] E. Abate and M. Asdente, “Tight-binding calculation of $3d$ bands of Fe with and without spin-orbit coupling”, Phys. Rev. **140**, A1303–A1308 (1965).

[119] L. F. Mattheiss, “Band structures of transition-metal-dichalcogenide layer compounds”, Phys. Rev. B **8**, 3719–3740 (1973).

[120] A. Koitzsch, I. Opahle, S. Elgazzar, S. V. Borisenko, J. Geck, V. B. Zabolotnyy, D. Inosov, H. Shiozawa, M. Richter, M. Knupfer, J. Fink, B. Büchner, E. D. Bauer, J. L. Sarrao and R. Follath, “Electronic structure of CeCoIn$_5$ from angle-resolved photoemission spectroscopy”, Phys. Rev. B **79**, 075104 (2009).

[121] S. V. Borisenko, A. A. Kordyuk, A. N. Yaresko, V. B. Zabolotnyy, D. S. Inosov, R. Schuster, B. Büchner, R. Weber, R. Follath, L. Patthey and H. Berger, “Pseudogap and charge density waves in two dimensions”, Phys. Rev. Lett. **100**, 196402, 196402 (2008).

[122] G. Wiegers, J. de Boer, A. Meetsma and S. van Smaalen, “Domain structure and refinement of the triclinic superstructure of $1T$-TaSe$_2$ by single crystal x-ray diffraction”, Zeitschrift für Kristallographie/International journal for structural, physical, and chemical aspects of crystalline materials **216**, 45–50 (2001).

Danksagung

Im Folgenden möchte ich einige Worte des Dankes an jene richten, welche auf die eine oder andere Weise zum Gelingen dieser Arbeit beigetragen haben.

An erster Stelle gilt mein Dank Prof. Bernd Büchner für die hervorragende Möglichkeit meine Dissertation am IFW Dresden anzufertigen. In besonderem Maße möchte ich zudem Jochen Geck für die ausgezeichnete Betreuung danken. Seine Begeisterung für die Physik, zusammen mit seiner Fähigkeit komplexe Zusammenhänge verständlich zu erklären, wirkte stets hoch motivierend auf mich. Außerdem empfand ich es als sehr angenehm, dass seine Tür – im wahrsten Sinne des Wortes – immer für uns offen stand, was sicherlich keine Selbstverständlichkeit ist.

Furthermore, I want to thank Gaston Garbarino for introducing me into the world of high-pressure X-ray diffraction experiments and the countless hours he spend with us at the beamline during night shifts. I also want to express my gratitude to Alexei Bosak, Michael Hanfland and Michael Krisch for their support during beamtimes at the ESRF. Ebenso möchte ich mich bei Kai Roßnagel für wertvolle Diskussionen bedanken.

Bei Klaus Koepernick möchte ich mich für seinen exzellenten DFT Code sowie hilfreiche Anregungen bedanken. Für die technische Unterstützung am IFW bedanke ich mich bei Stefan Leger und Roland Hübel. Weiterhin danke ich Marion Malkoc, Kerstin Höllerer, Manja Maluk und Katja Schmiedel für die unverzichtbare Unterstützung bei der Bewältigung administrativer Herausforderungen.

Darüber hinaus möchte ich meiner gesamten Arbeitsgruppe für den kreativen und wertvollen fachlichen Austausch danken. Ganz herzlich bedanke ich mich insbesondere bei Jan Trinckauf. Die Diskussionen mit ihm haben ganz entscheidend zum Gelingen dieser Arbeit beigetragen. Frederik Klein danke ich stellvertretend für all meine Bürokollegen am IFW welche zu der höchst angenehmen Arbeitsatmosphäre beigetragen haben.

Auf privater Seite möchte ich meinen Eltern dafür danken, dass sie stets ein offenes Ohr für mich haben. Wenn auch an letzter Stelle geht mein größter Dank an Anne für den Rückhalt, den sie mir gibt und das Verständnis, das sie mir entgegen bringt.

Erklärung

Hiermit versichere ich, dass ich die vorliegende Dissertation ohne unzulässige Hilfe Dritter und ohne Benutzung anderer als der angegebenen Hilfsmittel angefertigt habe. Die aus fremden Quellen direkt oder indirekt übernommenen Gedanken sind als solche kenntlich gemacht. Die Arbeit wurde bisher weder im Inland noch im Ausland in gleicher oder ähnlicher Form einer anderen Prüfungsbehörde vorgelegt.

Die vorliegende Dissertation wurde am Leibniz Institut für Festkörper- und Werkstofforschung Dresden unter der wissenschaftlichen Betreuung von Dr. Jochen Geck und Prof. Bernd Büchner angefertigt.

Bis zum jetzigen Zeitpunkt habe ich keinerlei erfolglose Promotionsverfahren absolviert.

Ich erkenne hiermit die Promotionsordnung der Fakultät Mathematik und Naturwissenschaften der Technischen Universität Dresden an.

Tobias Ritschel
Dresden, Mai 2015